MINISTÉRIO DA CIÊNCIA E TECNOLOGIA
INSTITUTO NACIONAL DE PESQUISAS ESPACIAIS

sid.inpe.br/mtc m21d/2024/05.09.00.30-TDI

COMPUTATIONAL STATISTICS AND MACHINE LEARNING APPROACHES FOR MONITORING AND PREDICTING IONOSPHERIC SCINTILLATION

André Ricardo Fazanaro Martinon

Doctorate Thesis of the Graduate Course in Applied Computing, guided by Drs. Stephan Stephany, and Eurico Rodrigues de Paula, approved in April 10, 2024.

URL of the original document:
<http://urlib.net/8JMKD3MGP3W34T/4B9G5HL>

INPE
São José dos Campos
2024

PUBLISHED BY:

Instituto Nacional de Pesquisas Espaciais - INPE
Coordenação de Ensino, Pesquisa e Extensão (COEPE)
Divisão de Biblioteca (DIBIB)
CEP 12.227-010
São José dos Campos - SP - Brasil
Tel.:(012) 3208-6923/7348
E-mail: pubtc@inpe.br

MINISTÉRIO DA CIÊNCIA E TECNOLOGIA
INSTITUTO NACIONAL DE PESQUISAS ESPACIAIS

sid.inpe.br/mtc m21d/2024/05.09.00.30-TDI

COMPUTATIONAL STATISTICS AND MACHINE LEARNING APPROACHES FOR MONITORING AND PREDICTING IONOSPHERIC SCINTILLATION

André Ricardo Fazanaro Martinon

Doctorate Thesis of the Graduate Course in Applied Computing, guided by Drs. Stephan Stephany, and Eurico Rodrigues de Paula, approved in April 10, 2024.

URL of the original document:
<http://urlib.net/8JMKD3MGP3W34T/4B9G5HL>

INPE
São José dos Campos
2024

Cataloging in Publication Data

Martinon, André Ricardo Fazanaro.

M366c Computational statistics and machine learning approaches for monitoring and predicting ionospheric scintillation / André Ricardo Fazanaro Martinon. – São José dos Campos : INPE, 2024.

xxii + 144 p. ; (sid.inpe.br/mtc m21d/2024/05.09.00.30-TDI)

Thesis (Doctorate in Applied Computing) – Instituto Nacional de Pesquisas Espaciais, São José dos Campos, 2024.

Guiding : Drs. Stephan Stephany, and Eurico Rodrigues de Paula.

1. Ionospheric scintillation. 2. Map of amplitude scintillation. 3. Map of phase scintillation. 4. ROTI map. 5. Scintillation prediction. I.Título.

CDU 681.3.019:519.6

MINISTÉRIO DA CIÊNCIA, TECNOLOGIA E INOVAÇÃO

INSTITUTO NACIONAL DE PESQUISAS ESPACIAIS

DEFESA FINAL DE TESE DE ANDRÉ RICARDO FAZANARO MARTINON
BANCA Nº 062/2024, REGISTRO 39306/2020

No dia 10 de abril de 2024, às 14:00 horas, por videoconferência, o(a) aluno(a) mencionado(a) acima defendeu seu trabalho final (apresentação oral seguida de arguição) perante uma Banca Examinadora, cujos membros estão listados abaixo. O(A) aluno(a) foi APROVADO(A) pela Banca Examinadora, por unanimidade, em cumprimento ao requisito exigido para obtenção do Título de Doutor em Computação Aplicada, com a exigência de que o trabalho final a ser publicado deverá incorporar as correções sugeridas pela Banca Examinadora, com revisão pelo(s) orientador(es).

Novo Título: "COMPUTATIONAL STATISTICS AND MACHINE LEARNING APPROACHES FOR MONITORING AND PREDICTING IONOSPHERIC SCINTILLATION".

Membros da Banca:

Dr. Reinaldo Roberto Rosa – Presidente – INPE
Dr. Stephan Stephany – Orientador (a) – INPE
Dr. Eurico Rodrigues de Paula – Orientador (a) – INPE
Dr. Jonas Rodrigues de Souza – Membro Interno – INPE
Dr. Alison de Oliveira Moraes – Membro Externo – IAE
Dr. João Franciso Galera Monico – Membro Externo – FCT-UNESP

Documento assinado eletronicamente por **Eurico Rodrigues de Paula**, **Pesquisador**, em 17/04/2024, às 08:14 (horário oficial de Brasília), com fundamento no § 3º do art. 4º do Decreto nº 10.543, de 13 de novembro de 2020.

Documento assinado eletronicamente por **Reinaldo Roberto Rosa**, **Pesquisador Titular**, em 17/04/2024, às 09:17 (horário oficial de Brasília), com fundamento no § 3º do art. 4º do Decreto nº 10.543, de 13 de novembro de 2020.

Documento assinado eletronicamente por **Jonas Rodrigues de Souza**, **Pesquisador**, em 17/04/2024, às 09:26 (horário oficial de Brasília), com fundamento no § 3º do art. 4º do Decreto nº 10.543, de 13 de novembro de 2020.

Documento assinado eletronicamente por **Stephan Stephany**, **Pesquisador Titular**, em 17/04/2024, às 09:47 (horário oficial de Brasília), com fundamento no § 3º do art. 4º do Decreto nº 10.543, de 13 de novembro de 2020.

Documento assinado eletronicamente por **JOAO FRANCISCO GALERA MONICO (E)**, **Usuário Externo**, em 17/04/2024, às 15:57 (horário oficial de Brasília), com fundamento no § 3º do art. 4º do Decreto nº 10.543, de 13 de novembro de 2020.

Documento assinado eletronicamente por **Alison de oliveira moraes (E)**, **Usuário Externo**, em 17/04/2024, às 17:46 (horário oficial de Brasília), com fundamento no § 3º do art. 4º do Decreto nº 10.543, de 13 de novembro de 2020.

A autenticidade deste documento pode ser conferida no site https://sei.mcti.gov.br/verifica.html, informando o código verificador **11888062** e o código CRC **9B009D14**.

Referência: Processo nº 01340.002882/2024-35 SEI nº 11888062

A meus pais ***Sergio*** *(in memoriam) e* ***Sandra****, ao meu irmão* ***Alexandre*** *e à minha esposa* ***Ceila***

ACKNOWLEDGEMENTS

I would like to express my gratitude to the National Institute for Space Research (INPE) and to its Applied Computing postgraduate course. Also, I am grateful to my advisors Dr. Stephan Stephany and Dr. Eurico Rodrigues de Paula for their guidance, the weekly discussions and collaboration.

I am grateful to the Brazilian multi-institutional project INCT "GNSS Technology for Supporting Aerial Navigation" and the National Laboratory for Scientific Computing (MCTIC/LNCC, Brazil) for the use of the Santos Dumont supercomputer, as part of the project "Implementation of machine learning approaches that demand supercomputing for ionospheric scintillation prediction and meteorological forecast of severe convective events".

I am thankful to Dr. Bruno César Vani and Dr. Luiz Felipe Campos de Rezende for discussing their methodologies for generating scintillation maps. And, also thankful to MsC. Ítalo Tsuchiya for the configuration of all the GNSS-NavAer INCT network Septentrio receivers, in order to transmit incoming scintillation data blocks.

I would like to acknowledge the LISN (Low-latitude Ionospheric Sensor Network), the RBMC (Rede Brasileira de Monitoramento Contínuo dos Sistemas GNSS - IBGE) and the GNSS-NavAer INCT for the data employed in this work.

The current work was accomplished with the support of National Council for Scientific and Technological Development (CNPq, Brazil) doctorate grant 140562/2020-6 and the Coordination for the Improvement of Higher Education Personnel (CAPES, Brazil) – Finance Code 001.

ABSTRACT

Monitoring and prediction of ionospheric scintillation is a current topic of research since scintillation affects important services like Global Navigation Satellite Systems (GNSS). Scintillation monitoring relies on data provided by networks of GNSS stations, but according to the country, the number and distribution of these stations is uneven. Consequently, bidimensional maps of the amplitude scintillation index S4 are employed covering the region or country of interest. Alternatively, other indexes/variables related to scintillation could be employed instead of S4, like the phase amplitude index sigma-phi (σ_ϕ) or even the rate of change of Total Electron Content (TEC) index (ROTI), as proposed here. Another possibility is to derive probability maps from the chosen ionospheric variable in order to estimate the probability of occurrence of scintillation taking into account elevation and azimuthal angles given by the satellite-station line of sight. This work compares maps of different ionospheric indexes, showing that they are equivalent for the monitoring of scintillation. Another issue is how to generate smooth maps with accuracy and absence of artifacts, which requires preprocessing and interpolation steps. A recently proposed methodology for generating such maps in real-time using a PC-server is shown here. It employs specific preprocessing options and interpolation by Gaussian Process Regression, allowing to generate better maps, which are more correlated to actual GNSS station data and presenting less errors. The choice of the most suitable index for the generation of the maps is discussed, as well the derived probability maps. Furthermore, prediction of the occurrence of scintillation is presented from the time series of a specific parameter derived from amplitude scintillation maps or using the corresponding probability maps. Computational performance, map accuracy and prediction performance are included in the discussion.

Keywords: Ionospheric scintillation. Map of amplitude scintillation. Map of phase scintillation. ROTI map. Scintillation prediction.

ABORDAGENS DE ESTATÍSTICA COMPUTACIONAL E APRENDIZADO DE MÁQUINA PARA MONITORAMENTO E PREDIÇÃO DA CINTILAÇÃO IONOSFÉRICA

RESUMO

O monitoramento e a predição da cintilação ionosférica é um tema atual de pesquisa, uma vez que a cintilação afeta serviços importantes como os sistemas globais de navegação por satélite (Global Navigation Satellite Systems - GNSS). O monitoramento da cintilação depende de dados fornecidos por redes de estações GNSS, mas conforme o país, o número e a distribuição dessas estações é irregular. Consequentemente, mapas bidimensionais do índice S4 de cintilação em amplitude podem ser empregados para cobrir a região ou país de interesse. Alternativamente, outras variáveis relacionadas à cintilação poderiam ser empregadas em vez do índice S4, como o índice sigma-phi (σ_ϕ) da cintilação em fase ou mesmo o índice ROTI relativo à taxa de variação do conteúdo eletrônico total (Total Electron Content - TEC), como aqui proposto. Outra possibilidade é a derivação de mapas de probabilidade do índice escolhido para se estimar a probabilidade de ocorrência de cintilação levando em conta os ângulos de elevação e de azimute definidos pela linha de visada satélite-estação. Este trabalho compara mapas de diferentes índices ionosféricos mostrando que são equivalentes para o monitoramento da cintilação. Outro aspecto é como gerar mapas que sejam suaves, precisos e que não apresentem artefatos indesejáveis, o que requer definição de métodos de pré-processamento e interpolação. Uma metodologia recentemente proposta para gerar esses mapas em tempo real usando um PC servidor é apresentada aqui. Emprega opções específicas de pré-processamento e interpolação por regressão por Processo Gaussiano, permitindo gerar mapas melhores, mais correlacionados com dados reais de estações GNSS e apresentando menos erros. Além disso, a predição de ocorrência de cintilação é feita utilizando séries temporais de um parâmetro específico derivado dos mapas de cintilação em amplitude ou usando os correspondentes mapas de probabilidade. Desempenho computacional, acurácia dos mapas e desempenho de predição são também discutidos.

Palavras-chave: Cintilação ionosférica. Mapa de cintilação em amplitude. Mapa de cintilação em fase. Mapa de ROTI. Predição de cintilação.

LIST OF FIGURES

Page

LIST OF TABLES

Page

LIST OF ABBREVIATIONS

AGW	–	Atmospheric Gravity Waves
API	–	Application Programming Interface
ASCII	–	American Standard Code for Information Interchange
BEIDOU	–	Chinese Global Navigation Satellite System
CALIBRA	–	Countering GNSS high Accuracy applications Limitations due to ionospheric disturbances in Brazil
CIGALA	–	Concept for Ionospheric Scintillation Mitigation for Professional GNSS in Latin America
CORR	–	Pearson's Correlation Coefficient
CSV	–	Comma-separated values file format
DBMS	–	Database Management System
DDEF	–	Disturbance Dynamo Electric Field
DLR	–	Deutsches Zentrum für Luft- und Raumfahrt
Dst	–	Disturbance Storm Time Index
EIA	–	Equatorial Ionization Anomaly
ENRI	–	Electronic Navigation Research Institute
ESA	–	European Space Agency
EUV	–	Extreme Ultraviolet
FTP	–	File Transfer Protocol
GALILEO	–	European Global Navigation Satellite System
GBAS	–	Ground Based Augmentation System
GLONASS	–	Russian Global Navigation Satellite System
GNSS	–	Global Navigation Satellite System
GPR	–	Gaussian Process Regression
GPS	–	Global Positioning System
GPU	–	Graphics Processing Unit
HTTP	–	Hypertext Transfer Protocol
IBGE	–	Instituto Brasileiro de Geografia e Estatística
ICAO	–	International Civil Aviation Organization
ICEA	–	Ministry of Aeronautics Institute for Airspace Control
IDW	–	Inverse Distance Weighting
IGRF	–	International Geomagnetic Reference Field
IGS	–	International GNSS Service
IMPC	–	Ionosphere Monitoring and Prediction Center
INCT	–	Institutos Nacionais de Ciência, Tecnologia e Inovação
INGV	–	Italian National Institute of Geophysics and Volcanology
INPE	–	National Institute for Space Research
IP	–	Internet Protocol
IPP	–	Ionospheric Pierce Point
ISMR	–	Ionospheric Scintillation Monitoring Receiver
JSON	–	JavaScript Object Notation
L-SAR	–	L-band Synthetic Aperture Radar
LISN	–	Low-Latitude Ionospheric Sensor Network

LT	–	Local time
MAE	–	Mean Absolute Error
MMAX	–	Mean of Maximum Errors
MMIN	–	Mean of Minimum Errors
MXAE	–	Mean of Maximum Absolute Errors
N/A	–	Not applicable
NaN	–	Not a number
NavAer	–	GNSS Technology for Supporting Aerial Navigation
NoSQL	–	Not only SQL
NTRIP	–	Networked Transport of RTCM via Internet Protocol
OpenMP	–	Open Multi-Processing
PC	–	Personal Computer
PNG	–	Portable Network Graphic
PPEF	–	Prompt Penetration of eastward Electric Field
PRN	–	Pseudorandom noise
PSD	–	Power Spectral Density
RBMC	–	Rede Brasileira de Monitoramento Contínuo dos Sistemas GNSS
RF	–	Radio Frequency
RINEX	–	Receiver Independent Exchange Format
RMSE	–	Root Mean Square Error
ROT	–	Temporal rate of change of TEC
ROTI	–	Rate of change of TEC index
SAR	–	Synthetic Aperture Radar
SBAS	–	Satellite Based Augmentation System
SCINDA	–	SCIntillation Network Decision Aid
SCINTEC	–	System for monitoring and mapping of ionospheric scintillation and Total Electron Content in real time over Brazilian territory
SF	–	Ionospheric Spread of F layer
SQL	–	Structured Query Language
SRB	–	Solar Radio Burst
SSS	–	Stratified Shuffle Split
STDA	–	Standard Deviation of Absolute Error
STEC	–	Slant TEC
TCP	–	Transmission Control Protocol
TEC	–	Total Electron Content
TECU	–	TEC units
UK	–	United Kingdom
UNESP	–	São Paulo State University
USB	–	Universal Serial Bus
UT	–	Universal Time
UTC	–	Coordinated Universal Time
VQI	–	Vertical index values reduced by the average value above the 3rd quartile at the centroid
XGBoost	–	eXtreme Gradient Boosting

CONTENTS

Page

1 INTRODUCTION

The use of Global Navigation Satellite Systems (GNSS) for aerial navigation has been a global trend for more than a decade, being currently employed in all phases of flights in most of the countries. GNSS navigation does not usually require ground equipment, and allows to optimize aerial routes, thus reducing required flight time and fuel consumption. However, GNSS signals may be submitted to the strong influence of the ionosphere, which cause positioning errors that affect requirements of the International Civil Aviation Organization (ICAO), such as accuracy, integrity, availability and continuity.

Ionospheric scintillation in amplitude and phase is the major cause of such errors, being associated with ionospheric plasma irregularities. The ionosphere can be modeled by the density of electrons integrated in an unitary cross section of a cylinder that spans from the receiver to the satellite, which is the Total Electron Content (TEC). Regions of depleted plasma (low TEC values) are called ionospheric bubbles, which are formed after sunset near the magnetic equator and expand along the magnetic north and south directions. Small-scale ionospheric plasma irregularities generated inside equatorial plasma bubbles cause amplitude and phase scintillation in the GNSS L band signal, typically in the months of September to March, in Brazil.

Ionospheric scintillation can present a different dynamic according to the geographic location (mainly latitude), hour of the day, month of the year, year of the solar cycle, which typically lasts 11 years, and also geomagnetic activity. It also presents a high daily variability. Over Brazil, performance of GNSSs is much more affected due to ionospheric scintillation than countries of other longitudinal sectors, mainly under the Equatorial Ionization Anomaly (EIA). This issue may affect GNSS-based aerial navigation, being critical for approach and departure procedures. It may also affect some other non-aeronautical applications.

Scintillation affects the receiver signal by a fast phase variation that may cause a loss in the phase lock (LEICK, 1995; SKONE et al., 2001) and/or a rapid amplitude fluctuation, which weakens the signal enough not to be sensed by the loop discriminator (HUMPHREYS et al., 2004; KINTNER et al., 2005). Consequently, there is a decrease in the number of available satellites and a degradation in the GNSS receiver performance (BANDYOPADHAYAY et al., 1997; KINTNER et al., 2001). As a result the required accuracy for aerial navigation and mainly takeoff/landing operations cannot be reached. In Brazil, GNSS augmentation systems like the Satel-

lite Based Augmentation System (SBAS) (DE PAULA et al., 2007) and the Ground Based Augmentation System (GBAS) are affected by ionospheric scintillation, precluding takeoff/landing operations guided by GNSS.

Therefore, the use of GNSS in Brazil is the object of current studies about the effects of ionospheric scintillation. Typically, the monitoring of scintillation is made using maps of the amplitude scintillation index S4, stressing the need for generation of real-time accurate scintillation maps. In particular, the multi-institutional project INCT NavAer (MONICO et al., 2022) was proposed (referred to as INCT for simplicity), allowing for the implementation of a network of GNSS monitoring stations with GNSS receivers able to measure with high acquisition rate (50 to 100 Hz) the raw RF signal of the satellite-receiver link. The derived variables such as TEC, and the amplitude and phase scintillation indexes, respectively S4 and σ_ϕ can then be calculated.

Data provided by the INCT GNSS receivers and other monitoring networks (PAULA et al., 2023) such as the RBMC (Rede Brasileira de Monitoramento Contínuo dos Sistemas GNSS), owned by IBGE (Instituto Brasileiro de Geografia e Estatística), may be employed for technological and research purposes. For instance, to optimize the performance of GNSS receivers during occurrences of ionospheric scintillation, to be assimilated in ionospheric models, and also to provide to potential users real-time scintillation maps. Besides being employed for Aviation, such maps are also useful in geodetic applications, such as precision agriculture and oil prospecting and extraction platforms at deep ocean, vessel navigation, large trucks transporting minerals, just to cite some examples of systems that use GNSS signals. Telecommunication systems using trans-ionospheric signals are also affected. The scintillations also cause distortions (fringes) in images of L-band Synthetic Aperture Radar (SAR) images (SATO et al., 2021).

The monitoring of ionospheric scintillation is thus important, since it may affect critical GNSS-based services. In this scope, the objective of this thesis is to select an ionospheric index most suitable for scintillation monitoring, in order to generate the corresponding maps covering the Brazilian territory and part of the neighboring countries. The map of a particular index or then its derived probability may be chosen (MARTINON et al., 2022), among the amplitude scintillation index (S4), the phase scintillation index (σ_ϕ), or the ROTI (Rate of change of TEC Index). The latter correlates well with the S4 index (CARRANO et al., 2019), and with the σ_ϕ index. In addition, the prediction of occurrence of scintillation is performed using

time series of a parameter derived from amplitude scintillation maps or using the corresponding probability maps, thus allowing the issue of warnings of eventual scintillation occurrences. Among different parameters that were evaluated, the chosen parameter was the percentage area of the considered map with moderate to strong amplitude scintillation values.

1.1 State-of-the-art of the generation and prediction of scintillation-related maps

The making of scintillation maps requires the interpolation of a given ionospheric variable for a finite set of sampling points. Each sampling point corresponds to a Ionospheric Pierce Point (IPP), defined as the intersection of the line-of-sight between the GNSS receiver-satellite (the slant path) with the ionosphere, which is assumed as an uniformly distributed density spherical shell over the Earth at the mean altitude where the maximum value of the ionospheric electron density is observed. Such mean altitude is typically considered as 350 km. In the case of the amplitude scintillation map, the interpolation is made from the S4 values for all IPPs of the considered set of GNSS stations of the given area and for the considered time interval.

Two approaches for generating regional amplitude scintillation maps for the Brazilian region were proposed by Rezende et al. (2007) and Vani (2018). These approaches are based on the IDW (Inverse Distance Weighting) interpolation, but employed different preprocessing options. Recent works proposed the generation of scintillation maps for different parts of the globe, mainly using approaches based on kriging interpolation (AMABAYO et al., 2021; HAMEL et al., 2014; KIEFT et al., 2014). All the cited approaches result in a temporal sequence of maps using or not a priori IPP samples from a previous map of the sequence. A more recent work (KOULOURI, 2022) proposed the use of Kalman filtering for generating scintillation maps in real-time with a 1-minute resolution. Finally, there is the research related to this thesis, described ahead (MARTINON et al., 2023).

Besides scintillation amplitude maps, there are few works about phase scintillation maps and ROTI maps for high/medium latitudes (BEECK; JENSEN, 2021; BÉNIGUEL et al., 2017; CHERNIAK et al., 2018; DE FRANCESCHI et al., 2019; MORTON et al., 2020; NGUYEN et al., 2022; PI et al., 2013; ZHAO et al., 2022). For instance, Cherniak et al. (2018) describes the generation of the ROTI maps over the Northern hemisphere to characterize occurrences of ionospheric irregularities. These maps are provided by the International GNSS Service (IGS) since 2014. In

addition, there is a work (CHERNIAK et al., 2022) describing the extension of the IGS ROTI maps to cover the Southern hemisphere and low/equatorial latitude region. It was intended to evaluate the sensitivity of the ROTI maps to detect plasma irregularities associated with the development of equatorial plasma bubbles for low, middle, and high solar activity periods. These IGS ROTI maps allowed to recognize plasma irregularities related to ionospheric plasma bubbles during local postsunset hours. In particular, the employed sampling rate of 30 s with integration time of 5 minutes and spatial resolution of $2^\circ \times 2^\circ$, allows to identify large irregularities in the TEC field. However, such sampling rate, integration time and spatial resolution are not suitable for scintillation monitoring, as in the case of this thesis.

In addition to the above IGS site, another one that provides ROTI maps in near real-time is the German Deutsches Zentrum für Luft- und Raumfahrt (DLR) IMPC[1] (Ionosphere Monitoring and Prediction Center), but with low resolution, and with no interpolation. Another site provided by Electronic Navigation Research Institute[2] (ENRI), but benefits from the availability of a very dense GNSS monitoring network (SAITO et al., 2021).

Concerning phase scintillation maps, as far as we know, there is only one work about phase scintillation maps, Kieft et al. (2014), using kriging interpolation.

The achievement of accurate scintillation forecast by a numerical model or prediction by a data-oriented models is a current topic of research, and would be much useful in applications of GNSS-based on services (STAFFORD, 2000), which have presented an expanding demand in areas like aviation and agriculture as already mentioned. Since high gradients of TEC may be associated with the occurrence of scintillation (MUELLA et al., 2010), TEC field modeling is also a topic of interest. However, there is not a suitable numerical electron-density model based on first principles able to model the generation and evolution of the ionospheric bubbles, since there are many uncertainties involved in such modeling. There is a numerical model, able to simulate ionospheric bubbles (YOKOYAMA, 2017), but lacking suitable temporal and spatial resolutions to model plasma irregularities. In addition, some numerical models were proposed to predict scintillation, but presented low accuracy (BÉNIGUEL; HAMEL, 2011; RETTERER, 2010; WERNIK et al., 2007).

Research intended for low latitude amplitude scintillation prediction using data-oriented models was started in Brazil (REZENDE, 2009; REZENDE et al., 2010;

[1] <https://impc.dlr.de/products/ionospheric-perturbations/rate-of-change-of-tec-index/>
[2] <https://www.enri.go.jp/cnspub/susaito/rocket/>

LIMA et al., 2014; LIMA et al., 2015). Rezende (2009) and Rezende et al. (2010) proposed some approaches for predicting amplitude scintillation, as well as Vani (2018), but no approach was robust enough to be further developed for operational purposes. Lima et al. (2014) analyzed the correlation between scintillation at São José dos Campos and at São Luís, near the Equator, while Lima et al. (2015) proposed prediction of scintillation at São Luís using only local scintillation data.

Another work, (MCGRANAGHAN et al., 2018) was about prediction at high latitudes, near the North Pole using the persistence model, assuming that scintillation intensity would last a few hours. Besides these works, there seems to be a sole 2021 article concerning low latitude amplitude scintillation prediction (ZHAO et al., 2021), which proposed a data-oriented model using the Gradient Boosting algorithm. It employs S4 data for the 2012-2020 years and also the height of the virtual layer ionospheric F, which is measured by an ionosonde. The approach allows for predictions of occurrence or not of scintillation for the chosen GNSS station for the whole night, according to a threshold of S4 = 0.5. However, there is a single result for every night at the given station that does not take into account any variability along the night, and a sole detection by the algorithm of a S4 value above the threshold for a given line of sight satellite-station would prevail over the remaining others below the S4 threshold. In addition, the prediction performance using the F1 score metric was always below 85 %.

A more recent work also proposed scintillation prediction with data-oriented models for low magnetic latitudes, specifically for São José dos Campos, Brazil, using historical data of ionospheric scintillation and other ionospheric parameters, geomagnetic and solar-activity data for the period 2011-2018 that covers the previous solar cycle (DOS SANTOS, 2022; DOS SANTOS et al., 2022). The proposed prediction algorithms include two Gradient Boosting Tree algorithms, and a convolutional neural network, all available in the Python programming. Prediction performance was promising.

1.2 Objectives

Below, the objectives and contributions of this thesis are listed. The objectives are:

- To provide a better tool for scintillation monitoring over the Brazil territory and neighboring countries by means of suitable real-time scintillation maps. Maps of amplitude and phase scintillation, and also of the ROTI are generated and compared using a recently proposed approach (MAR-

TINON et al., 2023). This comparison is performed in order to check the corresponding errors of these maps for a set of locations given by GNSS stations, and thus analyze which one of these three types of maps is better for scintillation monitoring.

- To analyze the corresponding probability maps (MARTINON et al., 2022) for these three types of maps (amplitude and phase scintillation and ROTI), which take into account azimuthal and elevation angles of each GNSS satellite-station link. An error analysis is also performed to evaluate the probability maps. A future enhancement would be to weight the contribution of each link to the probability using angular differences given by the line of sight elevation angle to the dip magnetic inclination and by the line of sight azimuthal angle to the magnetic declination.

- To employ these maps for the prediction of scintillation occurrences. It is intended to perform the prediction of the occurrence of ionospheric scintillation using the best type of map selected in the main objective. However, in the current work, only time series of amplitude scintillation maps and of the corresponding probability maps are generated for the prediction of the scintillation. In these maps, the fraction of area corresponding to moderate-strong scintillation is taken as a predictive parameter for scintillation prediction using a machine learning algorithm.

The contributions of the thesis follows:

- The recently proposed approach (MARTINON et al., 2023) for the generation of maps of amplitude and phase scintillation and ROTI, which proposes the use of Gaussian Process interpolation and a set of specific preprocessing options for scintillation data.

- The new probability maps (MARTINON et al., 2022) for these three types of maps. Since these maps are generated using azimuthal and elevation angles of each GNSS satellite-station link, a better awareness of scintillation occurrence can be provided to the GNSS user.

- An initial scintillation prediction approach, which employs time series of a parameter derived from amplitude scintillation maps or of the corresponding probability maps. As already mentioned, the parameter is given by the fraction of area corresponding to moderate-strong scintillation is taken as

a predictive parameter for scintillation prediction using a machine learning algorithm. It was tested only for the amplitude scintillation maps and the corresponding probability maps in predictions with an antecedence of 15 minutes of the same night using a machine learning method.

- The implemented prototype (MARTINON et al., 2024) for amplitude and phase scintillation maps with real-time capability. It includes the capability of GNSS-station data being automatically collected by a PC-based real-time server that provides map generation and online dissemination to users through a web server. It allows GNSS users being more aware of current occurrences of scintillation that may affect the accuracy or availability of GNSS-provided location or of a set of locations corresponding to an intended displacement, by means of the map color scale.

- A new algorithm developed for detection and correction of cycle slips, which are discontinuities in the receiver carrier phase lock caused by receiver-satellite loss of the lock, and/or by scintillation affecting their RF link. This algorithm, related to the slant TEC (STEC) measurements, proved to be more efficient than the standard ones.

In future work related to scintillation prediction, time series of different parameters of maps of different ionospheric indexes, or of the corresponding probability maps, may be chosen instead of the time series of the parameter derived from amplitude scintillation maps, shown here, as well as different machine learning approaches. Similarly to the prediction approach presented here, prediction may be tried for a smaller region, antecedence of more hours of the same night, and using additional data such as solar and geomagnetic indexes (exogenous variables).

Furthermore, different machine learning algorithms can be tested, including the related hyperparameter optimization, in order to choose the one with better prediction performance. Tests using higher prediction antecedence can then be tried for the same night.

Finally, also as a future work, a validation will be performed with actual data in order to evaluate the available real-time maps, as well as the accuracy of the predictions of the occurrence of scintillation, concerning scintillation awareness and usefulness to provide warnings of scintillation occurrence in real-time or for the next hours.

1.3 Structure of this thesis

The structure of this thesis is divided as follows. Chapter 2 addresses ionospheric scintillation definitions and climatology, networks of GNSS monitoring stations and measurements of related variables. Chapter 3 is about raw data provided by GNSS monitoring stations and preprocessing options. Chapter 4 shows the approach used to generate maps for amplitude and phase scintillation, and for ROTI, followed by an analysis of the correlation between these three types of maps. Chapter 5 presents the corresponding probability maps for the maps of these three indexes also with a correlation analysis. Chapter 6 presents an approach for the prediction of scintillation based on a time series of a parameter derived from amplitude scintillation maps or using the corresponding probability maps. Chapter 7 presents a prototype of the proposed real-time system for generating and disseminating amplitude and phase scintillation maps, which was already implemented. Finally, Chapter 8 draws conclusions and future work.

2 IONOSPHERIC SCINTILLATION

During daylight the equatorial ionospheric plasma is lifted up due to eastward electric fields. After sunset and until about 21 LT (local time) this upward plasma movement is intensified giving origin to a large vertical electron density gradient at the ionospheric F region base, that is one condition for plasma irregularity to be generated through the Rayleigh Taylor mechanism (ABDU, 2019). If the conditions are favorable these irregularities grow up and while moving upwards at the equatorial region they give origin to large structures known as ionospheric bubbles that map along the magnetic field lines reaching low latitudes. The bubbles can reach the Equatorial Ionization Anomaly (EIA) crests that are regions of high electron density around 15 degrees north and south of the magnetic dip equator. Inside the bubbles smaller scale irregularities are generated by cascading processes and those having the scale size of the first Fresnel zone (about 400 m) cause amplitude and phase scintillation in the L band frequencies like the GNSS signal. As stated in the former section, the ionospheric scintillation can cause loss of lock of the GNSS signal and/or a rapid amplitude fluctuation causing a degradation in the GNSS receiver performance.

2.1 Climatology of ionospheric scintillation

Due to the daily variability of atmospheric neutral winds, the presence of Atmospheric Gravity Waves (AGW) and the variability of the ionospheric electric field responsible for the prereversal peak in the vertical plasma drift around 18 to 21 LT, the plasma irregularities and consequently the ionospheric scintillation also presents a large day-to-day variability. The scintillation has a dependence with the 11 year solar cycle activity, the season, the local time, the geographic position (latitude and longitude) and the geomagnetically disturbed time. Besides these scintillation variations stronger scintillation is observed when the GNSS signal is aligned (elevation and azimuth) with the equatorial plasma bubbles.

2.1.1 Scintillation dependence from solar cycle, season and local time

Figure 2.1 shows the S4 percentage of occurrence (see horizontal bar in the top of the Figure) from the low-latitude GNSS receiver at Cachoeira Paulista from 1998 to 2014 in function of Local Time for links with S4 $>$ 0.2. The F10.7 cm solar flux is represented by the white continuous curve with its values presented at the right vertical axis. It can be observed that scintillation at this site lasts from around September to March/April and from about 20 LT to 25 LT during high solar activity

and practically vanishes during solar minimum activity.

Figure 2.1 - S4 percentage of occurrence at Cachoeira Paulista from 1998 to 2014.

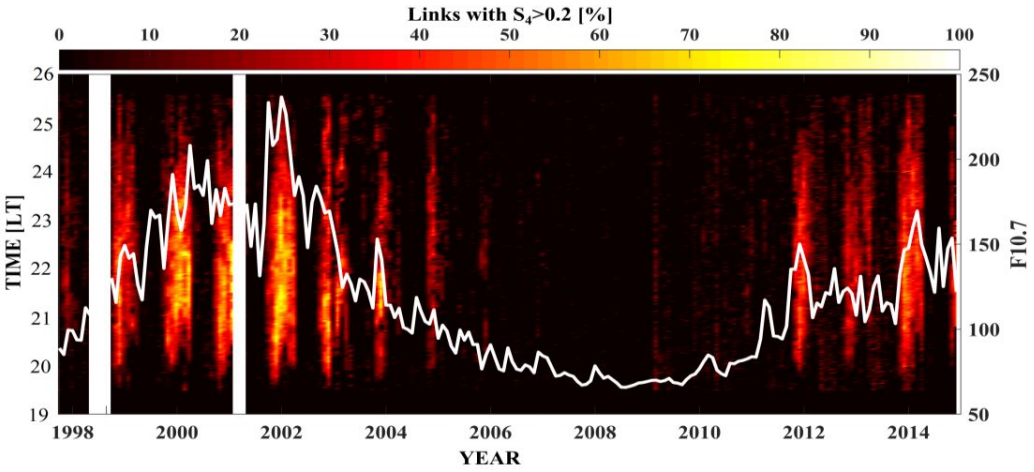

SOURCE: Paula et al. (2021).

2.1.2 Scintillation variation with the latitude and longitude

The latitudinal variation of the scintillation amplitude at low latitudes is substantially influenced by the EIA (Equatorial Ionization Anomaly). Under the ionization EIA crests, that occur between about 15° magnetic degrees north and south of the dip equator, the amplitude scintillation increases due to the larger background electronic density at these regions during the preversal hours (18-21 LT) compared to lower latitudes. The ionospheric irregularities are proportional to the ionization variation ΔN, where N is the background ionization. As N increases close to EIA crests ΔN also should increase since the ratio $\Delta N/N$ remains constant along the magnetic field lines which have a high latitudinal electrical conductivity (PAULA et al., 2003). Figure 2.2 shows the Cumulative Distribution Function of signal amplitude for São Luís close to the magnetic dip equator, Cuiabá between the magnetic dip equator and the EIA crest and São José dos Campos under the EIA crest, for December 6, 2001. Larger signal amplitude ranges are observed under the EIA crest with consequent larger S4 values.

Figure 2.3 presents the S4 values along the satellite tracks projected over the ground between 21 to 03 UT (18 to 24 LT) for March 17, 2002, for the Brazilian region. S4

Figure 2.2 - Cumulative distribution function for the signal amplitude.

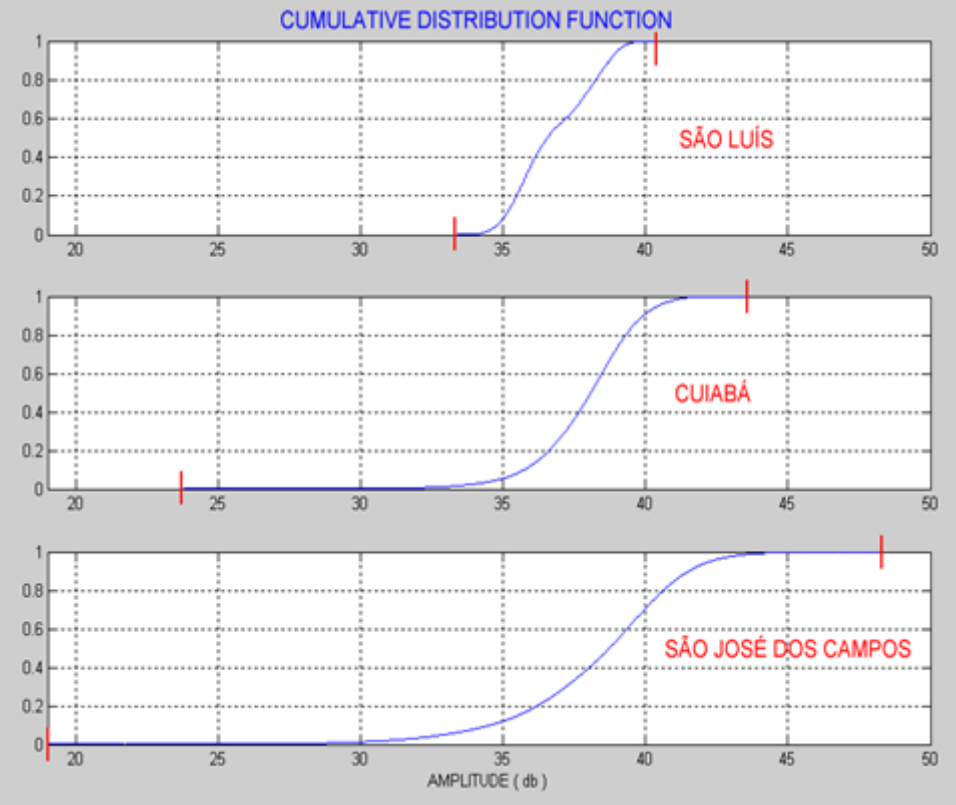

SOURCE: Rezende et al. (2007).

values are represented in the right colored vertical bar. Larger S4 amplitudes are observed under the EIA crest.

Over South America, where the magnetic declination decreases from east to west, the longitudinal effects of the plasma irregularities was studied by Abdu et al. (1998) using the SF (generic term to express ionospheric spread of F layer that occurs during the presence of plasma irregularities) measured by the Digisondes of Cachoeira Paulista (45° W, 22.5° S, −28° dip, magnetic declination 21° W) and Tucumán (64° W, 27° S, −26° dip, magnetic declination 3° W). Much less occurrence of ionospheric irregularities was observed at Tucumán where the magnetic declination is only 3° W. Recent work of (VALLADARES, 2023) showed that the ionospheric scintillation occurrence and intensity over the Brazilian sector are much larger compared to the Peruvian sector. The alignment between the magnetic field lines and the terminator line (day-night) and also the vertical plasma drift at the magnetic

Figure 2.3 - S4 values along the satellite tracks projected over the ground.

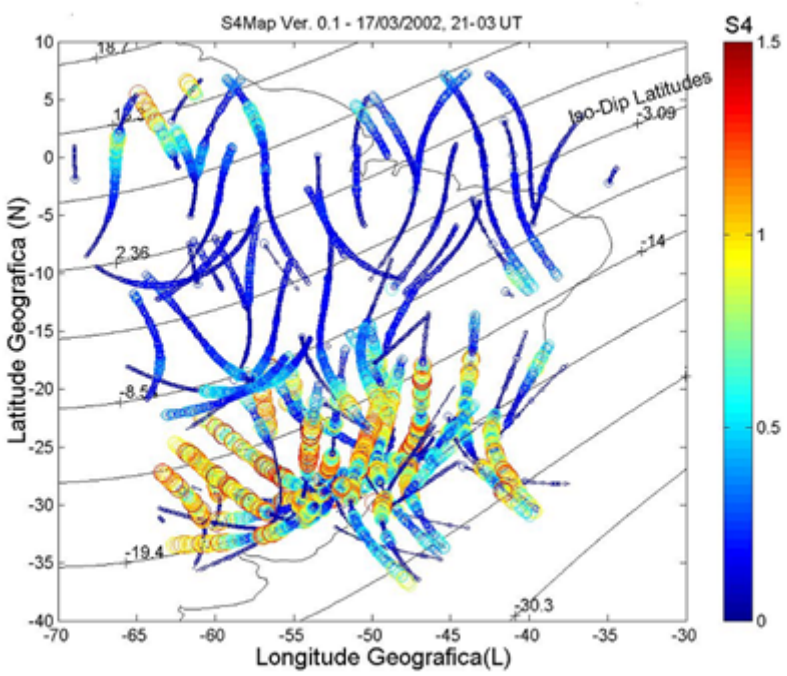

SOURCE: Modified from Rodrigues (2003).

equator are important factors that determine the seasonality and the occurrence of the irregularities at a specific site.

2.1.3 Magnetic storm effects over scintillation

During magnetic storms scintillation can be inhibited or generated even at months when they are not usually expected. The magnetic storms have substantial effects over the scintillation. If there is prompt penetration of eastward electric field (PPEF) from magnetosphere into equatorial region during the prereversal hours, the upward plasma drift is intensified (PAULA et al., 2019) and plasma irregularities can be generated even during no scintillation season. Figure 2.4 presents one example of scintillation triggering during the 10-12 April 2001 strong magnetic storm. No strong scintillation was expected for this month since scintillation decays after March over Brazilian sector, but scintillation was observed only during the night 11/12 at all satellites during the storm main and part of the recovery phase, when the magnetic index Dst reached about $-260\,\mathrm{nT}$. In the upper panel the Dst index is plotted in red line. However, if the prompt penetration of the electric field is westward, scintillation

may be inhibited.

Figure 2.4 - S4 index triggered during the night 11/12 April, 2001 during the occurrence of a strong magnetic storm.

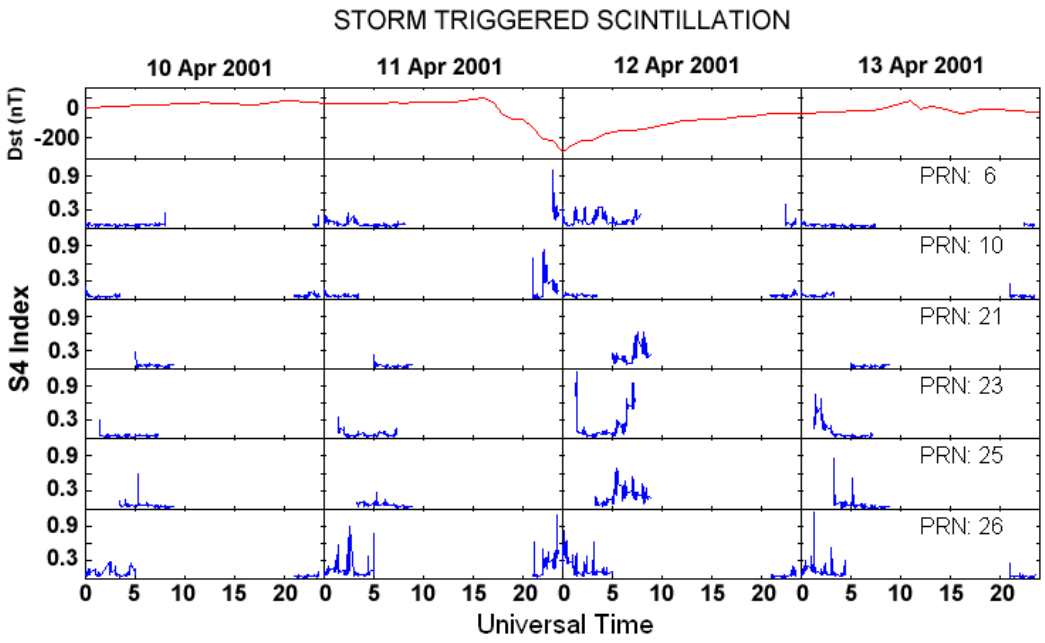

SOURCE: Paula et al. (2022).

During the storm main phase, the high latitude region becomes heated by the auroral intensified currents (Joule effect) and energetic particle precipitations generating a storm time neutral wind blowing initially to the equator direction that generates the disturbance dynamo electric field (DDEF) (ABDU et al., 2006). This electric field is westward during daytime and pre reversal hours and inhibits the prereversion plasma drift peak and consequently the generation of plasma irregularities. It takes some hours after the storm main phase for this process to set up one westward electric field at the magnetic equator. Figure 2.5 shows one example of scintillation inhibition at 8 GNSS satellites during the super strong storm night 20/21 November 2003. In the upper panel it is plotted the Dst index (red line) that reached almost $-500\,\mathrm{nT}$, which is considered a severe storm.

During the occurrence of large solar flares, Solar Radio Burst (SRB) causes large

Figure 2.5 - Example of scintillation inhibition during the night of 20/21 November 2003 few hours after the storm main phase.

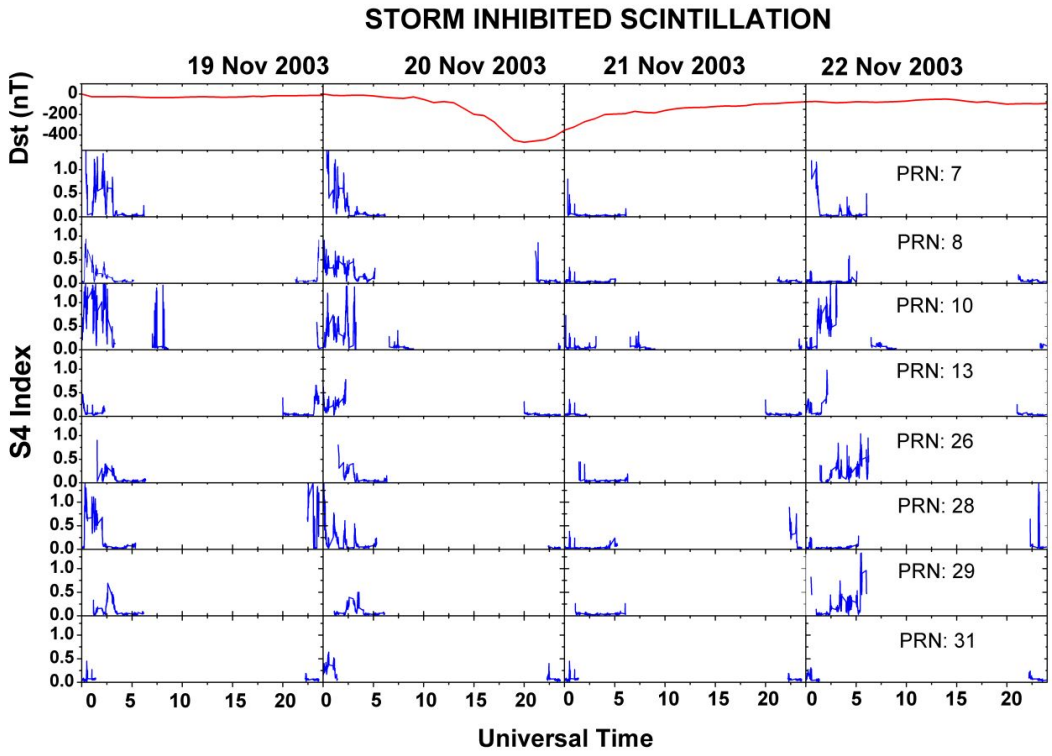

SOURCE: Paula et al. (2022).

noise in the GNSS signal in the sunlit side and gives rise to amplitude fluctuations that can interrupt the GNSS services for a short period of time. During these SRBs increased EUV radiation causes large ionization at the D and E ionospheric regions that can block the Digisonde signal during many minutes. Figure 2.6 shows the C/No ratio for 06 September 2017 during the X9.3 solar flare for the frequencies L1 C/A, L2C and L5 for Fortaleza, Inconfidentes and São José dos Campos (PAULA et al., 2022), where fadings can be observed at the frequencies L2C and L5 during the SRB peak at 12:02 UT on day September 06, 2017. The vertical red line is the time of the solar flare maximum. The figure shows that the L1 frequency C/No was not affected, but C/No for the L2C and L5 frequencies were attenuated during such event.

Figure 2.6 - GPS C/No signal for L1, L2C and L5 GPS frequencies during 06 September 2017 for the sites FRTZ, INCO and SJCU.

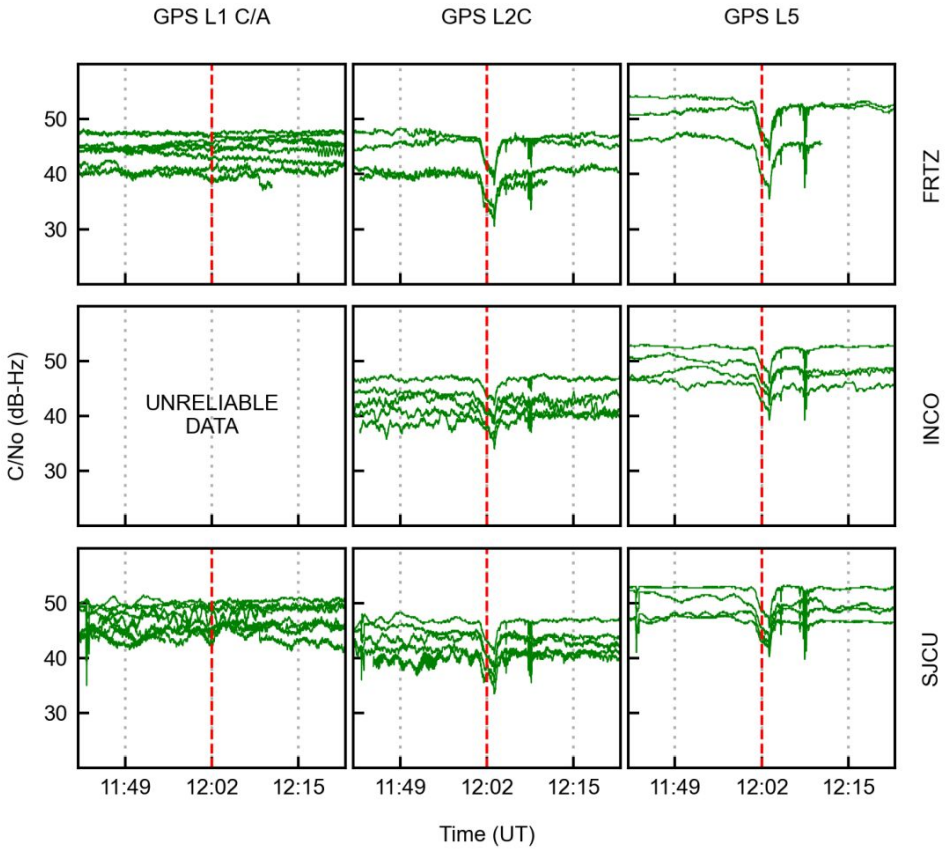

SOURCE: Paula et al. (2022).

2.1.4 Receiver-satellite link and the equatorial plasma bubble alignment

When there is the alignment (azimuth and elevation) between the GNSS signal and the equatorial plasma bubble that extends in the direction NW (21° W) over Brazil, this signal propagates a longer distance in the turbulent medium created by the bubbles. In these events more severe scintillation is triggered compared to other directions (MORAES et al., 2018) with consequent loss of phase lock and larger phase scintillations. Figure 2.7 (a) presents the amplitude scintillation events plotted at the respective IPP projections for the periods of 15-30 November 2014 and 04-18 February 2015 for São José dos Campos (23.2° S, 45.9° W, dip latitude: 19.2° S). The outer and inner circles define elevations equal to 20° and 60°, respectively. The IPPs were considered at 350 km of altitude and only signals from satellite elevations larger

than 20° were considered in this study. Figure 2.7 (b) and (c) show the azimuth and elevation of the scintillation cases, respectively. According to this figure the most severe scintillations are from satellite tracks aligned with NW magnetic direction, with azimuth around 315° and the signals from these satellites are prone to have larger losses of lock (PAULA et al., 2022).

Figure 2.7 - The amplitude scintillation events plotted at the respective IPP projections for GPS-L1 signals for the periods of 15-30 November 2014 and 04-18 February 2015 for São José dos Campos (a) and their azimuthal (b) and elevation (c) angles spatial distribution.

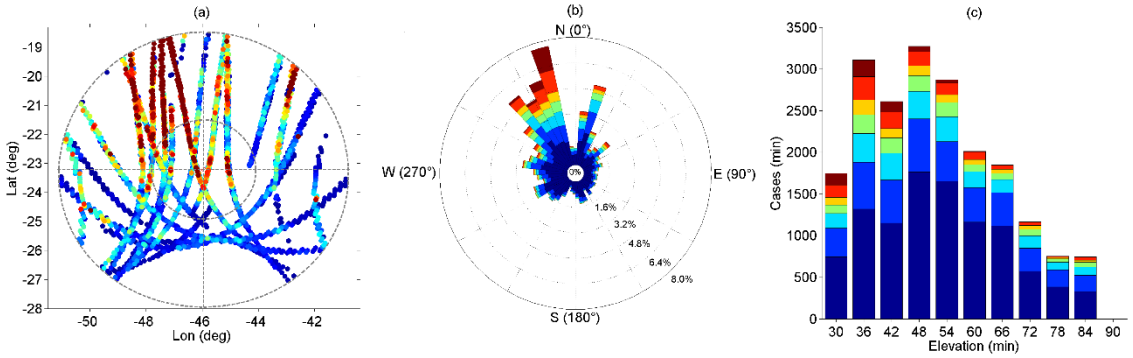

SOURCE: Paula et al. (2022).

2.2 GNSS monitoring networks

The pioneering ionospheric scintillation monitoring network in the Brazilian territory was implemented by the SCINTEC project, and it was operational between 1997 and 2017. In this network, scintillation data was acquired by CASCADE GPS receivers (GEC-Plessey GPS card) developed jointly with Cornell University and the National Institute for Space Research (INPE).

There are currently three ionospheric monitoring networks in operation in Brazil. The first one is the Low-Latitude Ionospheric Sensor Network (LISN) (VALLADARES; CHAU, 2012) that includes scintillation monitors (Novatel GSV 4004B-G2 receivers), magnetometers and ionosondes. This network covers not only the Brazilian territory, but some other regions of South America. The second one is the CIGALA/CALIBRA network, derived from a joint project between UK Nottingham University, the Italian National Institute of Geophysics and Volcanology (INGV),

the Slovenian University of Nova Gorica, the Belgian company Septentrio and the Brazilian São Paulo State University (UNESP) and ConsultGEL consultancy on geomatics. This network was funded by ESA (European Space Agency), aiming to monitor and characterize the effects of scintillation on GNSS positioning (VANI et al., 2017). It employs Septentrio PolaRxS PRO and Septentrio PolaRx5S scintillation monitor receivers, and it has been expanded in the scope of the Brazilian INCT project "GNSS technology to support Air Navigation". The third one is the ICEA (Ministry of Aeronautics Institute for Airspace Control) network, which uses mainly Septentrio PolaRxS PRO scintillation monitor receivers, but access to updated data is restricted. A current map showing all the active monitoring stations of these three networks, is shown in <https://ismrquerytool.fct.unesp.br/is/>.

The Brazilian Network for Continuous Monitoring of the GNSS Systems (RBMC) maintained by the Instituto Brasileiro de Geografia e Estatística (IBGE) consists in a set of geodetic stations, equipped with high-performance GNSS (Global Navigation Satellite Systems) receivers, which provide observations to assess coordinates once a day or in real time. This network has provided 15-second resolution data in the RINEX 2 format since 2010 and in the RINEX 3 format since 2017. More recently, after January 1st, 2020, provides 1-Hz resolution data in the RINEX 3 format.

Differently from the other three networks previously presented, the IBGE RMBC network is not aimed at monitoring ionospheric scintillation, which requires a more specialized GNSS receiver with sampling frequency of 50 Hz. However, this network has a much higher number of receivers (currently, 147) providing a better and more dense coverage of the Brazilian territory, as can be seen in Figure 2.8. Data can be download from the RBMC's HTTP repository[1].

A recent work by (PAULA et al., 2023) provides more detailed information about the Brazilian GNSS networks for ionospheric monitoring.

Data files are available for 15-minute or 1-day periods. Real time data download is available using the NTRIP caster of the RBMC server. Such data allows to calculate the STEC and the ROTI, which is the standard deviation of the temporal rate of change of TEC (ROT) for a given time interval, using different combinations of sampling frequency and time interval for ROTI calculation. The ROTI has a good correlation with S4 and σ_ϕ indexes and it can be used to detect scintillation in regions with scarcity of scintillation monitors.

[1] <https://geoftp.ibge.gov.br/informacoes_sobre_posicionamento_geodesico/rbmc/>

Figure 2.8 - IBGE RBMC stations available on January 10, 2024.

SOURCE: Instituto Brasileiro de Geografia e Estatística (2024)

2.3 Ionospheric scintillation indexes derived from GNSS receiver data

The receivers of the ground stations of the GNSS monitoring networks provide raw data that allows to calculate scintillation amplitude and phase indexes in a straightforward manner. These stations also allow estimating ROT and its corresponding standard deviation, the ROTI for the given sampling frequency and time interval. Numerical experimentation was performed concerning these parameters, allowing to conclude that the best combination is sampling frequency of 1 second and time interval of 1 minute for ROTI calculation. Maps of ROTI are potential alternative to

maps of amplitude or phase scintillation for monitoring scintillation, since ROTI is highly correlated to scintillation. The reason is that scintillation normally occurs in areas that present high TEC gradients and/or high TEC temporal rates. However, ROT and ROTI calculations demand a relatively high processing cost.

2.3.1 Amplitude Scintillation index

Amplitude scintillation is given by the S4 index, estimated from radio frequency signals acquired at 50 Hz by receivers of GNSS monitoring stations. Typically, the signal intensity of 3,000 samples of 1-minute interval is used to calculate the S4 index value given by the intensity standard deviation normalized by the mean intensity (VAN DIERENDONCK et al., 1993).

$$\mathrm{S4} = \sqrt{\frac{\langle I^2 \rangle - \langle I \rangle^2}{\langle I \rangle^2}} \tag{2.1}$$

with:

$$I = A^2 = I_c^2 + Q_c^2 \tag{2.2}$$

Where I is the signal intensity, A is the amplitude of the received signal, I_c and Q_c are the signal intensity in-phase and quadrature components, and $\langle\,\rangle$ is ensemble intensity.

The S4 index is calculated for each available GNSS satellite-receiver link from several constellations (GPS, GLONASS, GALILEO, BEIDOU, SBAS, etc.), for a multi-constellation capable receiver. As a consequence, the number of GNSS satellites that are visible for a station can exceed 30 in the same minute. In addition, the S4 index is also calculated for 1 or more L-band frequencies available at the receiver for each satellite. Taking into account the GPS constellation and the L1 C/A signal or the L1C modernized signal, for newer GPS satellites, the calculations of the index S4 are compatible between GNSS stations equipped with different receivers (PAULA et al., 2021).

The present work employs all available GNSS constellations and the corresponding L1 signal for the considered time interval to produce the amplitude scintillation maps, except for SBAS satellites which are only used to assess errors of the maps.

2.3.2 Phase scintillation index

The phase scintillation is given by the σ_ϕ index, as well as the S4 index estimated from radio frequency signals acquired at 50 Hz by receivers of GNSS monitoring stations. Typically, the signal phase fluctuations of 3,000 samples of a 1-minute interval is used to calculate the σ_ϕ index value given by the phase fluctuations standard deviation (VAN DIERENDONCK et al., 1993).

$$\sigma_\phi = \sqrt{\langle \phi^2 \rangle - \langle \phi \rangle^2} \tag{2.3}$$

Where ϕ is the unwrapped and detrended carrier phase. The carrier phase detrend is performed by a sixth-order Butterworth high-pass filter with a default cutoff frequency of 0.1 Hz.

Only the INCT network monitoring stations calculate the σ_ϕ index. These GNSS receivers record the σ_ϕ over 1, 3, 10, 30 and 60 second non overlapping intervals every 60 seconds for each satellite of all available constellations and frequencies. As stated by Moraes et al. (2017) the σ_ϕ over 60 second interval is more adequate to represent the phase scintillation at low-latitudes, corresponding to the Fresnel scale of interest. The present work employs all available GNSS constellations, except SBAS, and the corresponding L1 signal for the considered time interval to produce the phase scintillation maps using the σ_ϕ over 60 second. It is important to note that the SBAS satellites signal phase fluctuations are not suitable to calculate σ_ϕ (VAN DIERENDONCK; ARBESSER-RASTBURG, 2004).

2.3.3 Rate of change of TEC index (ROTI)

The TEC is the electron density (n_e) given by the line integral along the signal slant path s from receiver to satellite, considering a column of one-meter-square cross section centered on the path, which is given in TEC units (TECU), defined as $1\,\text{TECU} = 10^{16}\,\text{electrons/m}^2$.

$$\text{TEC} = \int n_e \, ds \tag{2.4}$$

Typical TEC values measured near the Earth's surface range from about 1 to 150 TECU (JONAH, 2013) with the actual value depending on geographic location, local time, season, solar EUV flux, and magnetic activity.

The relative STEC can be characterized by observing carrier phase delays of the received RF signal transmitted from GNSS satellites. The carrier phase observable recorded by a multi-frequency GNSS receiver allows to estimate the STEC, in TECU, as follows:

$$\text{STEC} = \frac{f_1^2 f_2^2}{f_1^2 - f_2^2} \frac{L_1 - L_2}{K} \tag{2.5}$$

In the above equation, f_1 and f_2 are the two carrier frequencies of the GNSS signals, L_1 and L_2 are the carrier phase counts, and $K \approx 40.3\, m^3 s^{-2}$.

The ROT is defined by the difference between two successive TEC measurements according to a sampling frequency. Typically, measurements are made every 30 seconds, but this rate can be adjusted depending on the region (low, middle or high latitude) and on the plasma drift conditions (PI et al., 1997). ROT is computed in units of TECU/s:

$$\text{ROT}_m = \frac{\text{TEC}_m - \text{TEC}_{m-1}}{t_m - t_{m-1}} \tag{2.6}$$

The ROTI is defined as standard deviation of the ROT over a defined time interval, typically 5 minutes, and also given in TECU/s, as follows:

$$\text{ROTI} = \sqrt{\langle \text{ROT}^2 \rangle - \langle \text{ROT} \rangle^2} \tag{2.7}$$

The combination of STEC/ROT sampling rate and ROTI calculation time interval determines the minimum and maximum size of the ionospheric irregularities that can be detected. Furthermore, STEC/ROT sampling rate must be compatible with the zonal drift velocity in the region of interest (JACOBSEN, 2014). According to Carrano et al. (2019), the best sampling rate for STEC/ROT in low latitude regions is 1 Hz and ROTI calculated with 1 minute time interval, which were the adopted criterion in this work.

2.3.4 Scintillation severity classes

It is very difficult to define scintillation severity classes, since it requires establishing precise thresholds for each class, and there is not a general consensus in this matter. Perhaps the most important threshold is the value above which there is strong scin-

tillation, but also it varies with research institutes of different countries. Therefore, the thresholds adopted here were defined trying to ensure the maximum separability between classes, either for classification purposes in the case of maps for scintillation monitoring, or for scintillation prediction purposes. An additional difficulty is that strong scintillation in phase and/or amplitude may cause GNSS satellite-station loss-of-lock, and consequently scintillation is not measured and such data is lost. This may be a topic of a future research analyzing loss of lock in scintillation sensors like Septentrio receivers of INCT GNSS stations or different receivers of the RBMC GNSS monitoring stations.

In this work, for the amplitude scintillation index, the S4 index, the adopted scintillation severity classes are:

- Weak Scintillation: $0.15 \leq \text{S4} < 0.3$.
- Moderate Scintillation: $0.3 \leq \text{S4} \leq 0.7$.
- Strong Scintillation: $\text{S4} > 0.7$.

Values less than 0.15 are not considered as amplitude scintillation.

For the phase scintillation index, the σ_ϕ index, the adopted scintillation severity classes are:

- Weak Scintillation: $0.15 \leq \sigma_\phi < 0.3$.
- Moderate Scintillation: $0.3 \leq \sigma_\phi \leq 0.7$.
- Strong Scintillation: $\sigma_\phi > 0.7$.

The σ_ϕ is expressed in radians, and values less than 0.15 radians are not considered as phase scintillation.

For the ROTI, the adopted scintillation severity classes are:

- Weak Scintillation: $0.04 \leq \text{ROTI} < 0.09$.
- Moderate Scintillation: $0.09 \leq \text{ROTI} \leq 0.2$.
- Strong Scintillation: $\text{ROTI} > 0.2$.

The ROTI is expressed in TECU/s, and values less than 0.04 TECU/s are not considered as scintillation.

Besides the ranges adopted for the scintillation severity classes, S4 values above 1.4, σ_ϕ above 1.4 radian and ROTI above 0.4 TECU/s are considered outliers.

2.3.5 Vertical projection

Spogli et al. (2009) proposed the use of the scintillation index S4 and σ_ϕ projected to the vertical, to take into account the geometrical effects on the measurements made at different elevation angles. The S4 index value projected to the vertical can be obtained by the following equation:

$$S4_v = S4 \frac{1}{(F(\theta_{el}))^{(p+1)/4}} \tag{2.8}$$

Above S4 is the index directly calculated at a given elevation angle (θ_{el}) along the slant path, i.e. the line of sight satellite-station. In the same equation, the exponent p is the spectral slope of the phase Power Spectral Density (PSD), which is provided by the INCT stations at a 1-minute rate for each satellite, while for the LISN stations it is assumed as $p = 2.6$ (SPOGLI et al., 2013). $F(\theta_{el})$ is a mapping function defined as:

$$F(\theta_{el}) = \frac{1}{\sqrt{1 - \left(\frac{R_E \cos(\theta_{el})}{R_E + H_{ipp}}\right)}} \tag{2.9}$$

Where R_E is the Earth radius (6.371 km), the altitude of the IPP (350 km) and θ_{el} the satellite elevation angle.

The σ_ϕ index value can be projected to the vertical using the following equation:

$$\sigma_\phi^v = \sigma_\phi \frac{1}{(F(\theta_{el}))^a} \tag{2.10}$$

Where σ_ϕ is the index directly calculated at a given elevation angle (θ_{el}) along the slant path (RINO, 1979), which describes the signal phase variance as a function of the zenith angle, and the exponent a of the phase is assumed to be 0.5. And $F(\theta_{el})$

is the mapping function defined in Equation 2.9.

Also, the ROTI value can be projected to the vertical according to Li et al. (2022) using the following equation:

$$\mathrm{ROTI_v} = \mathrm{ROTI}\frac{1}{F(\theta_{\mathrm{el}})} \tag{2.11}$$

Above, ROTI is the index directly calculated at a given elevation angle (θ_{el}) along the slant path and $F(\theta_{\mathrm{el}})$ is the mapping function defined in Equation 2.9.

2.3.6 Ionospheric pierce point

The IPP coordinates are determined by the ground station receiver coordinates and azimuthaland elevation angles of the GNSS satellite as shown in Figure 2.9.

Figure 2.9 - Geometry of a satellite-ground station line-of-sight depicting the Ionospheric Pierce Point.

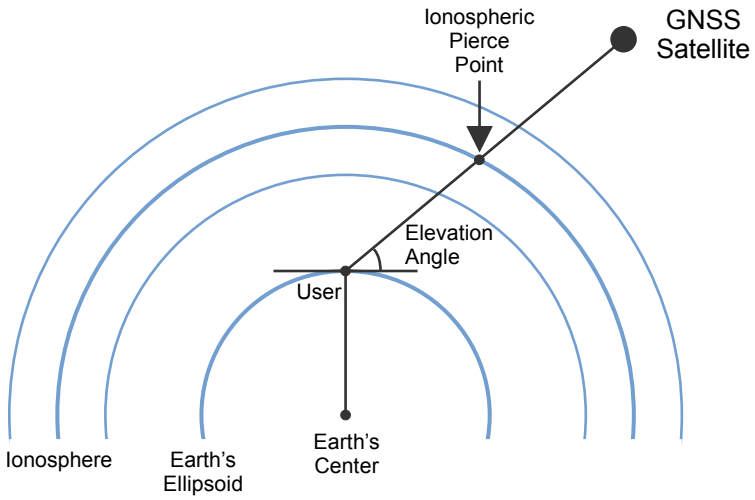

SOURCE: Martinon et al. (2023).

The geographic latitude (ϕ_{ipp}) and longitude (λ_{ipp}) of the IPP are given by the following equations (PROL et al., 2017):

$$\phi_{\text{ipp}} = \sin^{-1}\left[\sin\left(\phi_{\text{r}}\right)\cos\left(\Psi\right) + \cos\left(\phi_{\text{r}}\right)\sin\left(\Psi\right)\cos\left(\theta_{\text{az}}\right)\right] \tag{2.12}$$

$$\lambda_{\text{ipp}} = \lambda_{\text{r}} + \sin^{-1}\left[\frac{\sin\left(\Psi\right)\sin\left(\theta_{\text{az}}\right)}{\sin\left(\phi_{\text{ipp}}\right)}\right] \tag{2.13}$$

with:

$$\Psi = \frac{\pi}{2} - \theta_{\text{el}} - \sin^{-1}\left[\frac{R_{\text{E}}}{\left(R_{\text{E}} + H_{\text{ipp}}\right)}\cos\left(\theta_{\text{el}}\right)\right] \tag{2.14}$$

Above, ϕ_{r} and λ_{r} are respectively the latitude and longitude of the ground station, R_{E} is the Earth radius (6,371 km), H_{ipp} is the IPP altitude (350 km), and θ_{az} and θ_{el} are the azimuthal and elevation angles (in radians) of the GNSS satellite.

Considering a 24-hour time interval, each receiver-satellite link produces a sequence of closely-spaced IPPs, since the satellites are moving along their orbits. As shown in Figure 2.10, the closer to the geographic Equator a ground station is, the more its IPP distribution is similar to a circle for all satellites in lock. It can also be observed that for stations at lower latitudes less than 15° S, there are less lines-of-sight pointing to the South, due to the orbits of the GPS-constellation satellites. Similarly, the opposite occurs in the Northern hemisphere.

Figure 2.10 - 24-hour IPP distribution of 28th of November, 2013 for 23 monitoring stations in Brazil of the LISN and CIGALA/CALIBRA networks.

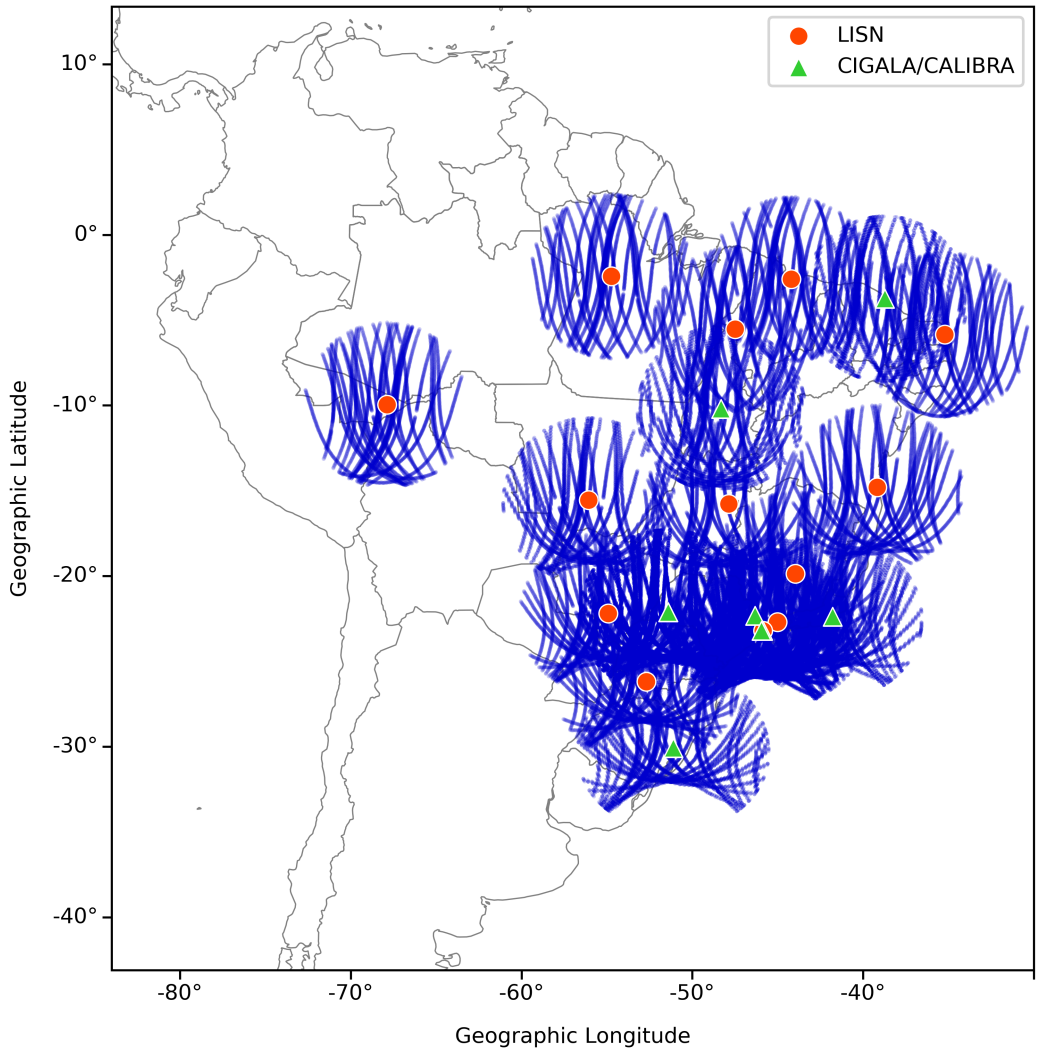

3 GNSS DATA AND POST-ACQUISITION PROCESSING METHODS

GNSS data is acquired by GNSS monitoring stations and undergoes some processing before being typically transmitted to a central server. This post-acquisition processed data varies according to the adopted format, and is further employed to generate scintillation maps.

The GNSS data used in this work was obtained from two ionospheric monitoring networks, the LISN monitoring stations covering most of South America, and the INCT stations, which cover only the Brazilian territory. LISN receivers are only compatible with GPS and SBAS satellites, while INCT receivers are multi-constellation. Data from the RBMC network was also employed, mainly in RINEX 3 format that provides multi-constellation observables.

The LISN data are provided in ASCII files, but according to a specific format, described in APPENDIX A - LISN S4 DATA FORMAT. Daily files comprehending 24 hours of data are available for each LISN station. INCT data are in the CSV (comma-separated values) format, with each line corresponding to a record/sample and each column following the order defined by the manufacturer (Septentrio), as described in APPENDIX B - SEPTENTRIO ISMR DATA FORMAT. Data can be downloaded for intervals of 15 minutes or one hour depending on the configuration of each INCT station. The RBMC RINEX 3 can be downloaded as 24 hours files with the 1/15 Hz sampling rate and 15 minutes files with the 1 Hz sampling rate, for each station.

The LISN network only provides the S4 index, whereas the INCT network provides the S4 and σ_ϕ index. For the ROTI calculation were used data from the INCT and RBMC networks with 1 Hz sampling rate.

3.1 Monitoring stations data

The geographic location of each monitoring station is mandatory: (i) to calculate the ionospheric pierce point of each observation, (ii) and allows estimating satellite orbits using precise ephemerides. Thus, the Cartesian coordinates X, Y and Z were obtained for each station belonging to the LISN, INCT and RBMC networks. The Cartesian coordinates were converted to geodetic coordinates in order to obtain the latitude, the longitude, and the altitude values of each station. Besides the geographic location, the station nomenclature, city, state, and country were also obtained. Finally these parameters were organized in a data set following the file

format presented in Table 3.1, and stored as a CSV file.

Table 3.1 - Monitoring stations data set file format.

Field	**Description**
name	4-letter monitoring station identifier.
city	The city where the station is located.
state	The state where the station is located.
country	The country where the station is located.
x	Cartesian coordinate X, of the station geographic location.
y	Cartesian coordinate Y, of the station geographic location.
z	Cartesian coordinate Z, of the station geographic location.
lat	Geographic latitude.
lon	Geographic longitude.
altitude	Elevation, above sea level, of the station geographic location.
network	LISN, INCT or RBMC.

3.2 S4 data

Since the format of the data provided by the two monitoring networks (LISN and INCT) is different, a unified data format was adopted, as shown in Table 3.2. The "i_lat" and "i_lon" values correspond to the IPP coordinates. The "s4" values are classified according to the scintillation severity using the following thresholds: null [0.00-0.15], weak (0.15-0.30], moderate (0.30-0.70], or strong (0.70-1.4) being available in the "class" column. Values of "s4" above 1.4 were considered outliers, being rounded to that value. In order to filter out data of L-band links affected by ground interference and the related multipath reflections, only satellite elevations higher than 30° were considered. The "s4v" value correspond to the vertical projection of the slant S4 value, as proposed by Spogli et al. (2009) and the spectral slope of the phase PSD (p) was defined according to Rino (1979) for LISN receivers ($p = 2.6$), and Spogli et al. (2013), for INCT receivers (p measured every minute).

3.3 σ_ϕ data

Although only the INCT network provides the σ_ϕ index data, to standardize the datasets, a data format based in the unified data format presented in Section 3.2 was

Table 3.2 - Unified S4 data file format for each S4 observation.

Field	**Description**
datetime	Day and time in format "yyyy-mm-dd hh:mm:ss".
prn	Satellite identifier.
az	Azimuth (degrees).
el	Elevation (degrees).
s4	S4 index from the C/A code in the L1 band.
s4v	Vertical projection of the S4 index.
class	Scintillation severity classification (0: null; 1: weak; 2: moderate; 3: strong).
station	Acronym of the monitoring station.
r_lat	Monitoring station latitude (degrees).
r_lon	Monitoring station longitude (degrees).
i_lat	IPP latitude (degrees).
i_lon	IPP longitude (degrees).
constellation	GPS, SBAS, GLONASS, GALILEO or BEIDOU.
network	LISN or INCT.
p	Spectral slope of the phase PSD in the 0.1 to 25 Hz range.

adopted, as shown in Table 3.3. The "i_lat" and "i_lon" values correspond to the IPP coordinates. The "phi60" values are classified according to the scintillation severity using the following thresholds: null [0.00-0.15], weak (0.15-0.30], moderate (0.30-0.70], or strong (0.70-1.4) being available in the "class" column. Values of "phi60" above 1.4 rad were considered outliers, being rounded to that value. In order to filter out data of L-band links affected by ground interference and the related multipath reflections, only satellite elevations higher than 30° were considered. The "phi60v" value corresponds to the vertical projection of the slant σ_ϕ value, as proposed by Spogli et al. (2013).

3.4 ROTI data

The ROTI data is not readily available by the monitoring networks as the S4 and σ_ϕ data, but demands to be calculated. Such calculation requires the use of an algorithm for detection and correction of cycle slips, which are discontinuities in the receiver carrier phase lock caused by receiver-satellite loss of the lock, and/or by scintillation

Table 3.3 - Unified σ_ϕ data file format for each σ_ϕ observation.

Field	**Description**
datetime	Day and time in format "yyyy-mm-dd hh:mm:ss".
prn	Satellite identifier.
az	Azimuth (degrees).
el	Elevation (degrees).
phi60	σ_ϕ index from the C/A code in the L1 band.
phi60v	Vertical projection of the σ_ϕ index.
class	Scintillation severity classification (0: null; 1: weak; 2: moderate; 3: strong).
station	Acronym of the monitoring station.
r_lat	Monitoring station latitude (degrees).
r_lon	Monitoring station longitude (degrees).
i_lat	IPP latitude (degrees).
i_lon	IPP longitude (degrees).
constellation	GPS, GLONASS, GALILEO or BEIDOU.
network	INCT.

affecting their RF link. A new algorithm, developed in the scope of this thesis, was able to detect more cycle slips than the standard algorithms.

In order to calculate ROTI some initial data processing included reading and converting RINEX files obtained from the INCT and RBMC networks to a simpler data format, as described in APPENDIX C - STEC DATA FILE FORMAT. The converted data is enhanced with the elevation and azimuthal angles of each satellite, which are interpolated using the IGS "Precise Satellites Orbits" data.

This initial conversion includes the STEC calculation applying the Equation 2.5, using the corresponding phase observables for the L1 and L2 frequencies for each constellation. These STEC values then undergo some preprocessing steps for ROT calculation, which is done applying the Equation 2.6.

First, cycle slips and data gaps must be detected and corrected. Cycle slip is a discontinuity in a receiver carrier phase lock on a satellite signal. The cycle slip can be defined as an abrupt change, or difference, in the continuity of the measured

phase cycles. This can be caused by receiver-satellite loss of the lock, and/or by scintillation affecting their RF link.

Standard methods for GNSS cycle slip detection make use of phase data on a combination of two carrier frequencies. The relative STEC is a geometry-free linear combination and was employed in this work in order to detect cycle slips using a new iterative algorithm proposed here. Figure 3.1 shows cycle slips and data gaps on the relative STEC for some hours of a particular day. Figure 3.2 shows the final STEC data after the application of the proposed iterative algorithm for the same period of time. The proposed iterative algorithm consists in applying detection and correction tasks until no further cycle slip can be detected, according to a stop condition.

Figure 3.1 - STEC data for GPS satellite PRN 14 presenting cycle slips and data gaps.

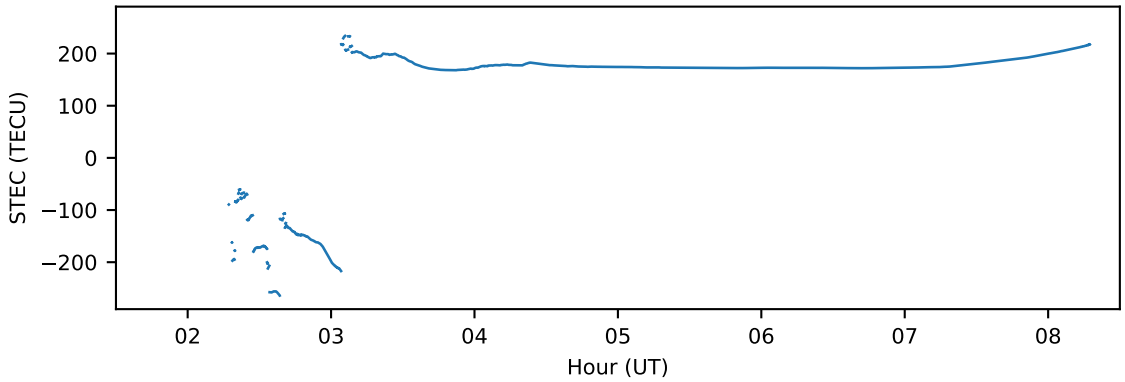

The cycle slip detection starts by checking STEC rate of changes over time. Two consecutive values of STEC are subtracted and the absolute value of the difference is taken - if such value is above a given threshold, this jump indicates a cycle slip. In this case, the threshold is given by the mean of the absolute STEC rate ($\overline{dSTEC}$) plus its standard deviation (std) multiplied by a factor (α). This factor defines the level above which the jumps are considered as cycle slips. It is important to note that low values could omit STEC variation due to scintillation and high values could not detect potential cycle slips. Values ranging from 7 to 14 for α present a good compromise between preserving scintillation variation and cycle slips detection in the relative STEC data. Another influence of the adopted α value is the correlation between ROTI and the S4 or σ_ϕ indexes, as further discussed in Chapter 4.

Figure 3.2 - STEC data for GPS satellite PRN 14 without cycle slips or data gaps.

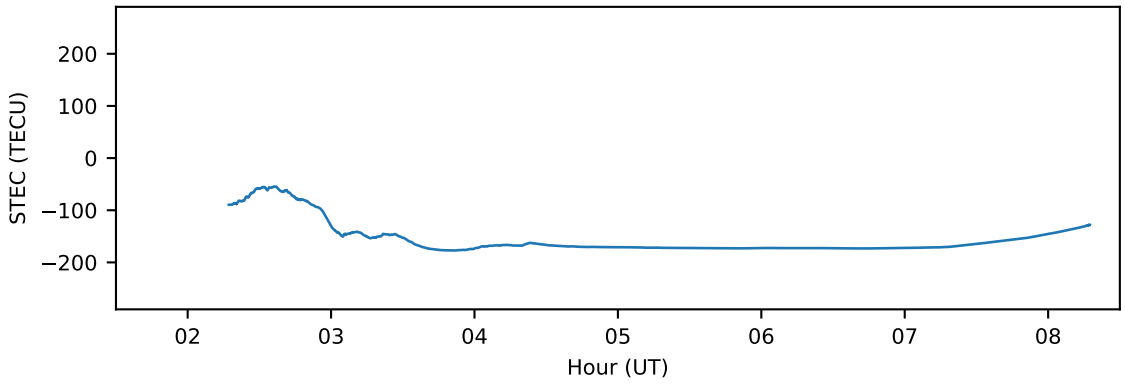

Figure 3.3 - Absolute STEC rate (dSTEC) curve for GPS satellite PRN 14, showing the threshold using $\alpha = 12.5$ for the detection of cycle slips.

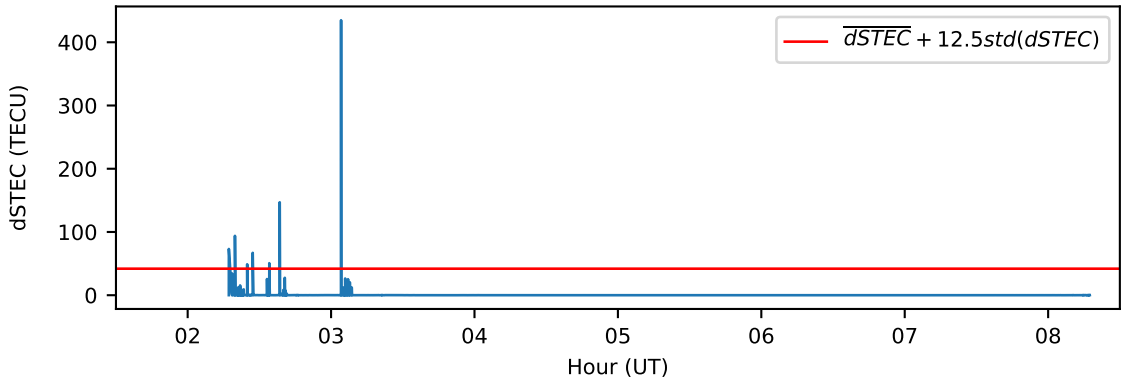

Once the cycle slips are detected (Figure 3.3) using the calculated threshold, the STEC curve can be corrected, starting with the assignment of NaN (not a number) to the points that presented cycle slips. Afterwards, for each of these points (in sequence), subtracting its preceding value from the following part of the curve. This implies having the first value after the cycle slip equal to the last value before the cycle slip. Thus, to avoid two adjacent repeated values, one of them is assigned as NaN. Figure 3.4 shows the corrected STEC data after the removal of the cycle slips detected in Figure 3.3.

Standard methods perform cycle slip detection in a single step, but the algorithm

Figure 3.4 - Corrected STEC after cycle slip removal for GPS satellite PRN 14.

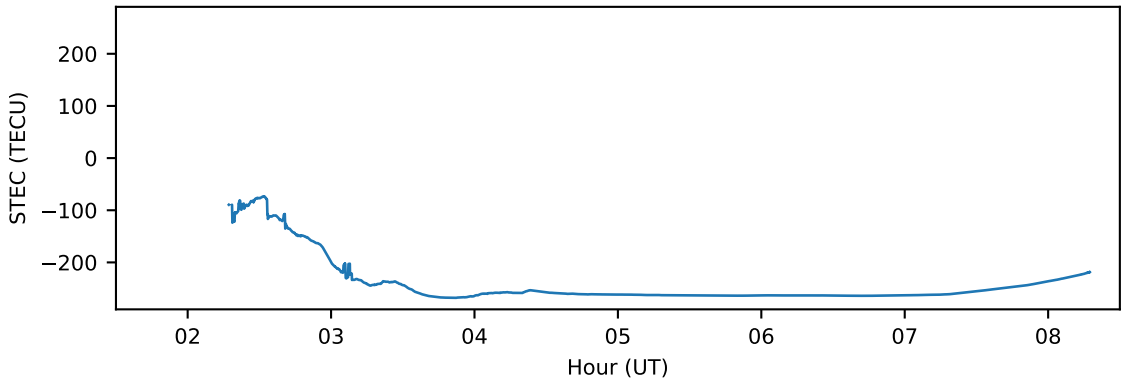

proposed here executes several steps in an adaptive way, employing the mean and standard deviation in each step, and stopping after no further cycle slips are detected. This allows to also remove cycle slips due to strong scintillation, not only the ones due to loss of lock. The following Figure 3.5, shows 4 detection-correction steps that were required by the proposed algorithm, showing no cycle slips in the final STEC values of the last step.

The second preprocessing step is to detrend the STEC time series for each satellite. As stated by Carrano et al. (2019), the definition of the ROTI calculation assumes that the ROT fluctuations is a zero-mean random process, otherwise the STEC must be detrented before computing ROTI. The detrend method applied is based on the method proposed by Paula et al. (2021) and is described below:

I. Each satellite STEC time series is resampled at the same sampling rate (1 Hz) of the RINEX file;

II. A linear interpolation is applied to fill data gaps due to losses of lock;

III. A 60-second moving average is performed to obtain the STEC trend;

IV. This trend is subtracted from the resampled STEC data (step I.).

After applying this method, the STEC time series does not present trends due to the range variation due to the satellite orbit (geometric Doppler), and also the contribution from terrestrial multipath will be partially suppressed, resulting in a zero-mean random process ROT time series.

Figure 3.5 - Sequence of 4 detection-correction steps for cycle slips: (left) initial dSTEC curve before correction, and (right) corrected STEC curve at each step.

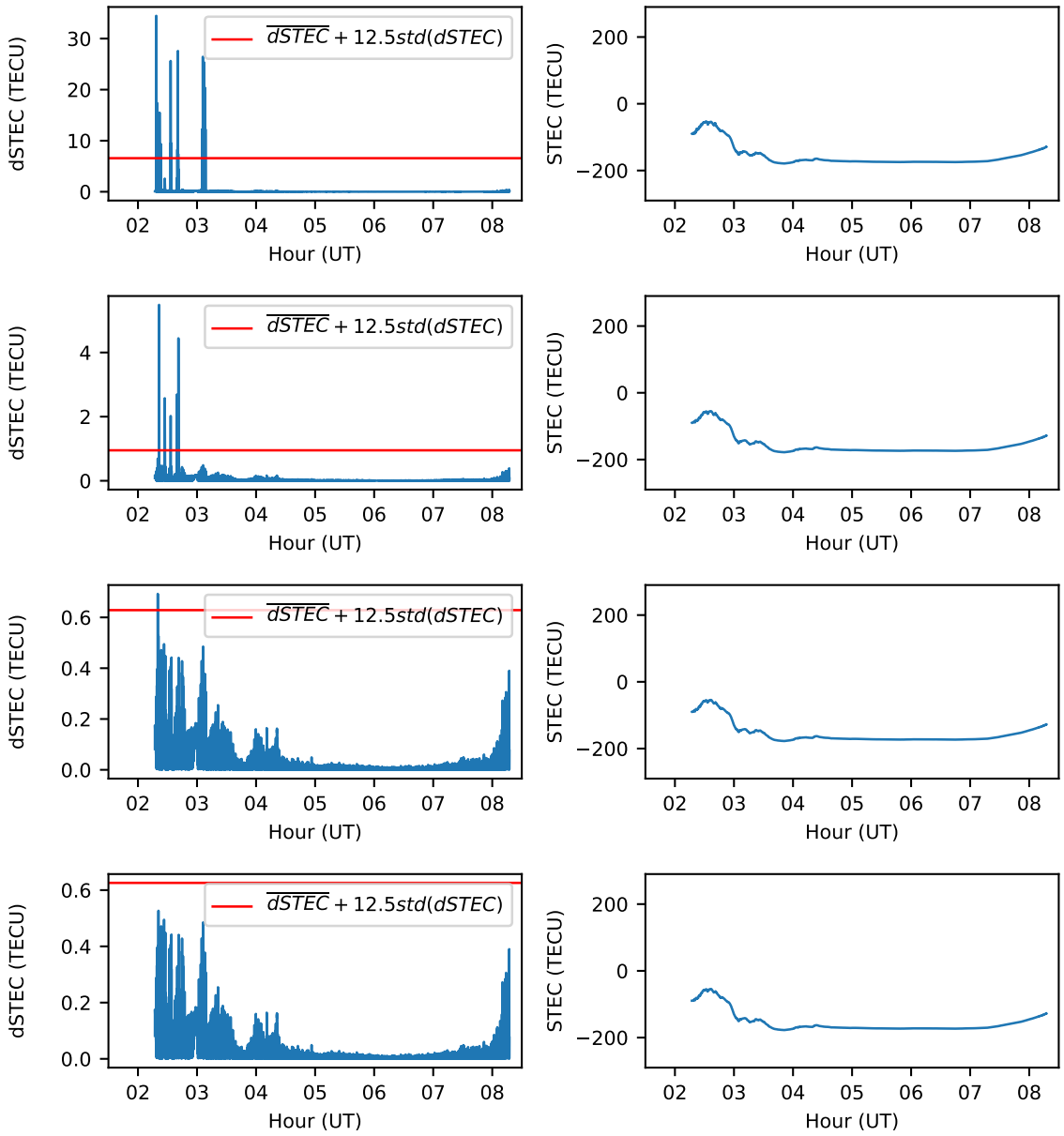

Finally the ROT values can be calculated using the Equation 2.6, resulting in 1 Hz resolution time series, as the data employed in this work present 1 Hz sampling rate. The ROTI time series are then calculated with a 1-minute time interval applying the Equation 2.7 in the ROT time series. It is important to note that a minimum of 80 % of ROT data for each 1 minute is adopted in order to calculate the ROTI values, otherwise a NaN value is assigned.

The data format based on the unified data format presented in Section 3.2 and Section 3.3 was adopted, as shown in Table 3.4. The "i_lat" and "i_lon" values correspond to the IPP coordinates. The "roti" values are classified according to the scintillation severity using the following thresholds: null [0.00-0.04], weak (0.04-0.09], moderate (0.09-0.20], or strong (0.20-0.40) being available in the "class" column. Values of "roti" above 0.4 TECU/s were considered outliers, being rounded to that value. In order to filter out data of L-band links affected by ground interference and the related multipath reflections, only satellite elevations higher than 30° were considered. The "rotiv" value corresponds to the vertical projection of the slant ROTI value, according to Li et al. (2022).

Table 3.4 - Unified ROTI data file format for each ROTI observation.

Field	**Description**
datetime	Day and time in format "yyyy-mm-dd hh:mm:ss".
prn	Satellite identifier.
az	Azimuth (degrees).
el	Elevation (degrees).
roti	ROTI value.
rotiv	Vertical projection of the ROTI value.
class	Scintillation severity classification (0: null; 1: weak; 2: moderate; 3: strong).
station	Acronym of the monitoring station.
r_lat	Monitoring station latitude (degrees).
r_lon	Monitoring station longitude (degrees).
i_lat	IPP latitude (degrees).
i_lon	IPP longitude (degrees).
constellation	GPS, GLONASS, GALILEO or BEIDOU.
network	INCT or RBMC.

4 SCINTILLATION MAPS GENERATION AND CORRELATION ANALYSIS

This chapter presents the generation and correlation analysis of the three scintillation maps that were proposed for scintillation monitoring, which are related to the scintillation indexes S4, σ_ϕ and ROTI. The making of these scintillation maps requires the interpolation of IPP samples, given by the ionospheric scintillation index values (S4, σ_ϕ, or ROTI) for each IPP of each satellite-station link considering the set of GNSS stations of the given area and time interval. Interpolation is performed with the aim of filling in IPP data gaps, resulting in a smoother map for the considered grid in longitude and latitude, and for the integration interval.

These maps were implemented using a new approach (MARTINON et al., 2023) entirely developed in the scope of this thesis. This new approach consists of a set of preprocessing options and an interpolation method. It allows to generate more accurate scintillation maps with a low computational cost that is compatible with real-time demands. Former approaches to investigate ionospheric scintillation over the Brazilian territory include the generation of regional S4 index maps (REZENDE et al., 2007), and Vani (2018) employed different preprocessing options and interpolation methods.

4.1 Approach for generating scintillation maps

The proposed approach (MARTINON et al., 2023) is named GPR(VQI), since it uses the Gaussian Process Regression for interpolation of the samples of a 15-minute interval, and the specific set of preprocessing options VQI, which corresponds to the use of the vertical projection of values of the considered scintillation index reduced by the average value above the 3rd quartile for the group of 15-minute samples of the considered aggregation cell. The interpolation grid has the same spatial resolution of the map ($0.25° \times 0.25°$), spanning latitudes $-39°$ to $9°$ and longitudes $-78°$ to $-30°$, and forming a regular grid of 193×193 grid points. A coarser aggregation grid with $1.0° \times 1.0°$ resolution with square cells centered at each grid point of the map delimitates the grouping of the samples for the considered grid point. The interpolated grid points are generated using the following assumptions:

I. Only samples corresponding to satellite elevations higher than $30°$ are considered, in order to filter out data of L-band links affected by ground interference and the related multipath reflections;

II. Scintillation index samples considered outliers are filtered out, according to the threshold defined in Section 2.3.4;

III. The ionosphere is modeled as a thin spherical shell over the Earth at the mean altitude of 350 km (typically), where the maximum value of the ionospheric electron density is observed;

IV. The IPP for each satellite-receiver link is defined as being the intersection of the line-of-sight receiver-satellite (the slant path) with the ionosphere, using the receiver coordinates and the azimuthal and elevation angles of the satellite (see Section 2.3.6);

V. The scintillation index values are projected to the vertical direction in order to take into account the geometrical effects on the measurements made at different elevation angles (see Section 2.3.5);

VI. An aggregation grid with $1.0° \times 1.0°$ resolution with square cells centered at each grid point of the map is defined to group the 15-minute samples of each cell, and to reduce them to an "interpolation sample" associated with the grid point. The value of each "interpolation sample" is given by the average of the scintillation index values above the 3rd quartile (top 25 % values of the samples contained in the cell of the corresponding grid point). Square cells without samples are discarded;

VII. The centroid of each "interpolation sample" is defined by the reduction function, in this case, the centroid of the group of samples with scintillation index values above the 3rd quartile;

VIII. The interpolation process employs the "interpolation samples", each one with a reduced value and a centroid, to obtain the values for the interpolation regular grid ($0.25° \times 0.25°$), which are then employed to render the scintillation map.

This approach and its correlated assumptions were employed to generate amplitude scintillation maps, using the S4 index, phase scintillation maps, using the σ_ϕ index, and also to generate the ROTI scintillation maps.

4.2 Data description and filtering

The GNSS data used to generate the scintillation maps was obtained from the INCT monitoring stations, which cover only the Brazilian territory. The three types of

scintillation maps were generated for 6 consecutive nights, from 8th to 13th of March, 2023. A total of 27 INCT monitoring stations were available, and the corresponding locations are shown in Figure 4.1. Not all the 27 stations have been continuously operational, with the total number of available stations ranging between 25 and 26. The present study employs all available GNSS constellations for the considered time interval to produce the scintillation maps, except for SBAS satellites which were not included, once this constellation is not suitable to calculate the σ_ϕ index, as discussed in Section 2.3.2.

Figure 4.1 - Geographic location of the 27 GNSS stations of the INCT networks that provided scintillation data for this study.

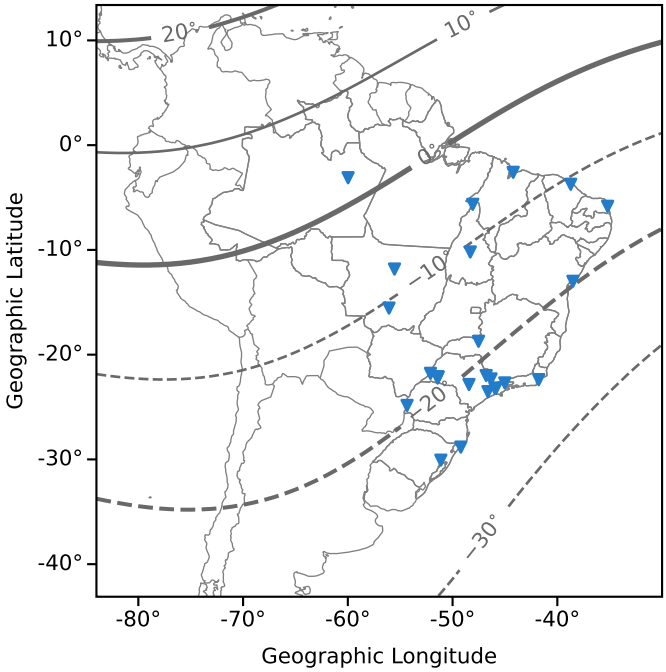

Table 4.1 presents the geographic locations and the magnetic dip latitudes for the 27 INCT monitoring stations. The magnetic dip latitude curves in Figure 4.1 and the values presented in the table were calculated using the IGRF 13 model (ALKEN et al., 2021).

Scintillation data was acquired for the 6 consecutive nights from 8th to 13th of March, 2023 for an interval of time of 8.5 hours, between 20:30 UT and 05:00 UT, which mostly presented moderate and strong scintillation events. Each 8.5-hour interval was divided into 34 consecutive intervals, integrating 14-minute a priori

Table 4.1 - INCT GNSS Ionospheric Monitoring Stations Coordinates.

Station	**City**	**Geographic**		**Magnetic**
		Latitude	**Longitude**	**Dip Latitude**
SLMA	São Luís	−2.5935	−44.2123	−6.8398
STMN	Manaus	−3.1102	−59.9749	2.4746
FRTZ	Fortaleza	−3.7362	−38.7248	−10.8703
STAR	Araguatins	−5.6512	−48.0733	−7.1479
STNT	Natal	−5.8406	−35.1962	−15.2186
PALM	Palmas	−10.1996	−48.3113	−10.7708
STSN	Sinop	−11.8294	−55.5447	−7.6465
UFBA	Salvador	−12.9998	−38.5107	−19.3219
STCB	Cuiabá	−15.5552	−56.0699	−11.0643
STMC	Monte Carmelo	−18.7240	−47.5238	−18.3375
STPE	Presidente Epitácio	−21.7852	−52.1116	−18.1563
STSJ	São João da Boa Vista	−21.9971	−46.7922	−21.2401
PRU4	Presidente Prudente	−22.1201	−51.4085	−18.7546
PRU2	Presidente Prudente	−22.1220	−51.4071	−18.7546
DMC1	Presidente Prudente	−22.1231	−51.4080	−18.7546
MOR3	Presidente Prudente	−22.1277	−51.4133	−18.7546
STPZ	Pirapozinho	−22.2409	−51.4260	−18.7546
INCO	Inconfidentes	−22.3185	−46.3281	−21.8723
STMA	Macaé	−22.3887	−41.7762	−24.4563
STCP	Cachoeira Paulista	−22.7023	−45.0138	−23.2196
SPBO	Botucatu	−22.8525	−48.4323	−21.3238
SJCE	São José dos Campos	−23.2075	−45.8597	−22.5870
SJCU	São José dos Campos	−23.2106	−45.9566	−22.5870
SPSP	São Paulo	−23.5338	−46.6253	−22.6520
STSH	Santa Helena	−24.8470	−54.3444	−19.2025
STBR	Balneário Rincão	−28.8267	−49.2139	−24.6613
POAL	Porto Alegre	−30.0739	−51.1197	−24.1321

IPP data to generate the corresponding sequence of maps using a sliding window of 15-minutes, with no overlap between consecutive maps, resulting in 204 scintillation maps. Please note the interval for error and correlation analysis starts at 20:45, due

to the use of *a priori* data.

Figure 4.2 presents the distribution of the S4, σ_ϕ and ROTI values classified according to the scintillation severity for each night interval using the following thresholds in Table 4.2, as detailed in Section 2.3.4. Although the scintillation maps were generated and evaluated for 8.5-hour intervals, Figure 4.2 presents the data distribution for a shorter time interval, from 22 UT to 03 UT, in which, for moderate solar flux, included most of the ionospheric scintillation occurrences.

Table 4.2 - Four-class scintillation severity thresholds for S4, σ_ϕ and ROTI.

Scintillation Index	**null**	**weak**	**moderate**	**strong**
S4	[0.00-0.15]	(0.15-0.30]	(0.30-0.70]	(0.70-1.40)
σ_ϕ	[0.00-0.15]	(0.15-0.30]	(0.30-0.70]	(0.70-1.40)
ROTI	[0.00-0.04]	(0.04-0.09]	(0.09-0.20]	(0.20-0.40)

Values above the upper limits for the strong class, shown in the table above were considered outliers, being rounded to the corresponding upper limit. In order to filter out data of L-band links affected by ground interference and the related multipath reflections, only satellite elevations higher than 30° were considered. In addition, for each interval, the corresponding values of the planetary Kp geomagnetic index and the adjusted F10.7 index (solar flux at the 10.7 cm wavelength) are presented, showing the absence of geomagnetic storms.

Figure 4.2 - Bar charts showing the distribution of the IPP samples according to the scintillation class of each scintillation index for the 6 consecutive nights, using 4 scintillation severity classes.

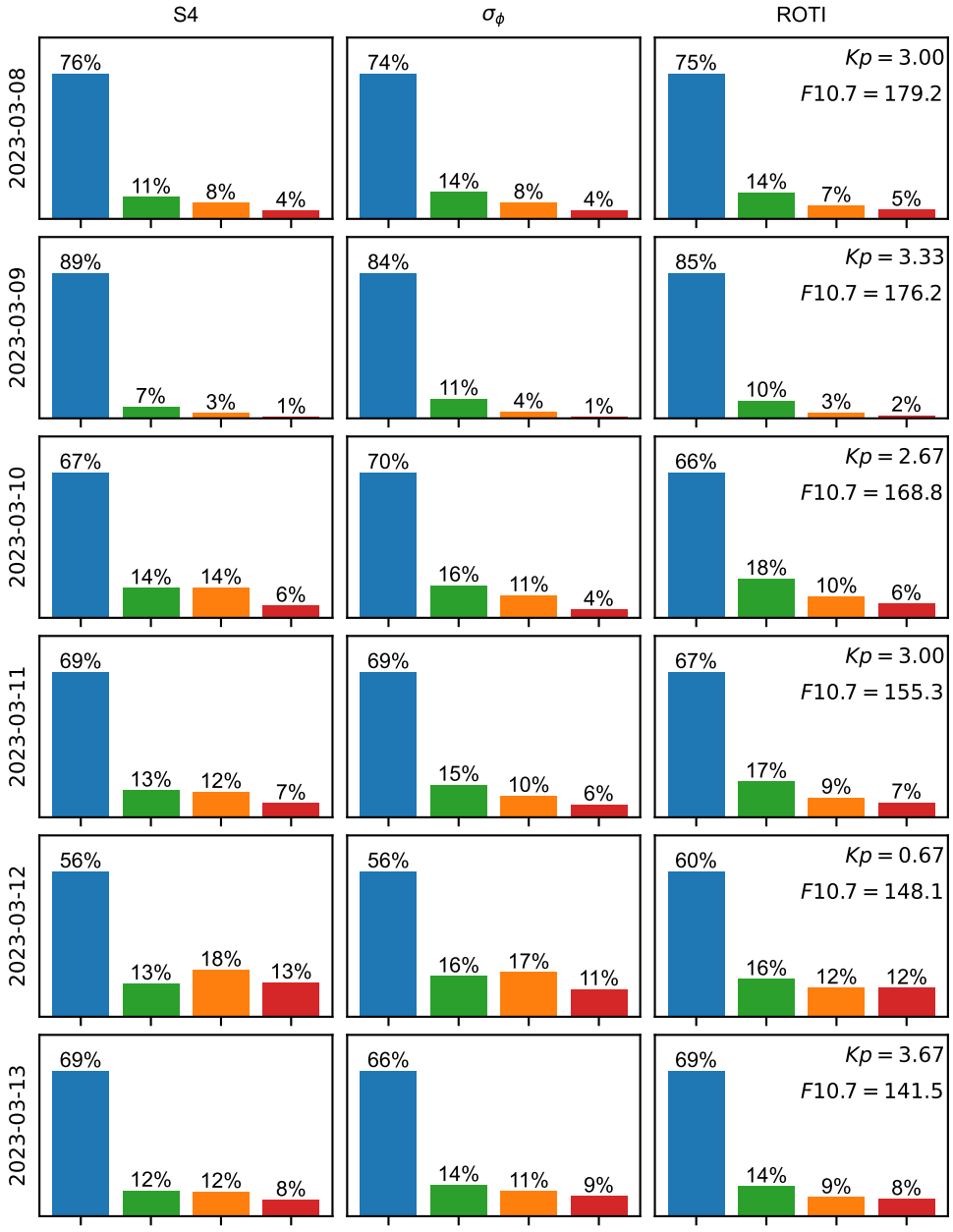

Each row refers to one night of scintillation data (22 UT to 03 UT). The corresponding values of the geomagnetic index Kp and the adjusted F10.7 solar flux index are also shown. Each color bar refers to a scintillation severity class, being: null (blue), weak (green), moderate (orange), and strong (red).

4.3 Interpolation error evaluation

The error evaluation of the GPR(VQI) approach was done for the set of 204 non-overlapping intervals of 15 minutes extracted from the 6 consecutive nights intervals (8.5 hours, from 20:45 UT to 5:00 UT). Scintillation maps were generated using a $0.25° \times 0.25°$ latitude and longitude resolution, covering latitudes 39° to 9° and longitudes 78° to 30°, forming a regular grid of 193×193 grid points. The evaluation of the maps employs each original IPP sample, and compares the corresponding index (S4, σ_ϕ or ROTI) value with the one obtained from the interpolated map. This is achieved by performing a distance-based weighted average of the four grid points of the map that are closer to the IPP sample position. It is important to distinguish between the interpolation points (obtained from the IPP samples) used to interpolate the map, and the test points (IPP samples used to evaluate the map). These two mutually-exclusive sets of IPP samples are obtained from the original set of IPP samples described in the previous section, which is split according to the validation scheme described below.

The Stratified Shuffle Split (SSS) cross-validation was chosen for the evaluation tests. It splits IPP samples into interpolation/test sets using stratified randomized folds, with each fold preserving the percentage of samples for each scintillation class (null, weak, moderate, and strong). An usual 10-fold scheme was chosen, thus the IPP samples in a given 15-minute interval were split into 10 sets, using 9 sets for interpolation and the remaining set, for evaluation. This scheme is repeated 10 times, swapping the evaluation set.

Considering the 204 fifteen-minute intervals, the 10-fold SSS scheme results in 2,040 scintillation maps. Each iteration of the 10-fold scheme employed, in average, 154,627 IPP samples for interpolation and 17,199 for evaluation/test, always considering the GPS, GLONASS, GALILEO and BEIDOU constellations. Therefore, the IPP samples of the test set in each iteration amount to about 10.01 % of the total IPP samples. Table 4.3 presents more detailed information about the IPP samples used in interpolation training and testing, for each night and each scintillation index.

In order to evaluate the generation of the three types of scintillation maps, seven different error and correlation metrics were employed: overall Mean Absolute Error (MAE), overall Root Mean Square Error (RMSE), Mean of Maximum Absolute Errors (MXAE), Mean of Minimum Errors (MMIN), Mean of Maximum Errors (MMAX), overall Standard Deviation of Absolute Error (STDA) and the overall Pearson's Correlation Coefficient (CORR). MXAE, MMIN, and MMAX means are

Table 4.3 - IPP samples for training and testing the interpolator.

Night	S4		σ_ϕ		ROTI	
	Train	**Test**	**Train**	**Test**	**Train**	**Test**
03/08/2023	172,416	19,174	172,416	19,174	146,576	16,304
03/09/2023	155,287	17,274	155,287	17,274	142,227	15,821
03/10/2023	143,386	15,951	143,386	15,951	134,010	14,909
03/11/2023	151,987	16,907	151,987	16,907	153,770	17,103
03/12/2023	159,364	17,723	159,364	17,723	161,727	17,983
03/13/2023	158,940	17,679	158,940	17,679	162,220	18,041

calculated for each map. It is important to note that the CORR metric compares the original IPP sample and the corresponding interpolated sample obtained from each map. The correlation between the three types of scintillation maps is discussed in Section 4.4.

Table 4.4 shows the interpolation error and correlation for the amplitude scintillation maps that were generated for each one of the consecutive 6 nights. These scintillation maps were generated using all available satellites from the GPS, GALILEO, BEIDOU and GLONASS constellations.

Table 4.4 - GPR(VQI) interpolation error metrics and correlation results for the amplitude scintillation maps using the SSS cross-validation scheme.

Night	**MAE**	**RMSE**	**MXAE**	**MMAX**	**MMIN**	**STDA**	**CORR**
03/08/2023	0.0375	0.0731	0.3857	0.3787	−0.2077	0.0628	0.8782
03/09/2023	0.0267	0.0463	0.2858	0.2767	−0.1575	0.0378	0.8375
03/10/2023	0.0454	0.0827	0.4053	0.3984	−0.2189	0.0690	0.8821
03/11/2023	0.0477	0.0879	0.4263	0.4207	−0.2279	0.0739	0.8770
03/12/2023	0.0696	0.1241	0.5126	0.5048	−0.2972	0.1027	0.8718
03/13/2023	0.0492	0.0930	0.4925	0.4840	−0.2590	0.0789	0.8681

The results shown in Table 4.4 are in agreement with the results obtained by Martinon et al. (2023). In that work, MAE, RMSE, MXAE, MMAX, MMIN, STDA, and

CORR values were respectively: 0.0627, 0.1088, 0.5496, 0.5419, −0.3074, 0.0889, and 0.8681.

Table 4.5 - GPR(VQI) interpolation error metrics and correlation results for the phase scintillation maps using the SSS cross-validation scheme.

Night	MAE	RMSE	MXAE	MMAX	MMIN	STDA	CORR
03/08/2023	0.0436	0.0945	0.4801	0.4711	−0.2905	0.0838	0.8416
03/09/2023	0.0257	0.0500	0.3080	0.2912	−0.1940	0.0429	0.8084
03/10/2023	0.0477	0.0957	0.4694	0.4505	−0.3054	0.0830	0.8468
03/11/2023	0.0537	0.1095	0.5603	0.5438	−0.3362	0.0954	0.8271
03/12/2023	0.0942	0.1751	0.8225	0.7881	−0.5436	0.1476	0.8079
03/13/2023	0.0605	0.1229	0.6362	0.6109	−0.3813	0.1070	0.8352

For the phase scintillation maps, the interpolation errors shown in Table 4.5 are higher than the corresponding amplitude scintillation maps for the same night (shown in Table 4.4), except for the MAE metric. The correlation is also worse for phase scintillation maps than for amplitude scintillation maps. The metrics MMAX and MMIN differs too much between these two types of scintillation maps, since phase scintillation maps present more area with moderate and strong scintillation in comparison to the corresponding amplitude scintillation maps, as seen in Figure 4.3, for example.

The interpolation error for the ROTI scintillation maps seen in Table 4.6 cannot be directly compared with the amplitude and phase scintillation maps interpolation errors, since the range of the ROTI values is between 0.0 and 0.4, different from the range between 0.0 and 1.4 of the other two types of maps.

Therefore, given these different ranges, it is better to compare the scintillation severity classes associated with the errors. The MAE values are compatible between the three types of maps. The RMSE values are similar for the phase and ROTI maps, being higher than those of the amplitude maps for all nights, except for the night of 03/12/2023. Most of the MXAE values for the amplitude maps refer to the weak-moderate classes, while for the phase and ROTI maps, refer to the moderate-strong classes, and thus these maps present a higher range of the MMIN and MMAX values, as shown in Figure 4.4 for the corresponding ROTI map, which presented a better

Figure 4.3 - Amplitude scintillation map (left panel) and the corresponding phase scintillation map (right panel) for March 12th, 2023 at 23:15 UT, showing that the latter presents more area with moderate/strong scintillation.

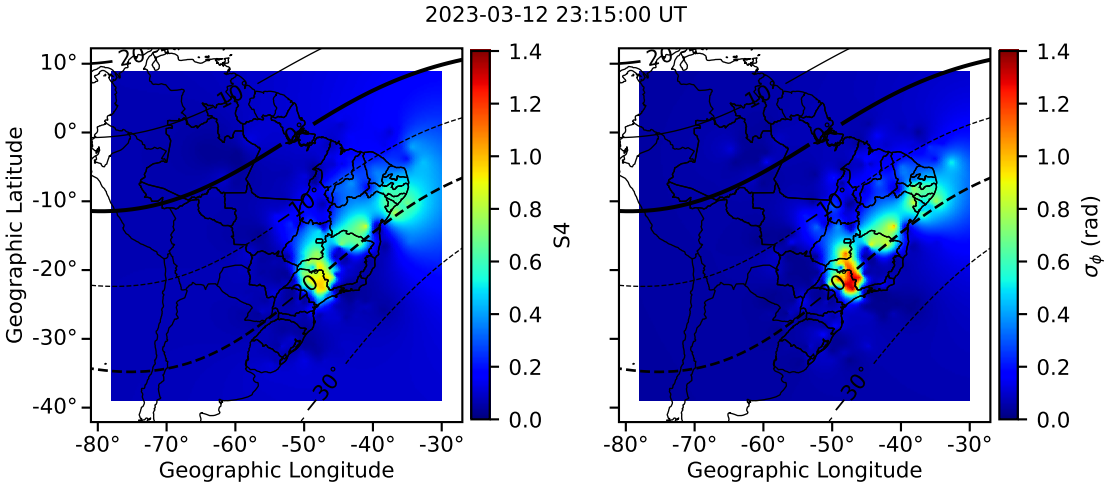

Table 4.6 - GPR(VQI) interpolation error metrics and correlation results for the ROTI scintillation maps using the SSS cross-validation scheme.

Night	MAE	RMSE	MXAE	MMAX	MMIN	STDA	CORR
03/08/2023	0.0090	0.0233	0.1371	0.1328	−0.0766	0.0215	0.8504
03/09/2023	0.0053	0.0127	0.0857	0.0828	−0.0460	0.0115	0.8227
03/10/2023	0.0134	0.0310	0.1431	0.1372	−0.0940	0.0280	0.8361
03/11/2023	0.0137	0.0321	0.1631	0.1569	−0.1016	0.0291	0.8361
03/12/2023	0.0257	0.0519	0.2343	0.2254	−0.1530	0.0451	0.8158
03/13/2023	0.0140	0.0332	0.1839	0.1777	−0.1088	0.0301	0.8388

correlation than the corresponding phase map, but yet lower than the corresponding amplitude map.

Besides the VQI preprocessing options, the amplitude, phase and ROTI scintillation maps were evaluated using the complete set of preprocessing options (12 preprocessing options). The corresponding error evaluation tables, for each type of scintillation map, are available in APPENDIX D - COMPLETE ERROR EVALUATION AND CORRELATION TABLES. These tables allows to conclude that the VQI prepro-

Figure 4.4 - Amplitude scintillation map (left panel) and the corresponding ROTI scintillation map (right panel) for March 12th, 2023 at 23:15 UT, showing that the latter presents more area with moderate/strong scintillation.

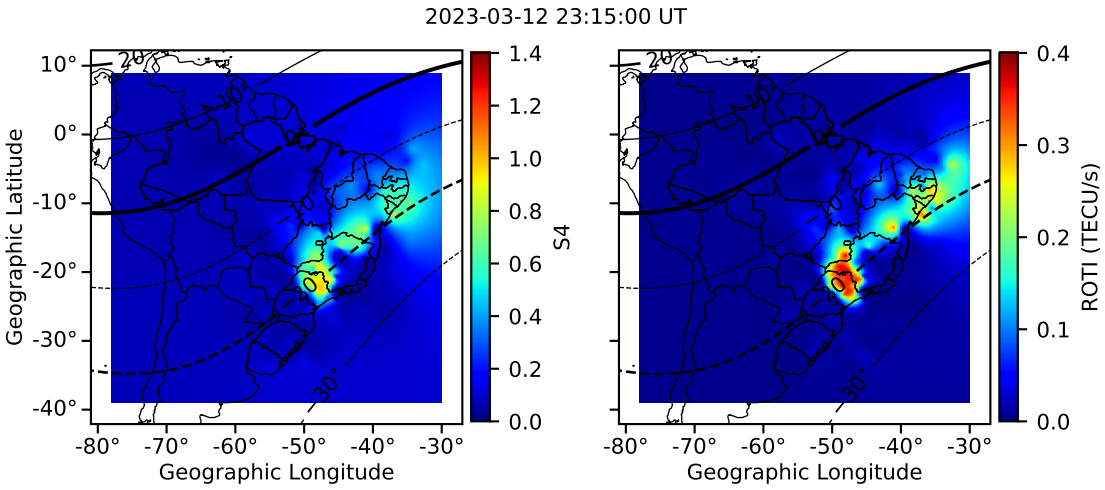

cessing approach performs better than the remaining 11 preprocessing options, in agreement with the results obtained by Martinon et al. (2023).

4.4 Correlation analysis between pairs of different-type scintillation maps

The correlation analysis of the GPR(VQI) approach was done for the set of 204 non-overlapping intervals of 15 minutes extracted from the 6 consecutive night intervals (8.5-hour intervals from 20:45 UT to 5:00 UT). These scintillation maps were generated using a $0.25° \times 0.25°$ latitude and longitude resolution, covering latitudes $-39°$ to $9°$ and longitudes $-78°$ to $-30°$, which corresponds to a regular grid of 193×193 grid points.

Three comparisons were performed in order to analyze the correlation between the different scintillation map types, as follows:

A. Correlation between the amplitude and the phase scintillation maps.

B. Correlation between the amplitude and the ROTI scintillation maps.

C. Correlation between the phase and the ROTI scintillation maps.

Table 4.7 - Correlation between the amplitude and phase scintillation maps for different times of the 6 consecutive nights (comparison A).

Time (UT)	Nights of March, 2023					
	08	09	10	11	12	13
20:45	−23.78	05.55	22.84	12.82	88.53	11.01
21:00	−04.56	14.40	33.08	12.81	83.50	20.13
21:15	02.18	27.55	44.22	−13.84	89.19	36.31
21:30	−16.56	27.42	27.21	−06.96	91.16	46.37
21:45	−02.09	25.88	20.60	−14.90	93.25	27.17
22:00	07.08	18.15	25.28	80.07	83.00	44.99
22:15	88.61	41.57	86.13	91.98	80.35	91.19
22:30	84.44	27.63	94.38	93.16	62.47	97.10
22:45	91.39	07.11	95.55	96.69	93.80	97.41
23:00	95.87	57.04	96.21	91.73	92.75	95.71
23:15	97.66	80.64	96.26	94.75	95.67	98.11
23:30	96.64	93.04	92.87	94.94	96.01	96.25
23:45	95.05	88.90	90.46	94.04	97.30	96.88
00:00	94.96	91.99	92.88	94.81	96.86	95.84
00:15	94.53	90.91	94.63	94.57	95.56	94.47
00:30	95.13	91.02	94.21	93.63	94.84	93.67
00:45	95.44	91.38	88.79	92.31	92.82	91.65
01:00	91.23	89.24	87.70	90.44	93.01	90.71
01:15	91.11	89.53	89.91	90.00	93.14	92.07
01:30	93.25	90.68	88.86	84.76	95.27	90.75
01:45	93.75	90.25	90.54	81.42	94.71	88.67
02:00	91.66	86.71	89.49	86.62	93.48	90.01
02:15	94.18	88.66	89.02	81.08	91.29	90.50
02:30	92.94	86.41	86.82	69.42	91.38	88.29
02:45	89.57	86.41	86.67	81.91	87.77	80.90
03:00	85.01	85.79	79.69	66.91	81.32	80.65
03:15	75.15	85.70	75.26	62.74	68.75	81.66
03:30	59.09	76.94	68.55	76.10	67.21	84.94
03:45	39.85	79.88	59.06	74.34	81.92	81.34
04:00	23.74	54.00	71.40	85.19	71.75	63.16
04:15	02.88	22.37	75.17	86.11	65.63	57.75
04:30	−06.65	−20.13	51.14	66.07	60.41	77.02
04:45	09.20	−31.69	28.10	36.54	43.53	77.33
05:00	−18.10	08.51	−02.90	32.85	35.66	78.85

The evaluation of each pair of scintillation map types was made using the Pearson's Correlation Coefficient. The 193 × 193 matrix of 37,249 grid point values for each map of the 204 scintillation maps, which is represented by the corresponding vector of 37,249 elements in order to calculate the correlation coefficient between each pair of maps. Table 4.7 presents the results for the A comparison, Table 4.8 for the B comparison and Table 4.9 for the C comparison. In these tables, correlation is represented using a color scale that shows in green correlations equal or greater than 90 %, in orange, correlations equal or greater than 80 % and lower than 90 %, and in red correlations lower than 80 %.

The results shown in Table 4.7 for comparison A show weak and/or negative correlation between amplitude and phase scintillation maps mainly before 22 UT and after 03 UT, which corresponds to maps with values lower than those of the weak class, i.e without scintillation. These low values can be considered as noise, thus implying low correlations. However, considering the interval between 22 UT and 03 UT, when scintillation events are more likely to occur, correlations are higher, as it would be expected. The overall correlation coefficient for all nights (22 UT to 03 UT) is 92.26 %, while the overall correlation coefficients for each night, from 08 to 13 of March 2023, are, respectively: 93.50 %, 88.90 %, 91.97 %, 90.08 %, 93.80 %, and 92.54 %.

The results shown in Table 4.8 for comparison B also show weak and/or negative correlation between amplitude and ROTI scintillation maps mainly before 22 UT and after 03 UT, which corresponds to maps with values lower than those of the weak class, i.e without scintillation. These low values can be considered as noise, thus implying low correlations. However, considering the interval between 22 UT and 03 UT, when scintillation events are more likely to occur, correlations are higher, as it would be expected. The overall correlation coefficient for all nights (22 UT to 03 UT) is 92.78 %, while the overall correlation coefficients for each night, 08 to 13 of March 2023, are, respectively: 92.64 %, 89.92 %, 91.73 %, 92.11 %, 94.12 %, and 93.21 %.

Table 4.8 - Correlation between the amplitude and ROTI scintillation maps for different times of the 6 consecutive nights (comparison B).

Time (UT)	Nights of March, 2023					
	08	09	10	11	12	13
20:45	14.63	29.78	32.46	34.53	76.30	24.65
21:00	26.81	44.90	48.09	35.74	68.18	50.90
21:15	38.82	42.64	36.00	49.10	64.41	51.89
21:30	26.07	40.39	11.32	30.41	77.75	54.53
21:45	29.82	43.36	27.62	38.44	78.93	45.92
22:00	32.16	44.31	67.26	92.63	64.59	89.89
22:15	93.63	44.59	81.63	92.60	66.33	89.37
22:30	86.78	23.76	93.20	95.17	58.26	86.67
22:45	86.98	29.05	90.81	98.02	96.57	93.46
23:00	96.39	70.72	95.71	91.88	90.24	91.65
23:15	94.93	71.88	96.11	91.90	95.08	93.82
23:30	95.03	90.55	95.10	94.02	95.21	95.63
23:45	93.48	77.95	93.45	91.35	92.86	95.21
00:00	94.38	86.66	92.70	94.72	95.77	94.40
00:15	93.30	90.70	91.93	93.89	94.39	94.88
00:30	92.51	86.67	91.05	94.39	94.48	94.76
00:45	92.96	91.42	92.26	94.36	94.72	96.27
01:00	93.95	89.12	94.65	92.97	95.08	92.80
01:15	89.59	91.54	91.32	93.43	93.82	94.30
01:30	90.10	93.00	93.13	93.30	93.87	94.59
01:45	91.56	92.05	91.70	89.04	95.71	92.20
02:00	91.05	87.83	90.05	90.80	94.81	93.06
02:15	90.62	91.89	86.48	91.21	93.71	92.53
02:30	92.18	86.17	89.56	85.30	93.26	92.16
02:45	90.57	88.04	87.55	92.78	91.95	92.74
03:00	87.66	87.22	89.00	88.82	87.67	85.69
03:15	85.44	81.02	84.62	80.72	87.43	87.27
03:30	71.10	79.22	78.92	83.35	87.86	85.98
03:45	77.34	83.44	78.24	90.64	90.26	81.11
04:00	58.75	69.66	80.24	91.43	84.04	77.16
04:15	43.84	51.51	83.32	87.82	78.57	79.07
04:30	05.60	32.79	65.26	86.79	70.42	84.91
04:45	40.02	18.47	48.74	64.56	51.26	87.35
05:00	−08.73	16.54	24.71	68.49	47.27	89.83

Table 4.9 - Correlation between phase and ROTI scintillation maps for different times of the 6 consecutive nights (comparison C).

Time (UT)	Nights of March, 2023					
	08	09	10	11	12	13
20:45	67.53	56.04	60.35	54.92	80.88	66.25
21:00	62.32	58.08	45.21	45.61	72.91	58.15
21:15	60.81	55.82	41.17	32.35	70.14	63.32
21:30	57.70	52.24	35.37	27.66	79.85	65.88
21:45	59.74	53.43	38.56	42.27	83.41	44.06
22:00	66.75	35.25	32.52	89.59	73.68	56.95
22:15	96.19	45.37	83.94	93.29	79.43	90.53
22:30	90.78	39.59	94.44	94.71	80.34	87.34
22:45	92.82	47.39	92.98	97.15	96.53	94.33
23:00	97.69	72.27	96.87	96.97	94.74	94.66
23:15	95.15	82.21	95.87	95.51	94.49	94.61
23:30	94.15	93.02	95.63	95.29	96.34	95.20
23:45	93.34	82.75	90.16	94.40	93.01	96.02
00:00	90.93	91.01	87.69	94.97	94.84	94.83
00:15	89.05	88.38	91.92	93.21	92.52	94.70
00:30	92.86	91.76	92.07	94.67	93.15	94.96
00:45	92.42	90.46	93.00	93.98	92.24	92.08
01:00	90.60	90.30	90.71	92.64	91.67	89.58
01:15	88.72	90.12	92.24	88.46	91.85	94.65
01:30	89.90	86.03	91.99	88.05	93.58	94.04
01:45	91.05	87.31	94.02	84.54	94.76	93.88
02:00	91.97	88.16	88.83	83.91	94.88	93.99
02:15	92.51	89.29	89.80	87.15	94.01	96.14
02:30	92.90	90.12	91.72	86.88	95.24	93.64
02:45	92.08	91.55	79.85	83.83	94.92	93.08
03:00	92.52	93.95	83.83	81.25	92.71	91.66
03:15	86.51	88.62	87.26	85.11	88.52	93.80
03:30	86.39	87.89	83.08	90.72	86.78	94.49
03:45	73.71	89.30	67.64	71.09	91.40	94.11
04:00	79.01	66.49	85.90	91.13	92.37	85.94
04:15	60.51	60.44	84.46	87.10	90.33	79.74
04:30	71.57	29.66	77.48	75.85	91.43	85.03
04:45	66.54	16.93	66.22	72.49	83.53	92.82
05:00	64.90	35.03	69.32	69.89	61.98	89.02

The results shown in Table 4.9 for comparison C also show weak and/or negative correlation between phase and ROTI scintillation maps mainly before 22 UT and after 03 UT, which corresponds to maps with values lower than those of the weak class, i.e without scintillation. These low values can be considered as noise, thus implying low correlations, but better than for comparisons A and B since both indexes are calculated using phase measurements, as expressed by Equations 2.3 and 2.5. However, considering the interval between 22 UT and 03 UT, when scintillation events are more likely to occur, correlations are higher, as it would be expected. The overall correlation coefficient for all nights (22 UT to 03 UT) is 92.45 %, while the overall correlation coefficients for each night, 08 to 13 of March 2023, are, respectively: 91.71 %, 87.19 %, 91.92 %, 91.75 %, 93.57 %, and 93.45 %.

4.5 Example of a scintillation map sequence

This section shows a sequence of scintillation maps of each type for the night from March 10th to 11th in 2023: amplitude scintillation (Figure 4.5), phase scintillation (Figure 4.6) and ROTI (Figure 4.7). These sequences of maps can be compared in Figure 4.8, which shows the amplitude scintillation sequence (1st row of maps), the phase scintillation sequence (2nd row of maps) and the ROTI sequence (3rd row of maps). The above sequence of maps were generated by the proposed approach employing INCT data.

Finally, as shown in Figure 4.9, the ROTI map sequence can be generated using (i) only INCT data (1st row of maps), (ii) only RBMC data (2nd row of maps) and (iii) data from both networks (3rd row of maps). It can be observed that as more GNSS stations are employed, more details can be seen in each map of the sequence.

Figure 4.5 - Hourly sequence of amplitude scintillation maps generated by the proposed approach employing INCT data, which shows the evolution of the ionospheric irregularities.

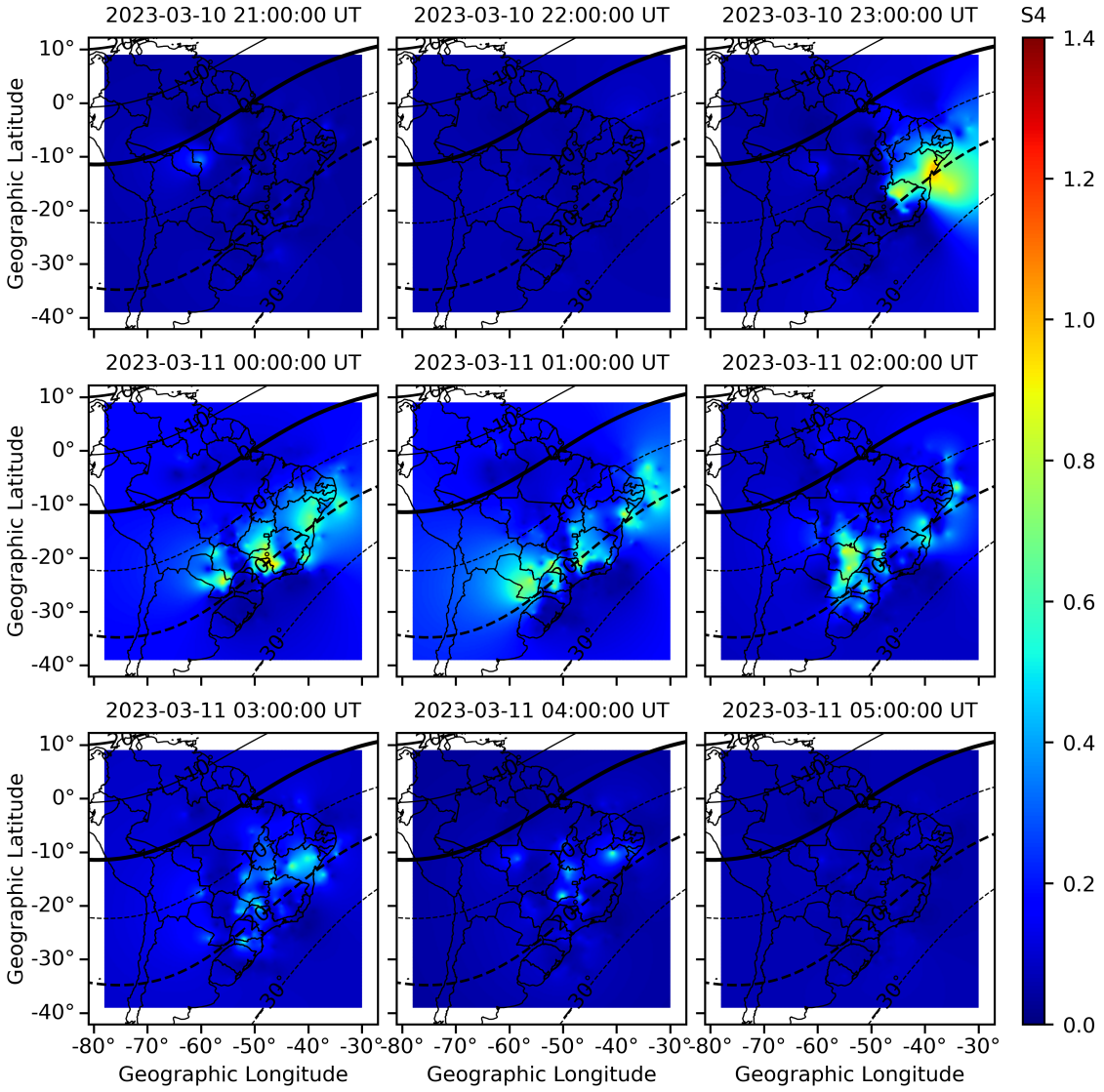

Figure 4.6 - Hourly sequence of phase scintillation maps generated by the proposed approach employing INCT data, which shows the evolution of the ionospheric irregularities.

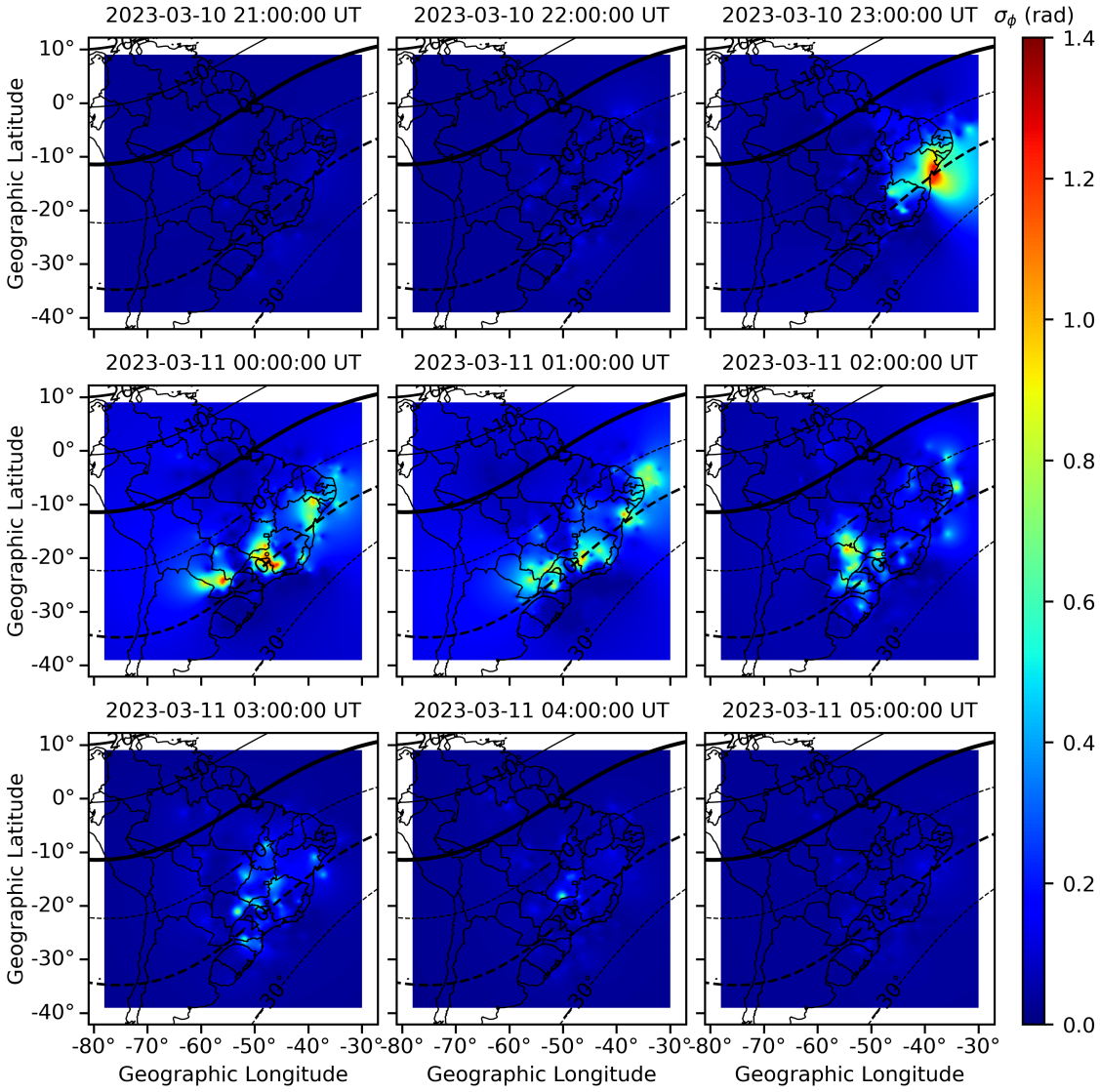

Figure 4.7 - Hourly sequence of ROTI maps generated by the proposed approach employing INCT data, which shows the evolution of the ionospheric irregularities.

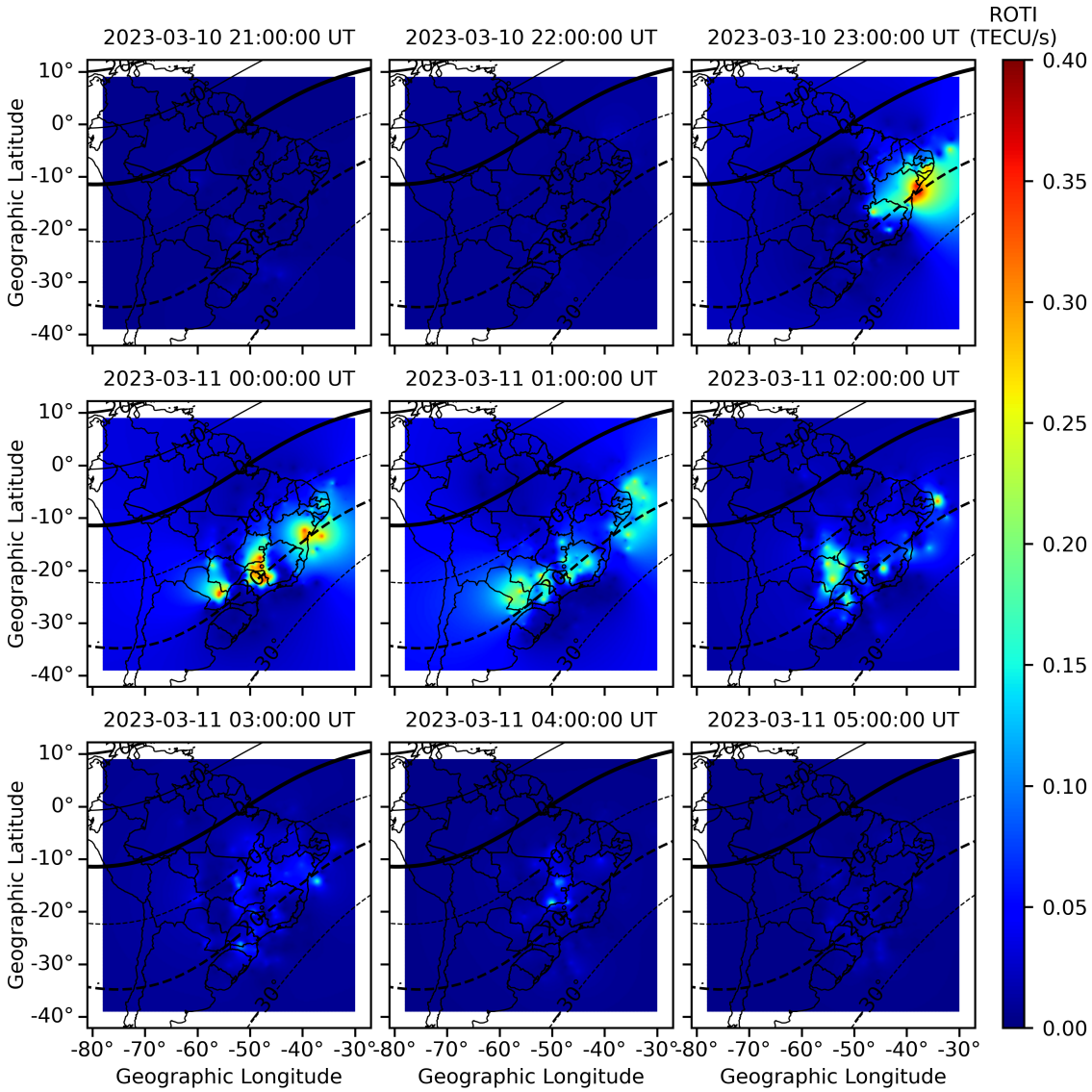

Figure 4.8 - Comparison of amplitude scintillation (1st row of maps), phase scintillation (2nd row of maps) and ROTI (3rd row of maps) maps generated by the proposed approach using INCT data.

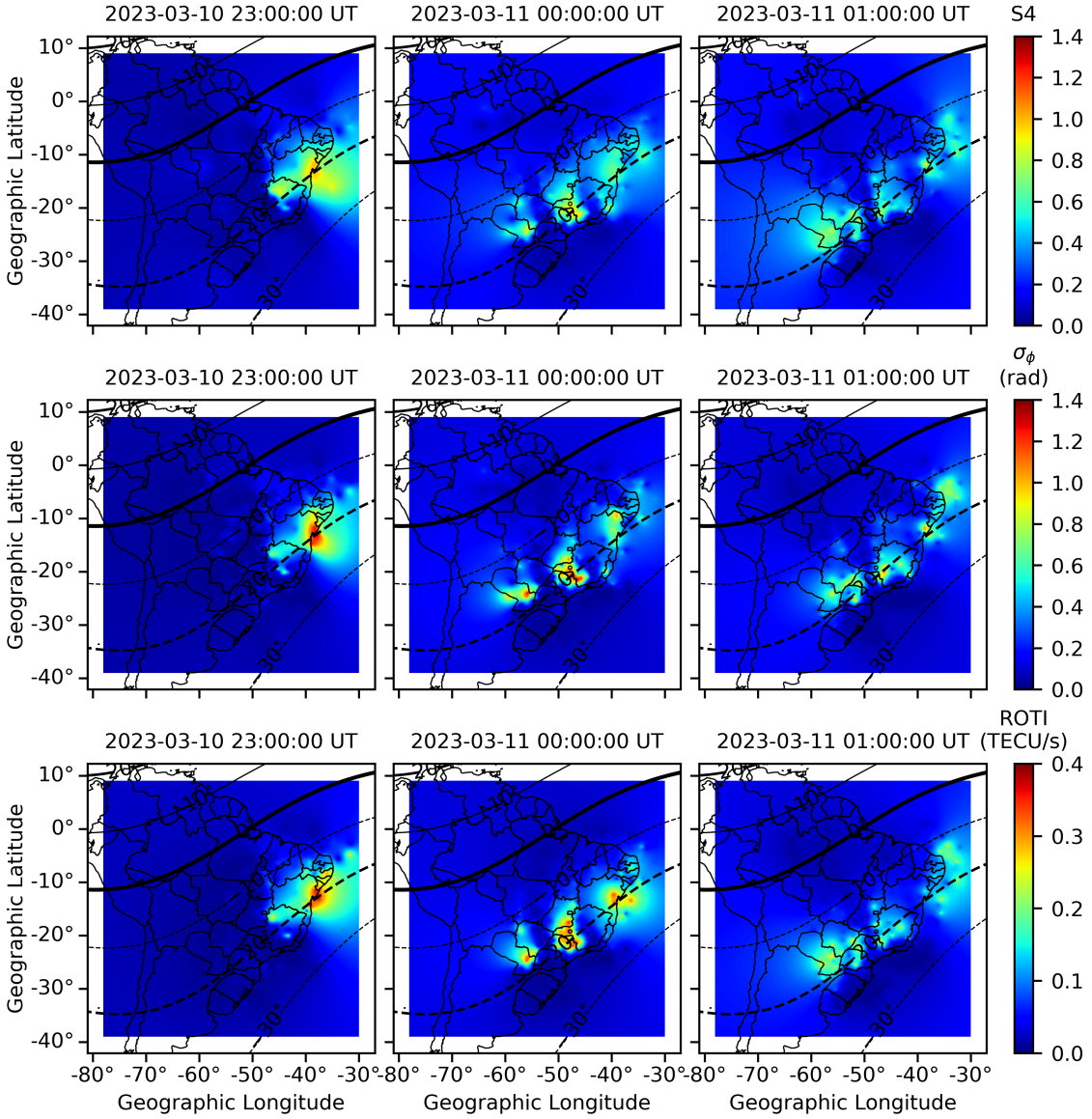

Figure 4.9 - Comparison between ROTI maps generated by the proposed approach, using only INCT data (1st row of maps), only RBMC data (2nd row of maps) and using data from both networks (3rd row of maps).

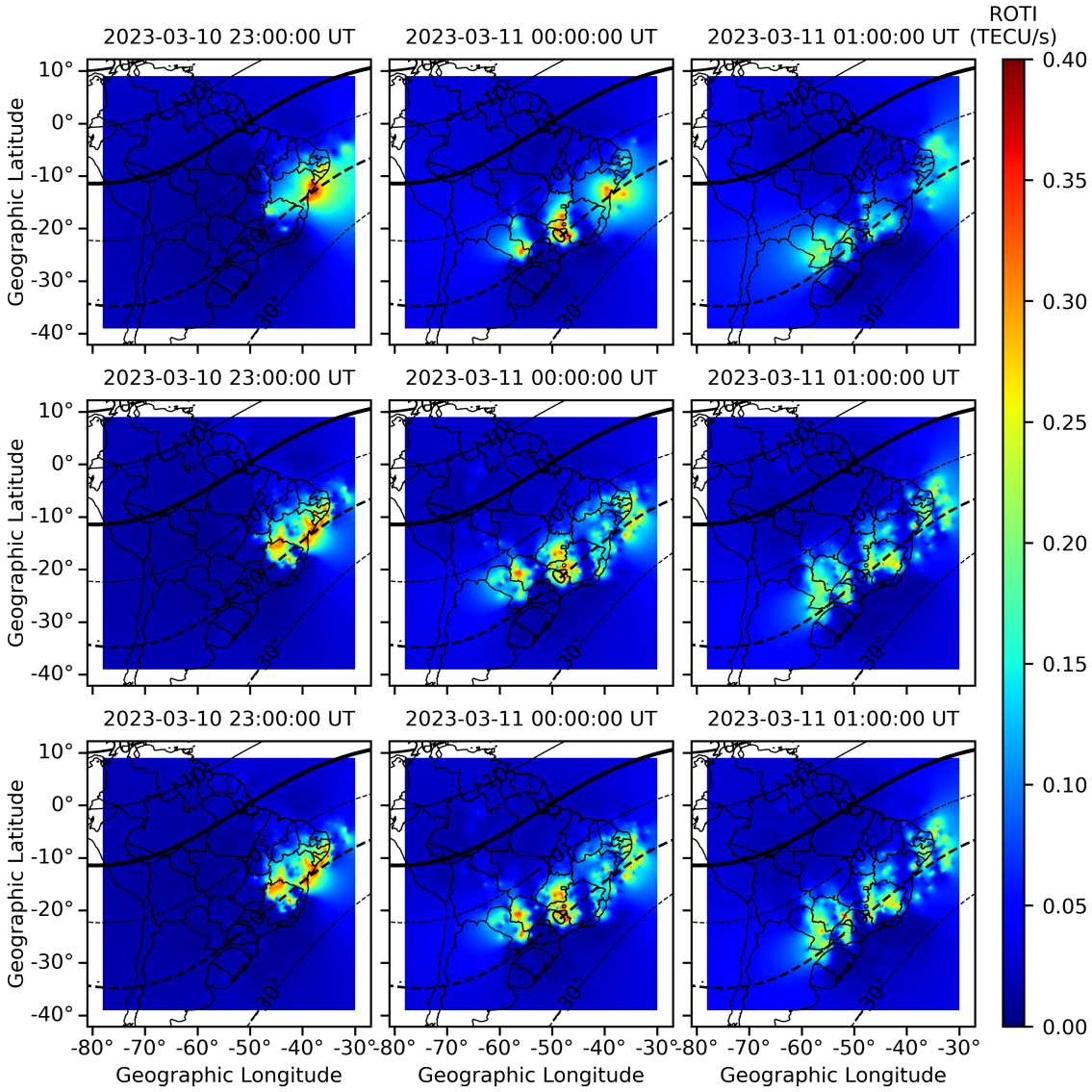

4.6 Discussion and conclusions

The correlation analysis of the maps of the scintillation indexes S4, σ_ϕ and ROTI shows that any of these maps can provide suitable scintillation monitoring. However, ROTI maps can be more accurate for scintillation monitoring depending on the region considered, since they are generated using standard TEC data derived from

GNSS signals. In this work, amplitude and phase scintillation data are provided by 27 INCT stations, a number that reached 32 stations in 2024. Considering only amplitude scintillation data, there are 15 LISN stations in Brazil plus other LISN 26 stations abroad. In comparison, the IBGE RBMC network can provide up to 147 stations, providing GNSS data that allows calculating the ROTI. Consequently, TEC and thus ROTI data are obtained using the IBGE GNSS network, with much more and better distributed stations. The next chapter presents the three probability maps that correspond to the maps of these three indexes, in order to check if they are better for scintillation monitoring.

5 ANALYSIS OF THE CORRESPONDING PROBABILITY MAPS

This chapter presents the generation, error evaluation and correlation analysis of the new probability maps that are generated from the corresponding maps of the scintillation indexes S4, σ_ϕ and ROTI presented in the preceding chapter. Instead of interpolating values corresponding to index values at IPPs, the probability maps are generated from a set of scintillation probability values at each grid point.

Maps of probability of occurrence of scintillation are an innovative concept, entirely developed in the scope of this thesis. The use of probability maps for strong amplitude scintillation (S4 values above 0.7), and restricted to the GPS constellation, was already proposed in Martinon et al. (2022). However, the probability maps generated in this chapter have been extended to use the same GNSS constellations as the scintillation maps shown in the preceding chapter, i.e. BEIDOU, GALILEO, GLONASS, and GPS.

These probability maps take into account elevation and azimuthal angles of each GNSS satellite-station link, and thus are expected to provide a better awareness of scintillation occurrence to the users, since GNSS services can be affected by strong ionospheric scintillation, causing loss-of-lock or positioning error. Scintillation maps covering Brazil can be made available in near real time, as seen in Chapter 7, yielding the vertical projection of a scintillation index at every grid point with a given time resolution, as seen in Chapter 4.

Standard scintillation maps of any scintillation index are intended to be a representation of the occurrence of scintillation in the ionosphere. However, considering a scintillation map for a particular time interval, a GNSS receiver at a given latitude and longitude will not experience the scintillation effects corresponding to its location in the scintillation map, since the azimuthal and elevation angles of each satellite-receiver link are not taken into account. Therefore, the new scintillation probability maps are proposed, which provide for every grid point a probability of a receiver undergoing scintillation in function of the average positions of the set of GNSS satellites within reach in the considered time interval.

Satellite positions can be promptly estimated using data from IGS “Precise Satellites Orbits”, which describes the satellite orbits. Consequently, neighboring scintillation occurrences are taken into account in the probability map, providing GNSS users a better awareness of being affected by strong scintillation near or at their position.

The probability maps proposed in this thesis are specific for GNSS applications, but the same approach can be easily adapted for remote sensing satellites, by taking into account the scan angle to nadir for each swath of the considered onboard sensor. The same scintillation map may then be employed to generate customized probability maps, according to the remote sensing satellite orbit and scan angle. Besides the GNSS satellites/receivers, other satellites that transmits and/or receives electromagnetic signals in the L-band may be affected by ionospheric scintillation, as in the case of satellites equipped with L-SAR (L-band Synthetic Aperture Radar) sensors. On the other hand, distortions in SAR images caused by scintillation may allow to identify ionospheric bubbles (SATO et al., 2021), large structures of depleted plasma that contain high density gradients associated with the occurrence of scintillation.

5.1 Proposed methodology for scintillation probability maps

This work proposes the making of scintillation probability maps of the corresponding scintillation index maps for the same area and time interval. Such maps provide for a receiver location the probability of undergoing scintillation, in this case, strong amplitude scintillation (S4 above 0.70), but can be generated for any other scintillation level, such as null [0.00-0.15], weak (0.15-0.30], or moderate (0.30-0.70]. Different scintillation levels or ranges may be adopted if required. Scintillation probability maps can also be derived for phase scintillation and ROTI maps.

The resulting probability maps have the same geographic boundaries of the corresponding scintillation maps, thus covering latitudes $-39°$ to $9°$ and longitudes $-78°$ to $-30°$, and a regular grid with $1.0° \times 1.0°$ resolution, resulting in 49×49 grid points. The probability of scintillation occurrence is calculated for every grid point of the probability grid, retrieving the scintillation index values of neighboring points of the scintillation map. Considering a hypothetical receiver centered at the grid point, these neighboring points are defined using the positions of the set of in-range GNSS satellites, thus taking into account the elevation and azimuthal angles of the line-of-sight satellite-station. Only lines-of-sight with elevation angle higher than $30°$ are considered.

Each GNSS satellite position can be calculated by the available IGS satellite orbital data. The hypothetical receiver is assumed as locking up all satellites in its vicinity, thus defining a set of surrounding IPPs, each one with a scintillation index value obtained from the corresponding scintillation map. The probability at the grid point is then simply given by the ratio of IPPs with strong scintillation (or any other level) and the total number of IPPs. The probability maps, for a determined time interval,

are generated using the following steps/assumptions:

I. From an IGS FTP mirror, the precise ephemeris data are automatically downloaded for each day in the corresponding scintillation maps, and also for the corresponding GNSS constellations used to generate the scintillation maps;

II. The orbits of each satellite, for all GNSS constellations, are interpolated with 1-minute resolution using the precise ephemeris data;

III. A probability grid with $1.0° \times 1.0°$ resolution is defined, where each grid point represents the location of a hypothetical receiver;

IV. Considering the coordinates of each grid point, the elevation and azimuthal angles of each satellite-receiver lines-of-sight are calculated, but only for elevations above 30°;

V. The ionosphere is modeled as a thin spherical shell over the Earth at the mean altitude of 350 km (typically), where the maximum value of the ionospheric electron density is observed;

VI. The IPP for each satellite-receiver link is defined as being the intersection of the line-of-sight receiver-satellite (the slant path) with the ionosphere, using the hypothetical receiver coordinates and the azimuthal and elevation angles of the satellite (see Section 2.3.6);

VII. Grid points near the boundaries of the grid will present IPPs outside the corresponding scintillation map area. In this case, the adopted criteria was to mirror the outside IPPs coordinates to the respective coordinates inside the scintillation map area;

VIII. The scintillation index values for each IPP are retrieved from the corresponding scintillation map interpolating the 4 closest neighboring scintillation index values. As the scintillation maps were generated using the vertical projection of the scintillation index, the retrieved scintillation index value is then projected to the slant path rearranging the corresponding Equation 2.8, 2.10, or 2.11, presented in Section 2.3.5;

IX. Finally, the probability at the grid point is then simply given by the ratio of IPPs with each scintillation level and the total number of IPPs.

The resulting probability map is provided in a CSV format file, which contains the latitude and longitude of each grid point and the respectives probabilities for each scintillation level.

5.2 Data description

In Chapter 4, a set of 204 scintillation maps using non-overlapping intervals of 15 minutes from 6 consecutive nights (from 8th to 13th of March, 2023) were generated using the GPR(VQI) for each the three types of scintillation indexes: S4, σ_ϕ and ROTI. This set of 204 scintillation maps for each scintillation index were used to generate the corresponding probability maps shown in this chapter.

The data distribution used in this study has a strong imbalance between the 4 scintillation classes adopted in Chapter 4, which are: null, weak, moderate and strong. These classes were defined in Table 4.2, and Figure 4.2 shows that there are few IPPs with strong scintillation. To investigate the use of the probability maps for the occurrence of strong scintillation such imbalance in the classes must be minimized, otherwise the resulting probabilities maps will present few grid points with strong scintillation. The class imbalance in the data was alleviated by reducing the scintillation classes to only three, which are: null, weak-moderate, and moderate-strong. The thresholds of the new classes are shown in Table 5.1. The percentage of IPP samples using this new three-class scintillation severity classification obviously resulted in a higher percentage of IPP samples with moderate-strong scintillation (as seen in Figure 5.1), in comparison to the percentage of IPP samples with strong scintillation shown in Figure 4.2.

Table 5.1 - Three-class scintillation severity thresholds for S4, σ_ϕ and ROTI for the generation of probability maps.

Scintillation Index	**null**	**weak-moderate**	**moderate-strong**
S4	[0.00-0.15]	(0.15-0.50]	(0.50-1.40)
σ_ϕ	[0.00-0.15]	(0.15-0.50]	(0.50-1.40)
ROTI	[0.00-0.04]	(0.04-0.14]	(0.14-0.40)

Although the probability maps derived from the scintillation maps were generated

Figure 5.1 - Bar charts showing the distribution of the IPP samples according to the scintillation class of each scintillation index for the 6 consecutive nights using 3 scintillation severity classes.

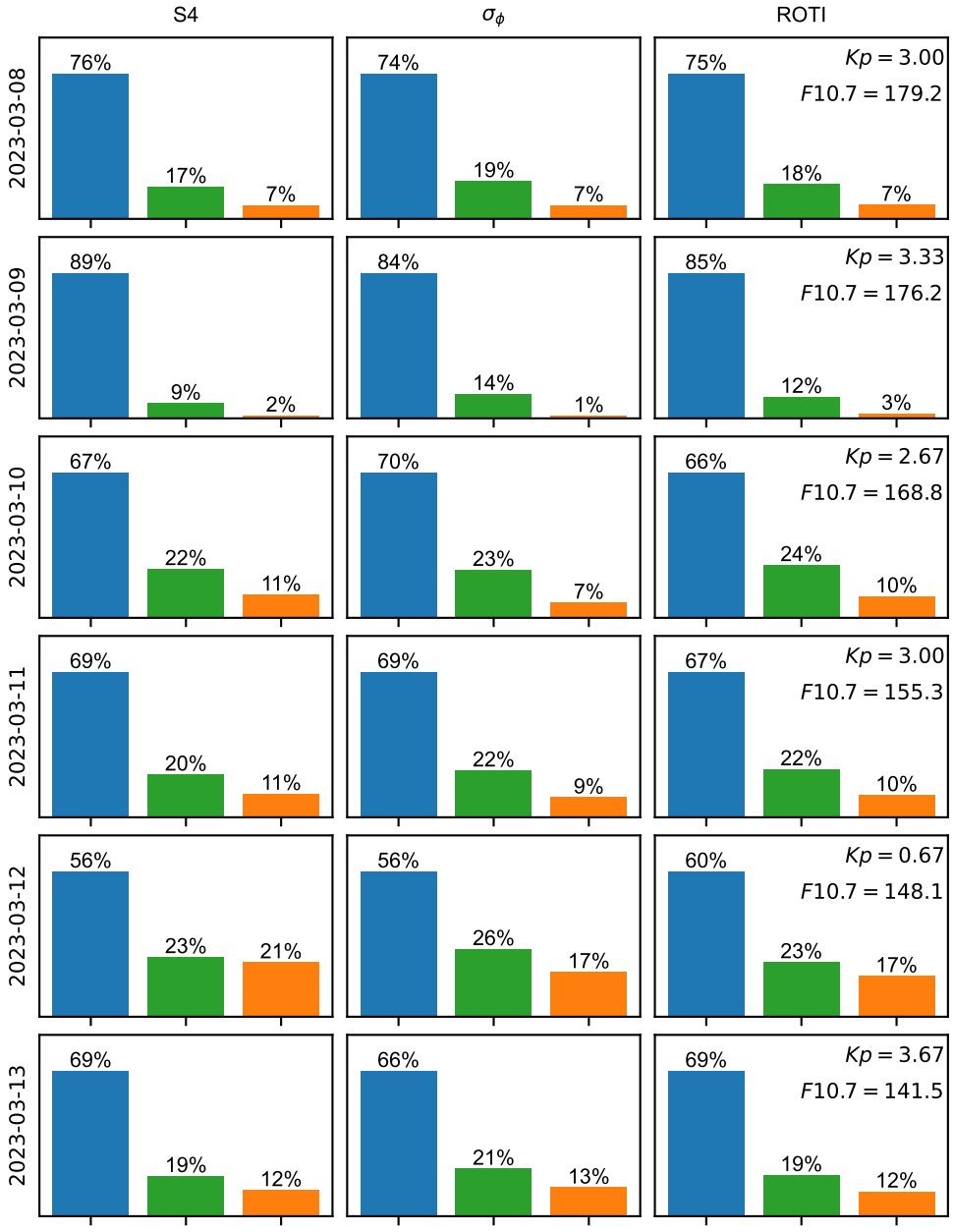

Each row refers to one night of scintillation data (22 UT to 03 UT). The corresponding values of the geomagnetic index Kp and the adjusted F10.7 solar flux index are also shown. Each color bar refers to a scintillation severity class, being: null (blue), weak to moderate (green), moderate to strong (orange).

and evaluated for 8.5-hour intervals, Figure 5.1 presents the data distribution for a shorter time interval, from 22 UT to 03 UT, in which, for moderate solar flux, the

ionospheric scintillation occurs.

5.3 Error evaluation

Error evaluation for the probability maps was done for the set of 204 fifteen-minute intervals extracted from the 6 consecutive nights intervals from 20:45 UT to 05:00 UT, comprehending 8.5 hours or 34 fifteen-minute non-overlapping intervals for each night, which were selected as presenting moderate-strong scintillation (as seen in Figure 5.1) over the Brazilian territory.

The probability maps were derived from the scintillation maps, using the moderate-strong scintillation level (Table 5.1). The scintillation maps were generated using the GPR(VQI) approach with $0.25° \times 0.25°$ latitude and longitude resolution, covering latitudes $-39°$ to $9°$ and longitudes $-78°$ to $-30°$, which corresponds to a regular grid of 193×193 grid points. However, the derived probability maps were generated using the coarser $1° \times 1°$ latitude and longitude resolution, covering latitudes $-39°$ to $9°$ and longitudes $-78°$ to $-30°$, which corresponds to a regular grid of 49×49 or 2,041 grid points.

Evaluation of the probability maps is done in a different way than the evaluation of the scintillation index maps of the former chapter. A set of inferred probabilities is estimated from the considered probability map (amplitude, phase or ROTI), composed of a vector of dimension N given by the probability of occurrence of scintillation of each GNSS station (total of N stations that may vary from map to map). A set of true probabilities is calculated from the actual scintillation data, composing a similar vector given by the true probability of occurrence of the N stations. The evaluation then compares, for the considered time interval, the error of the inferred probability vector with the true probability vector, and similarly calculates the correlation between these two vectors.

The set of inferred probabilities is obtained from the moderate-strong probability maps by interpolating the probability values of the four closest grid points according to the location of each of the N considered GNSS stations (locations shown in Table 4.1) for the considered time interval. The set of true probabilities for each of these N stations is simply given by the ratio of IPP samples of the moderate-strong class and the total number of IPPs, also for the considered time interval.

Seven different error and the correlation metrics were employed in the comparison of the true set and the inferred set: overall MAE, overall RMSE, MXAE, MMIN,

MMAX, overall STDA and the overall CORR. MXAE, MMIN, and MMAX means are calculated for each map. It is important to note that the CORR metric evaluates the correlation between two vectors, the inferred set of probabilities and the corresponding true set.

In the preceding chapter, the considered 204 scintillation maps for the 3 ionospheric indexes (amplitude and phase scintillation and ROTI) were generated using the proposed approach for the 12 preprocessing options, combining operators to reduce the scintillation index values for grouped IPPs (using mean, max, or 3rd quartile), and the use of slant or vertically-projected scintillation values. As already stated, the VQI preprocessing option was chosen since it yielded lower errors and better correlations. In this chapter, the best probability maps were derived from the corresponding scintillation maps using the VQI option, as assessed by the error and correlation analysis, as shown in Tables 5.2, Table 5.3, and Table 5.4, for the probability maps derived from the amplitude scintillation maps, phase scintillation maps and ROTI maps, respectively. Probability maps were generated using all available satellites from the GPS, GALILEO, BEIDOU and GLONASS constellations. The complete evaluation for the probability maps derived from the scintillation maps for all the 12 preprocessing options is available in APPENDIX E - PROBABILITY MAPS COMPLETE ERROR EVALUATION AND CORRELATION TABLES for the three types of probability maps.

Table 5.2 - Error metrics and correlation results for the probability maps derived from amplitude scintillation maps for the considered 6 consecutive nights.

Night	**MAE**	**RMSE**	**MXAE**	**MMAX**	**MMIN**	**STDA**	**CORR**
03/08/2023	2.5056	5.7187	10.9247	10.3962	−0.8591	5.1406	0.9529
03/09/2023	0.6224	2.3051	4.3004	3.9319	−0.9306	2.2195	0.9166
03/10/2023	3.2327	6.8387	12.9655	12.5047	−1.2686	6.0264	0.9554
03/11/2023	3.3734	6.9519	12.6518	12.5839	−0.9946	6.0786	0.9633
03/12/2023	6.7197	12.2782	18.4029	18.2842	−0.8346	10.2762	0.9707
03/13/2023	3.6554	7.6215	17.3673	17.2222	−0.8344	6.6877	0.9674

The results shown in Table 5.2 for the amplitude scintillation probability maps present lower errors, mainly for the MMAX and MMIN metrics, and better correlations compared to the results obtained by Martinon et al. (2022), which were

obtained using only the GPS constellation. The improved results shown here can be explained by the use of all available GNSS constellations.

Table 5.3 - Error metrics and correlation results for the probability maps derived from phase scintillation maps for the considered 6 consecutive nights.

Night	MAE	RMSE	MXAE	MMAX	MMIN	STDA	CORR
03/08/2023	2.2352	5.2259	9.8234	9.3237	−0.9538	4.7238	0.9630
03/09/2023	0.3946	1.6521	3.0799	2.2764	−1.1691	1.6043	0.8813
03/10/2023	2.3754	5.5089	9.6802	8.9667	−1.6396	4.9705	0.9340
03/11/2023	3.0814	7.1001	11.7366	11.4512	−1.3778	6.3966	0.9552
03/12/2023	8.1412	14.3527	26.9965	26.9965	−1.1557	11.8204	0.9560
03/13/2023	3.5785	7.8362	17.3262	16.9106	−1.0972	6.9714	0.9688

Comparing the results for the phase probability maps, shown in Table 5.3, with the results for the amplitude probability maps, it can be observed lower errors, mainly in nights with less scintillation activity, but higher errors in nights with more scintillation activity. Such behavior was also observed for the ROTI probability maps shown in Table 5.4.

Table 5.4 - Error metrics and correlation results for the probability maps derived from ROTI scintillation maps for the considered 6 consecutive nights.

Night	MAE	RMSE	MXAE	MMAX	MMIN	STDA	CORR
03/08/2023	2.5898	5.7198	10.2504	10.1345	−0.4611	5.0999	0.9613
03/09/2023	0.4567	1.7592	3.4922	2.9139	−0.9453	1.6989	0.8981
03/10/2023	3.6509	7.8252	12.3967	12.1353	−0.7464	6.9213	0.9403
03/11/2023	3.6040	7.6273	12.9093	12.5586	−1.5137	6.7221	0.9611
03/12/2023	8.8621	15.2501	24.6554	24.5340	−0.8284	12.4108	0.9689
03/13/2023	4.3037	8.9243	19.4150	19.2942	−0.8210	7.8180	0.9673

5.4 Correlation analysis between pairs of different-type probability maps

The same comparisons between pairs of maps of different types shown in Section 4.4 for amplitude scintillation, phase scintillation and ROTI maps is performed here, but for the corresponding pairs of probability maps:

A. Correlation between the amplitude and the phase probability maps.

B. Correlation between the amplitude and the ROTI probability maps.

C. Correlation between the phase and the ROTI probability maps.

The evaluation of each pair of probability scintillation map types was also done for the set of 204 non-overlapping intervals of 15 minutes extracted from the 8.5-hour intervals from 20:45 UT to 5:00 UT for the 6 consecutive nights.

Table 5.5 presents the results for the A comparison, Table 5.6 for the B comparison and Table 5.7 for the C comparison. In these tables, correlation is represented using a color scale that shows in green the correlations equal or greater than 90 %, in orange, correlations equal or greater than 80 % and lower than 90 %, and in red correlations lower than 80 %. In these tables, the N/A (not applicable) values were used when the pair of probability maps do not present scintillation probability, which results in a variance of zero and in a division by zero when the Pearson's correlation coefficient is calculated.

Table 5.5 shows that, considering the interval between 22 UT and 03 UT, when scintillation events are more likely to occur, correlations are higher, as it would be expected. The overall correlation coefficient for all nights (22 UT to 03 UT) is 90.49 %, while the overall correlation coefficients for each night, from 08 to 13 of March 2023, are, respectively: 91.51 %, 82.43 %, 85.77 %, 85.77 %, 93.63 %, and 94.20 %.

Table 5.6 shows that, considering the interval between 22 UT and 03 UT, when scintillation events are more likely to occur, correlations are higher, as it would be expected. The overall correlation coefficient for all nights (22 UT to 03 UT) is 93.89 %, while the overall correlation coefficients for each night, from 08 to 13 of March 2023, are, respectively: 92.86 %, 83.66 %, 92.68 %, 91.13 %, 95.28 %, and 95.97 %.

Table 5.5 - Correlation between amplitude and phase probability maps for different times of the 6 consecutive nights (comparison A).

Time (UT)	Nights of March, 2023					
	08	09	10	11	12	13
20:45	N/A	N/A	N/A	N/A	25.39	N/A
21:00	N/A	N/A	N/A	N/A	8.47	N/A
21:15	N/A	N/A	N/A	N/A	16.56	N/A
21:30	N/A	N/A	N/A	N/A	10.31	N/A
21:45	N/A	N/A	N/A	N/A	N/A	N/A
22:00	N/A	N/A	N/A	−0.04	N/A	N/A
22:15	82.27	N/A	49.63	93.72	10.19	77.83
22:30	46.99	N/A	68.10	89.65	4.14	95.75
22:45	N/A	N/A	96.05	87.96	95.64	98.26
23:00	89.46	100.00	95.55	96.50	85.24	97.19
23:15	98.26	45.41	88.78	88.86	91.59	98.85
23:30	95.27	94.13	83.97	86.83	93.98	98.54
23:45	95.40	48.91	81.38	90.19	96.96	98.42
00:00	94.21	55.53	83.11	92.35	96.86	98.01
00:15	90.64	87.00	84.89	91.23	96.79	94.42
00:30	93.77	86.92	88.82	89.45	96.54	94.20
00:45	89.85	92.50	85.73	89.97	94.47	92.87
01:00	84.29	84.57	80.17	86.74	95.46	91.50
01:15	89.84	80.52	83.58	85.92	96.04	91.41
01:30	93.59	85.42	86.21	77.39	95.22	96.46
01:45	94.97	62.07	83.05	55.16	95.30	94.50
02:00	94.67	57.92	86.21	62.20	94.43	90.07
02:15	95.13	69.60	80.76	68.63	94.14	93.88
02:30	94.13	53.56	57.86	61.27	92.63	87.38
02:45	84.61	51.47	66.28	86.58	73.88	79.26
03:00	79.82	63.78	43.73	64.13	75.12	89.87
03:15	4.46	79.58	51.72	43.91	47.88	87.10
03:30	8.96	10.31	−0.46	53.55	46.22	79.86
03:45	−0.31	53.60	N/A	41.58	61.87	26.06
04:00	N/A	N/A	40.48	89.39	34.64	N/A
04:15	N/A	N/A	N/A	66.57	48.01	N/A
04:30	N/A	N/A	N/A	N/A	40.39	39.88
04:45	N/A	N/A	N/A	N/A	N/A	68.88
05:00	N/A	N/A	N/A	N/A	N/A	51.15

Table 5.6 - Correlation between amplitude and ROTI probability maps for different times of the 6 consecutive nights (comparison B).

Time (UT)	Nights of March, 2023					
	08	09	10	11	12	13
20:45	N/A	N/A	N/A	N/A	10.63	N/A
21:00	N/A	N/A	N/A	N/A	5.49	N/A
21:15	N/A	N/A	N/A	N/A	8.46	N/A
21:30	N/A	N/A	N/A	N/A	7.07	N/A
21:45	N/A	N/A	N/A	N/A	N/A	N/A
22:00	N/A	N/A	N/A	−0.04	N/A	N/A
22:15	62.30	N/A	36.91	92.84	16.36	55.22
22:30	72.84	N/A	57.42	94.04	8.60	88.63
22:45	32.11	N/A	89.71	89.36	96.78	96.30
23:00	89.05	55.13	97.56	96.33	90.15	96.47
23:15	96.85	27.73	96.80	86.09	96.72	97.21
23:30	98.56	95.00	92.83	86.96	95.76	97.66
23:45	98.02	28.29	95.61	85.92	88.17	98.46
00:00	97.01	59.58	94.99	91.52	97.00	95.20
00:15	91.70	58.02	93.41	95.43	97.55	96.70
00:30	93.74	79.82	90.44	95.65	97.67	97.67
00:45	93.40	83.90	92.87	96.93	96.44	97.38
01:00	88.40	91.27	93.36	95.65	95.89	92.32
01:15	89.62	85.12	95.94	93.98	96.05	94.48
01:30	92.85	94.35	94.70	97.38	95.87	98.63
01:45	92.68	91.68	94.20	91.56	97.26	97.45
02:00	91.08	77.30	90.55	92.15	97.90	97.14
02:15	88.12	73.19	91.96	77.12	96.92	96.51
02:30	93.72	44.65	65.34	81.52	96.92	93.91
02:45	93.95	40.81	42.71	94.33	89.03	88.26
03:00	88.20	28.48	30.05	69.51	80.80	91.45
03:15	36.17	26.11	27.21	73.94	73.45	90.36
03:30	6.30	32.76	N/A	69.45	74.95	79.73
03:45	−0.19	72.15	N/A	45.27	84.11	67.99
04:00	N/A	N/A	51.98	84.22	64.44	−0.10
04:15	N/A	N/A	20.27	82.90	75.16	0.47
04:30	N/A	N/A	N/A	N/A	60.42	77.41
04:45	N/A	N/A	N/A	N/A	N/A	82.71
05:00	N/A	N/A	N/A	83.88	N/A	68.14

Table 5.7 - Correlation between phase and ROTI probability maps for different times of the 6 consecutive nights (comparison C).

Time (UT)	Nights of March, 2023					
	08	09	10	11	12	13
20:45	N/A	N/A	N/A	N/A	79.90	N/A
21:00	N/A	N/A	N/A	N/A	68.21	N/A
21:15	N/A	N/A	N/A	N/A	79.14	N/A
21:30	N/A	N/A	N/A	N/A	84.06	N/A
21:45	N/A	N/A	N/A	N/A	84.62	N/A
22:00	N/A	N/A	N/A	100.00	84.93	N/A
22:15	49.37	N/A	53.06	95.30	59.31	37.62
22:30	60.04	N/A	35.87	88.67	74.36	88.78
22:45	N/A	N/A	92.60	84.92	94.39	97.87
23:00	84.59	55.13	97.07	96.49	94.11	96.16
23:15	96.15	13.49	86.38	89.53	87.43	97.31
23:30	94.14	91.76	93.62	95.05	96.93	95.75
23:45	96.18	4.30	82.64	95.82	90.69	98.88
00:00	94.41	54.02	74.72	96.04	96.51	94.45
00:15	88.31	50.85	87.88	96.27	94.88	96.36
00:30	92.41	88.87	89.44	91.55	95.65	94.21
00:45	89.05	81.79	88.42	91.66	92.50	92.23
01:00	90.82	81.54	82.90	90.28	95.04	85.82
01:15	90.61	89.83	85.93	81.03	94.96	90.60
01:30	91.98	84.14	87.38	78.52	97.71	97.04
01:45	89.93	60.08	87.78	61.18	95.76	97.04
02:00	90.10	58.29	94.29	64.84	97.29	93.06
02:15	85.81	60.89	87.17	77.86	96.86	97.93
02:30	91.49	61.67	85.92	78.87	94.57	91.82
02:45	83.18	59.17	40.49	89.37	88.92	95.50
03:00	84.76	48.15	26.15	65.77	94.23	91.60
03:15	1.63	40.20	18.97	61.85	86.12	94.91
03:30	50.83	24.83	N/A	73.40	73.76	92.42
03:45	83.27	61.83	N/A	56.52	81.36	46.21
04:00	N/A	N/A	72.48	88.92	74.94	N/A
04:15	N/A	N/A	N/A	58.26	68.59	N/A
04:30	N/A	N/A	N/A	N/A	77.50	39.43
04:45	N/A	N/A	N/A	N/A	N/A	81.66
05:00	N/A	N/A	N/A	N/A	N/A	63.84

Table 5.7 shows that, considering the interval between 22 UT and 03 UT, when scintillation events are more likely to occur, correlations are higher, as it would be expected. The overall correlation coefficient for all nights (22 UT to 03 UT) is 90.95 %, while the overall correlation coefficients for each night, from 08 to 13 of March 2023, are, respectively: 90.88 %, 73.74 %, 86.38 %, 86.99 %, 94.34 %, and 94.20 %.

5.5 Example of a probability map sequence

This section shows a sequence of probability maps of each type for the night from March 10th to 11th in 2023: amplitude probability (Figure 5.2), phase probability (Figure 5.3) and ROTI probability (Figure 5.4). These sequences of maps can be compared in Figure 5.5, which shows the amplitude probability sequence (1st row of maps), the phase probability sequence (2nd row of maps) and the ROTI probability sequence (3rd row of maps). The above sequence of maps were generated by the proposed approach employing INCT data.

Finally, as shown in Figure 5.6, the ROTI probability map sequence can be generated using (i) only INCT data (1st row of maps), (ii) only RBMC data (2nd row of maps) and (iii) data from both networks (3rd row of maps). It can be observed that as more GNSS stations are employed, more details can be seen in each map of the sequence.

Figure 5.2 - Hourly sequence of amplitude probability maps generated by the proposed approach employing INCT data, which shows the evolution of the ionospheric irregularities.

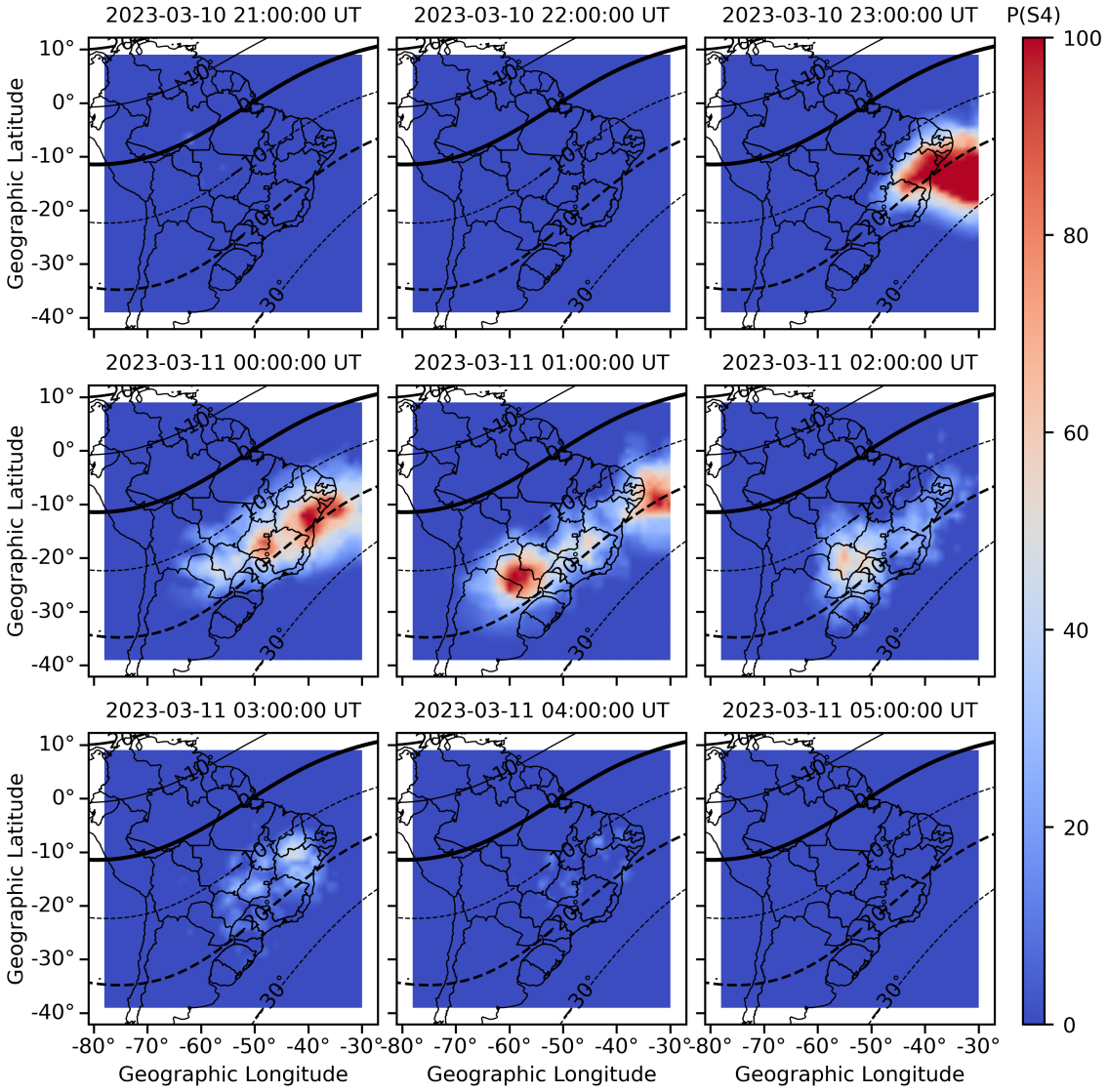

Figure 5.3 - Hourly sequence of phase probability maps generated by the proposed approach employing INCT data, which shows the evolution of the ionospheric irregularities.

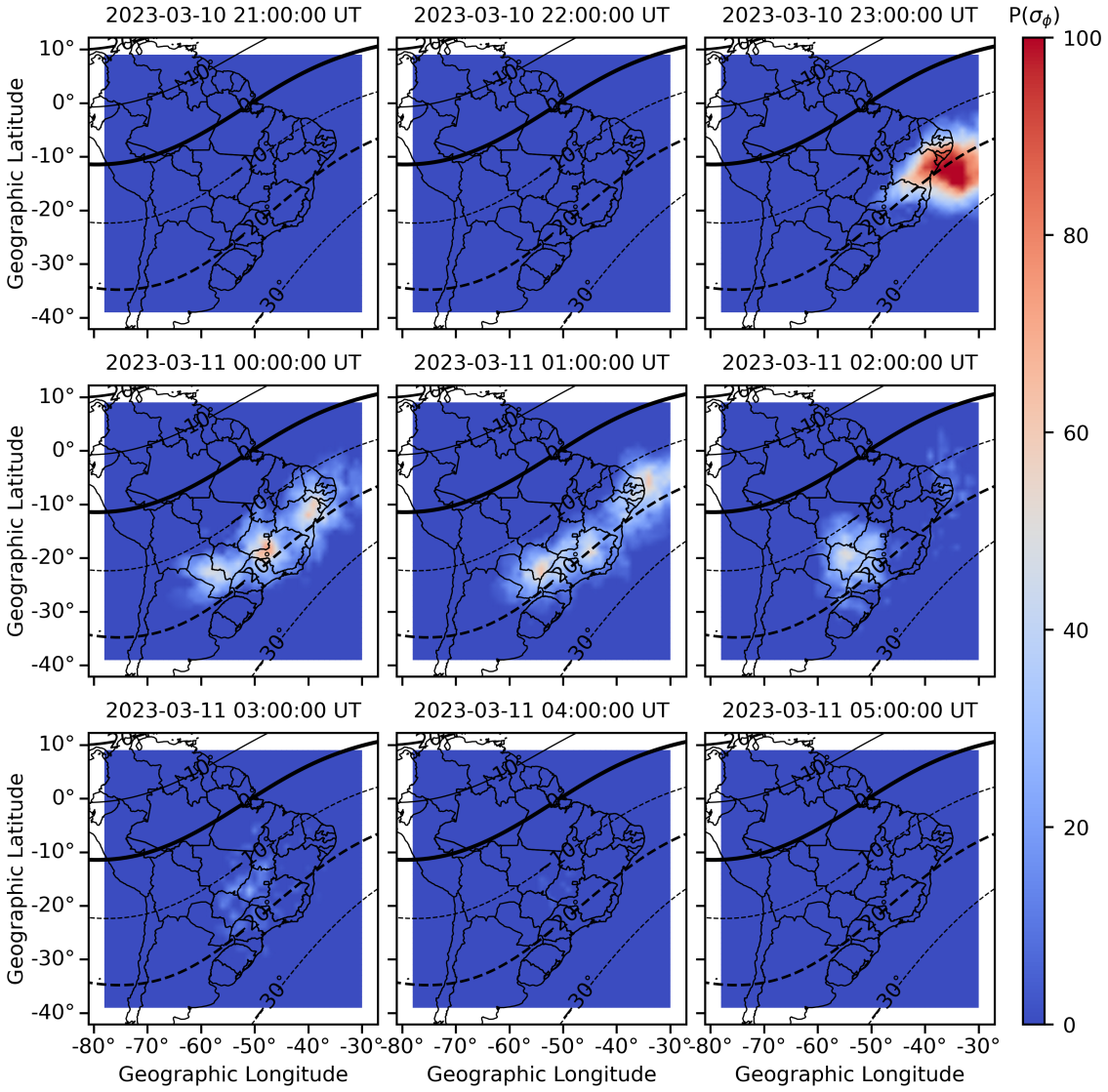

Figure 5.4 - Hourly sequence of ROTI probability maps generated by the proposed approach employing INCT data, which shows the evolution of the ionospheric irregularities.

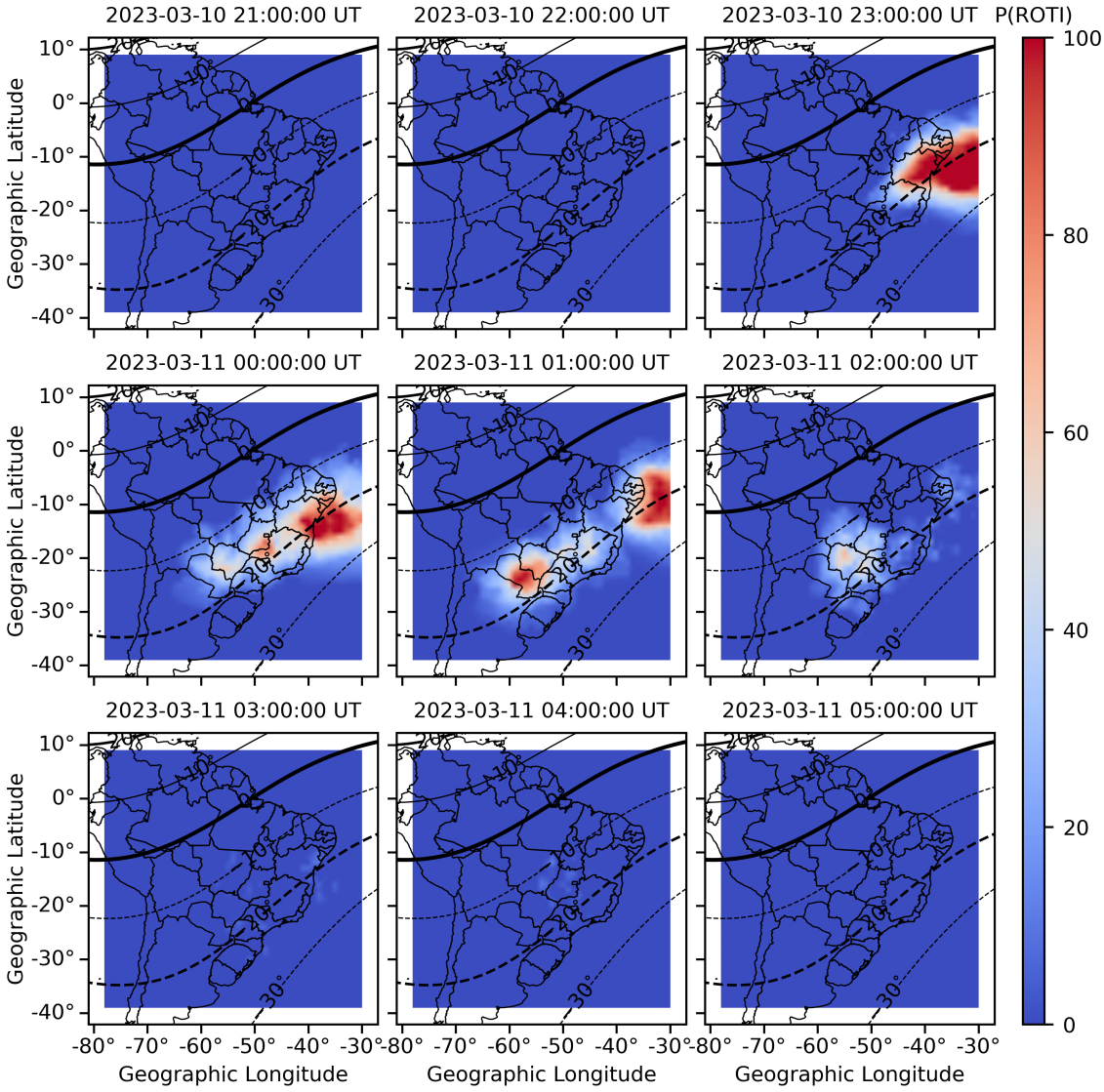

Figure 5.5 - Comparison of amplitude (1st row of maps), phase (2nd row of maps) and ROTI (3rd row of maps) probability maps generated by the proposed approach using INCT data.

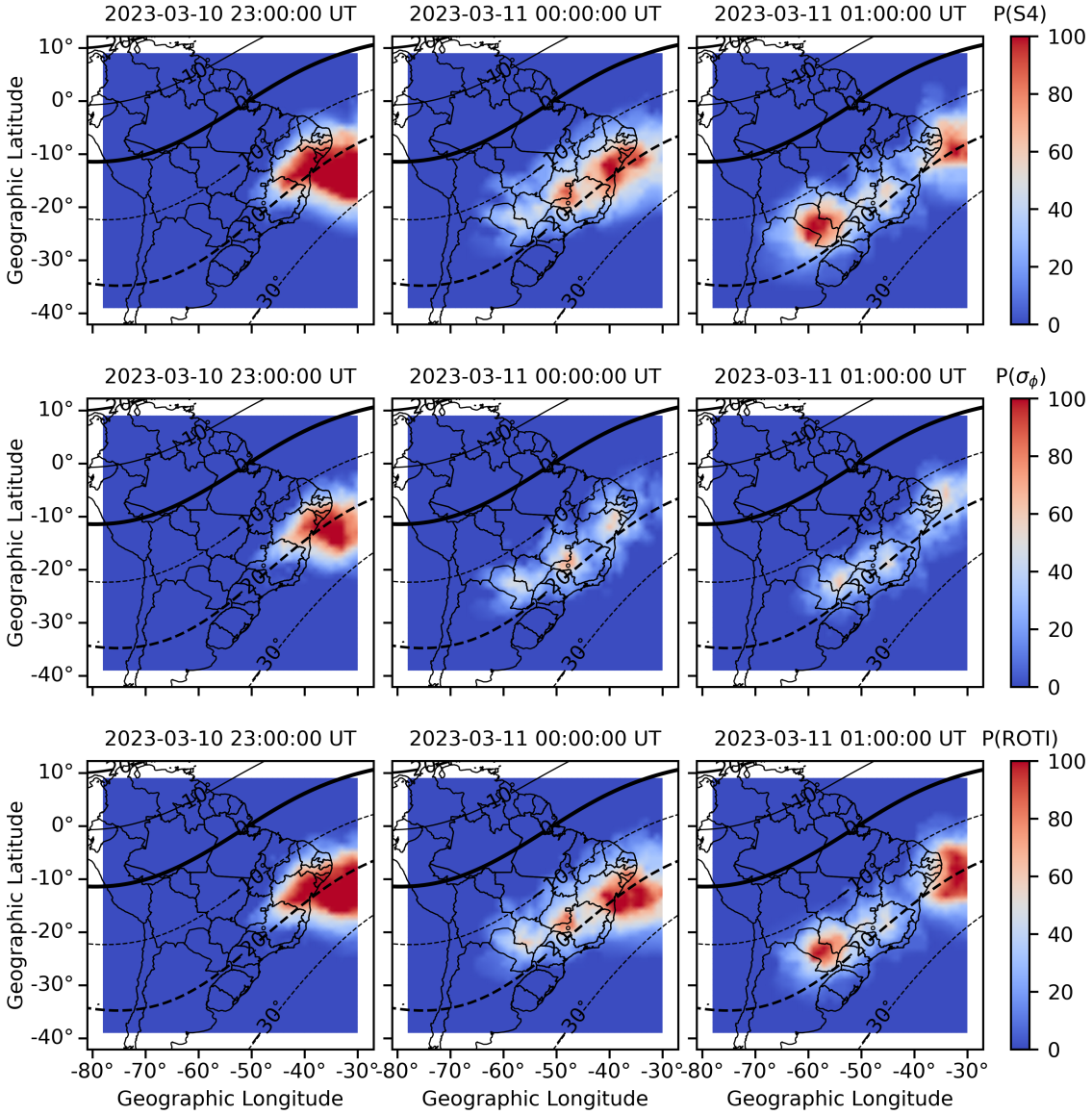

Figure 5.6 - Comparison between ROTI probability maps generated by the proposed approach, using only INCT data (1st row of maps), only RBMC data (2nd row of maps) and using data from both networks (3rd row of maps).

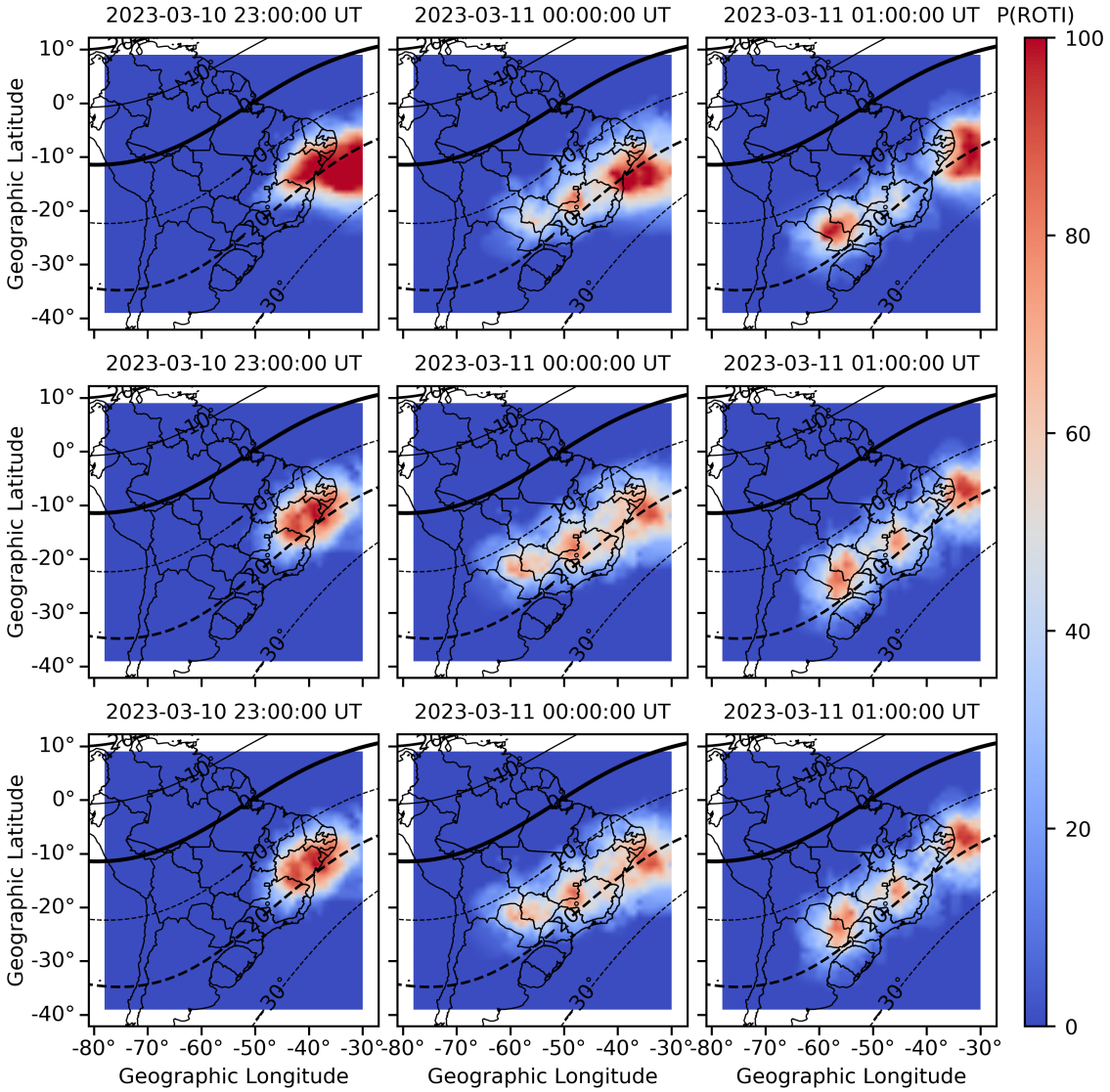

5.6 Discussion and conclusions

The innovative scintillation probability maps were evaluated using an extensive amount of real scintillation data of the three ionospheric indexes (amplitude scintillation, phase scintillation and ROTI). The probability maps derived from the corresponding maps of these indexes were evaluated using a set of GNSS stations in order to check if these maps were accurate concerning the monitoring of moderate-strong

scintillation. According to the employed metrics, the probability maps presented low errors, i.e. in most cases showed for the GNSS station location moderate-strong scintillation when actually the station was undergoing such level of scintillation. Consequently, the related correlation was high.

The results presented in this chapter demonstrate the potential of the probability maps as a real warning tool for moderate-strong scintillation in GNSS applications, and also for remote sensing and telecommunication satellites in general, which employ electromagnetic bands that can be affected by scintillation.

Further works devise a specific preprocessing for ionospheric index missing data due to station technical issues or loss-of-lock that will render better probability maps. Preliminary evaluations have already demonstrated that real time generation of scintillation probability maps for operational purposes is feasible using standard computational and network resources.

6 IONOSPHERIC SCINTILLATION PREDICTION

As already mentioned and detailed in Section 1.1, research intended for low latitude amplitude scintillation prediction and related research using data-oriented models was started in Brazil during the last decade (LIMA et al., 2014; LIMA et al., 2015; REZENDE, 2009; REZENDE et al., 2010; VANI, 2018). Besides these works, there seems to be a sole work concerning low latitude amplitude scintillation prediction (ZHAO et al., 2021), which proposed a data-oriented model using the Gradient Boosting algorithm, employing S4 data for the 2012-2020 years and also the virtual height of the ionospheric F layer, yielding a single prediction per night at a given station. A more recent work also proposed scintillation prediction with data-oriented models for low magnetic latitudes (São José dos Campos, Brazil), using historical data of ionospheric scintillation and additional/exogenous ionospheric, geomagnetic and solar-activity data for the period 2011-2018 of a previous solar cycle (DOS SANTOS, 2022; DOS SANTOS et al., 2022). Two Gradient Boosting Tree algorithms, and a convolutional neural network were evaluated. However, neither of these works presented prediction results with prediction performance suitable for operational purposes.

In this thesis, time series of amplitude scintillation maps or of the corresponding probability maps, were generated for the prediction of the scintillation. In these maps, the fraction of area corresponding to moderate-strong scintillation is taken as a predictive variable for scintillation prediction using a machine learning algorithm. The same prediction approach may be further extended for phase scintillation or ROTI or the corresponding probability maps. In this chapter, for the sake of simplicity, the area undergoing moderate-strong scintillation is referred simply by area in the amplitude scintillation maps. The same applies for the area related to moderate-strong class in the probability maps.

6.1 Proposed methodology for scintillation prediction

The amplitude scintillation maps or the corresponding probability maps were generated for intervals of time within each night, providing a two-dimensional time series of the ionospheric scintillation. The time series for each night allows us to follow the evolution of the scintillation over the Brazilian territory.

Assuming that the sequence of scintillation maps for each night has a dependence due to the temporal order between consecutive maps, the time is added as a predictive variable, providing additional information about the evolution of the ionospheric

scintillation along each night.

The proposed prediction approach considered 125 consecutive nights during the Solar Maximum of 2014, with a total of 35 scintillation maps per night, each one integrating 30 minutes of data. The first map is generated for 20:30 UT and the last map is generated at 05 UT. The temporal resolution of 30 minutes and the sliding window overlap of 15 minutes were chosen to obtain a smooth transition between consecutive maps.

The objective of the proposed prediction is to generate a moderate to strong ionospheric scintillation warning, answering the following questions:

1. How large is the area of Brazilian territory that could be affected by strong ionospheric scintillation in the next hour?

2. Considering a specific region of Brazil, what is the probability of it being affected by moderate-strong ionospheric scintillation?

In order to answer the first question, the two-dimensional time series of 35 amplitude scintillation maps for each night can be reduced to a one-dimensional time series given by the percentage of total area of moderate-strong amplitude scintillation of each scintillation map (values above 0.5), as exemplified in Figure 6.1. The same reduction of dimensionality is done for the corresponding moderate-strong probability maps, resulting in a one-dimensional time series related to the percentage of total area of the probability of moderate-strong scintillation above zero, as seen in Figure 6.2.

In order to answer the second question, the original area covering Brazil can be subdivided into quadrants successively, i.e. into 4 quadrants, and then each one of these also subdivided into 4 sub-quadrants and so on. Therefore, it would be possible to have a better identification of the area that will undergo scintillation. Here, the considered area was divided into 4 quadrants, and thus the time series of 35 amplitude scintillation maps for each night allows to derive 4 time series given by the percentage of area with moderate-strong scintillation (values above 0.5) for each quadrant, as exemplified in Figure 6.3. The same dimensionality reduction is done for the corresponding moderate-strong probability maps, resulting in 4 time series given by the percentage of area with the probability of moderate-strong scintillation above zero for each quadrant, as seen in Figure 6.4.

Figure 6.1 - Examples of amplitude scintillation maps (left panel), and the corresponding area (right panel) that presents moderate-strong scintillation, i.e. S4 values above 0.5.

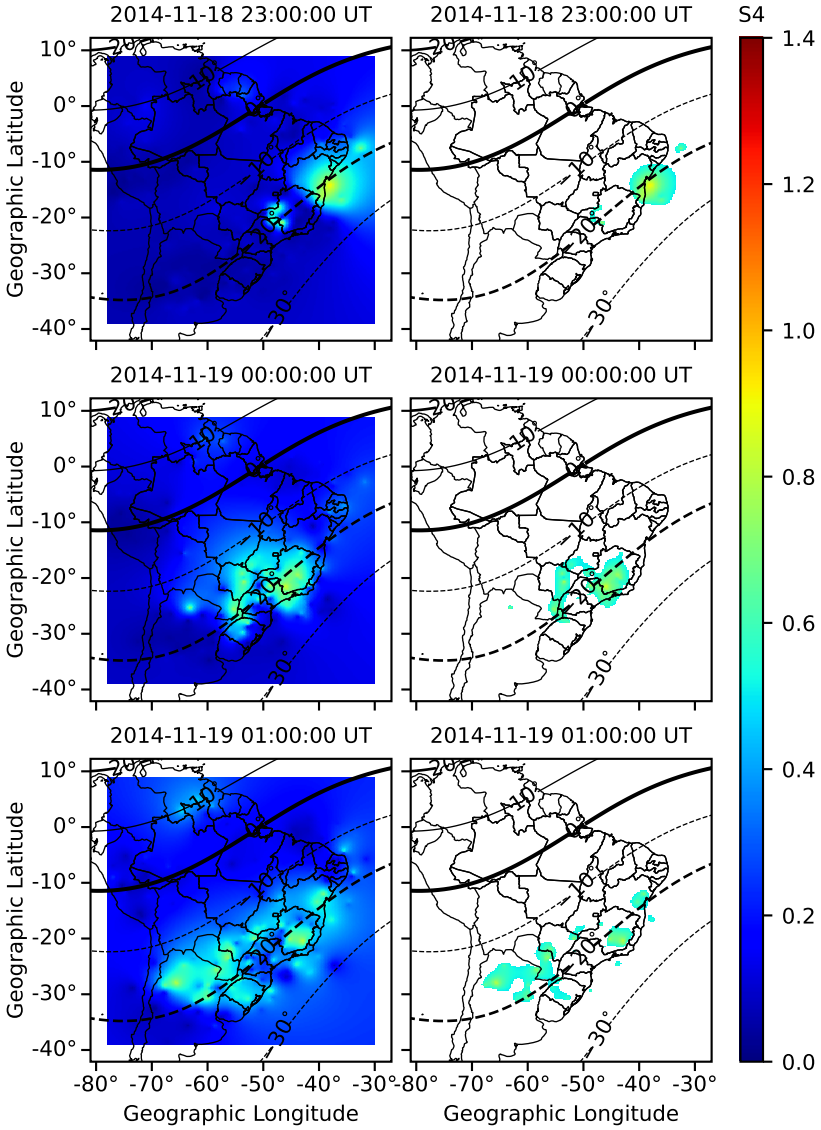

The prediction of the time series derived from the scintillation maps, and the corresponding probability maps, can be modeled as a supervised learning problem, allowing the use of standard linear or nonlinear machine learning algorithms.

In supervised learning, an algorithm learns from a mapping function that has training set of input/predictive variables (X) samples and the corresponding output/predicted variable (y) samples, as defined in Equation 6.1:

Figure 6.2 - Examples of moderate-strong amplitude probability maps (left panel), and the corresponding area (right panel) that presents probabilities above zero.

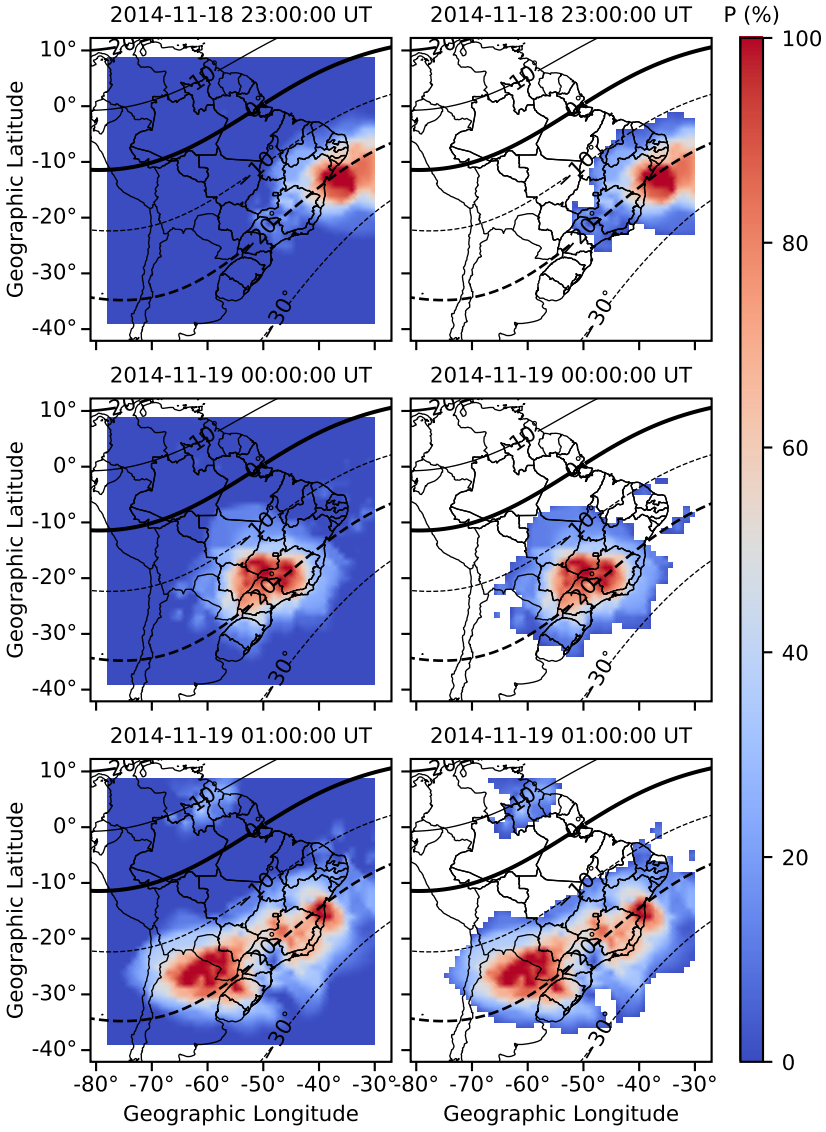

$$y = f(X) \tag{6.1}$$

The prediction of total percentage area and quadrant percentage area time series represent a regression problem, since the output variable (y) has a real value, in this case the area percentage.

As an example, considering the covered sequence of nights, a time series of the

Figure 6.3 - Examples of amplitude scintillation maps (left panel), and the corresponding 4 quadrants showing moderate-strong scintillation, i.e. S4 above 0.5.

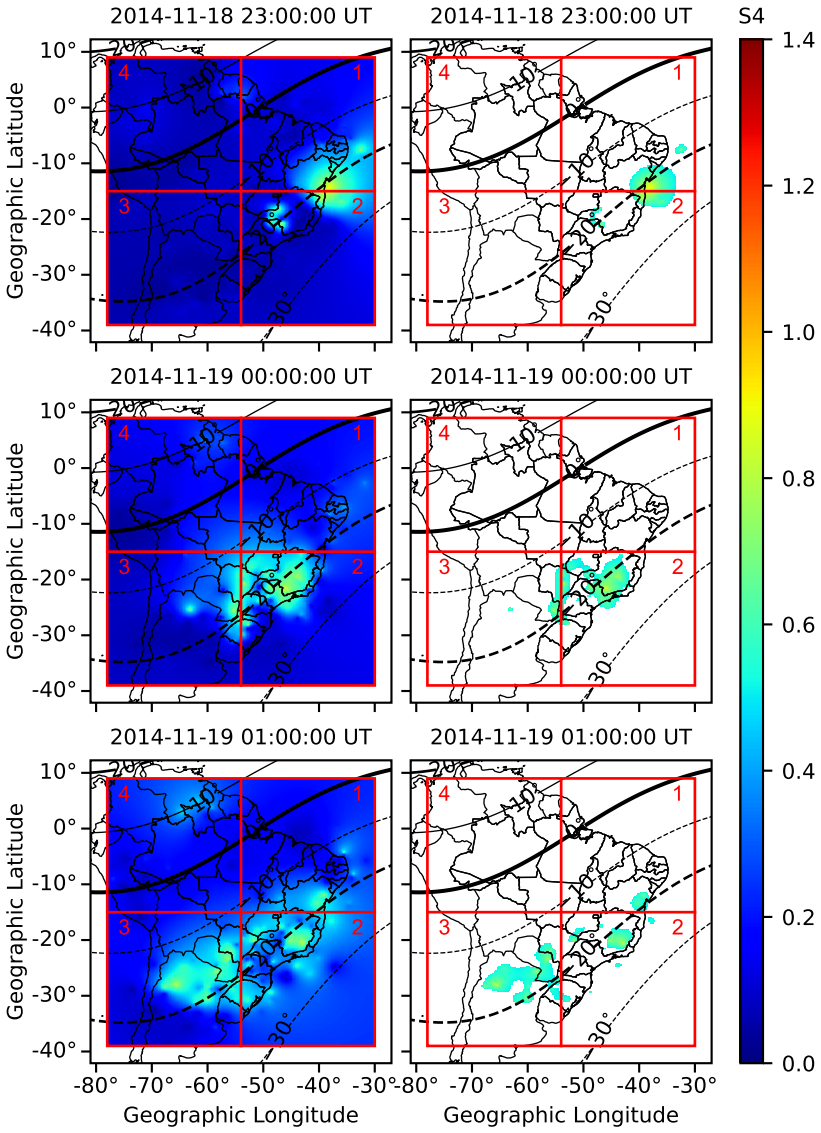

percentage of total area of the probability of moderate-strong scintillation can be extracted for a given night. The corresponding dataset has a time column (20:30, 20:45, 21:00, ..., 04:30, 04:45, 05:00), and an area column (0, 3.2, 20.1, ..., 30.5, 10, 0). This time series dataset needs to be reorganized for supervised learning, for instance, this may be achieved using the area of the previous time step as input (X) and the corresponding area of the next time step as the output (y), which expresses a temporal dependency.

Figure 6.4 - Examples of moderate-strong amplitude probability maps (left panel), and the corresponding 4 quadrants (right panel), showing probabilities above zero.

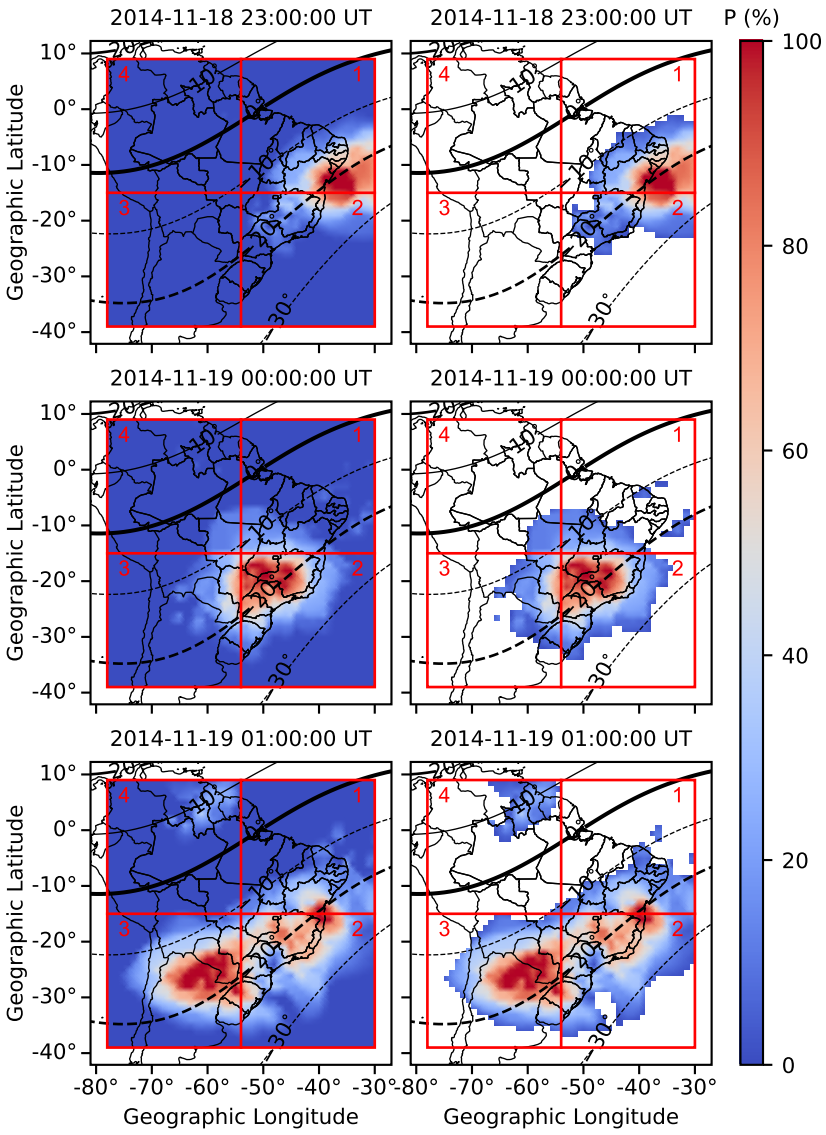

In addition, more input variables are used, as the mean area value of the previous 3 nights. The prediction for time (t) employs the preceding variables in 15-minute intervals of the same night. Thus prediction of the area for time (t) uses as predictive variables the area values of the 3 preceding times, i.e. the $t-3$, $t-2$, and $t-1$ area values. Besides that, the prediction is enhanced adding the mean of the exogenous variable F10.7 (solar flux) of the previous 3 nights as a further predictive variable.

In the proposed approach the machine learning algorithm chosen is an ensemble of

parallel decision trees, the eXtreme Gradient Boosting (XGBoost). However, instead of deriving a prediction model for all the times of all nights, a set of 32 prediction models are derived, one for each time of the night, based on the times that define the 15-minute intervals. The number of models (32) is defined by the interval of 21:15-05:00 UT of each night, and despite the 35 available values, it is only possible to derive 32 models, since each model needs the area values for the previous three discrete times.

This proposed approach for scintillation prediction is also intended for operational purposes in the real-time system presented in the next chapter (Chapter 7). The proposed set of 32 models for area prediction employs known data for the prediction with 15-minute antecedence. However, for prediction antecedence above 15 minutes, which is intended as a future work, the set of models will employ autoregression, i.e. it will employ its own predictions. In addition, the prediction would be enhanced by the use of updated scintillation data and the corresponding update values of area in place of the corresponding area values formerly available, either derived from historical scintillation data or from previous area predictions.

6.2 Data description

The proposed scintillation prediction approach was applied in a set of 4,375 scintillation amplitude maps generated using the GPR(VQI), and the respective 4,375 probability maps. Scintillation data was acquired for 125 consecutive nights from 28th of August to 30th of December, 2014, during the Solar maximum of the previous Solar Cycle. Such data was acquired for a 9-hour interval per night (from 20:00 LT to 5:00 LT), which mostly presented moderate and strong scintillation events. Each 9-hour interval is divided into 35 consecutive intervals, which allows to derive 35 scintillation maps per night. Each map integrates 30 minutes of data, using 29-minute a priori data and a sliding window of 15 minutes. Therefore, temporal resolution is 30 min and there is a 15-minute overlap between consecutive maps, providing a smooth transition between consecutive maps.

The GNSS amplitude scintillation data was obtained from two ionospheric monitoring networks, LISN, which covers most of South America, and INCT stations, covering only the Brazilian territory. LISN receivers are only compatible with GPS and SBAS satellites, while INCT receivers are multi-constellation. These networks provided a total of 46 ionospheric monitoring stations, with the corresponding locations shown in Figure 6.5. Not all the 46 stations of these networks have been continuously operational, with the total number of available stations ranging between

7 and 42 per night. The present study employs all available GNSS constellations, according to the monitoring network, for the considered time interval to produce the scintillation maps, except for SBAS satellites.

Figure 6.5 - Geographic location of the 46 GNSS stations of the LISN and INCT networks that provided scintillation data for the proposed scintillation prediction.

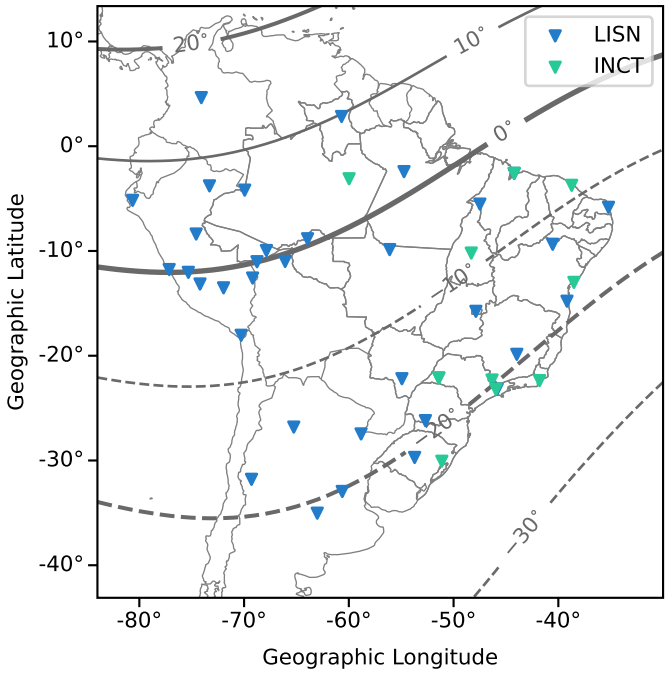

Table 6.1 presents the geographic locations and the magnetic dip latitudes for the 12 INCT monitoring stations, while Table 6.2 presents the same information for the 34 LISN monitoring stations. Since the intervals of time selected for this work are between August 2014 and December 2014, the magnetic dip latitude curves in Figure 6.5 and the values presented in these tables were derived using the year 2014 as reference and were calculated using the IGRF 13 model (ALKEN et al., 2021). Since the format of the data provided by the two monitoring networks is different, a unified data format was adopted, as shown in Section 3.2.

Figure 6.6 presents, for the 125 consecutive nights, the distribution of the S4 values classified into three severity classes using the following thresholds: null [0.00-0.15], weak-moderate (0.15-0.50], moderate-strong (0.50-1.4). The S4 values above 1.4 were considered outliers, being rounded to that upper threshold. For each night the figure shows the scintillation distribution, the corresponding values of the planetary Kp

geomagnetic index and the adjusted F10.7 index (solar flux at the 10.7 cm wavelength).

Table 6.1 - Coordinates of the INCT GNSS ionospheric monitoring network stations.

Station	**City**	**Geographic**		**Magnetic**
		Latitude	**Longitude**	**Dip Latitude**
SLMA	São Luís	−2.5935	−44.2123	−4.6808
MAN3	Manaus	−3.1102	−59.9749	4.2379
FRTZ	Fortaleza	−3.7362	−38.7248	−8.7233
PALM	Palmas	−10.1996	−48.3113	−8.5045
UFBA	Salvador	−12.9998	−38.5107	−16.9033
PRU1	Presidente Prudente	−22.1200	−51.4087	−16.6408
PRU2	Presidente Prudente	−22.1220	−51.4071	−16.6408
INCO	Inconfidentes	−22.3185	−46.3281	−19.5684
MAC2	Macaé	−22.3768	−41.7914	−22.0497
SJCE	São José dos Campos	−23.2075	−45.8597	−20.2967
SJCU	São José dos Campos	−23.2106	−45.9566	−20.2967
POAL	Porto Alegre	−30.0739	−51.1197	−22.2423

A dimensionality reduction is applied for the set of 4,375 amplitude scintillation maps, and the corresponding moderate-strong probability maps. Each amplitude scintillation map (193×193 grid points) is reduced to a single value corresponding to the percentage of total area of moderate-strong scintillation, i.e. S4 values above 0.5. The same reduction is made for the moderate-strong probability maps (49×49 grid points), considering the percentage of total area of moderate-strong probability above zero. In addition, each amplitude scintillation map (193×193 grid points) is further divided into four quadrants, each one with a percentage of area with moderate-strong scintillation. Each moderate-strong probability map (49×49 grid points) is also divided into four quadrants, each one with a percentage of area with moderate-strong probability above zero.

6.3 Evaluation of the prediction performance

The dataset comprehends 125 night intervals, from 08/28/2014 to 12/30/2014. The first 65 night intervals, from 08/28/2014 to 10/31/2014, were used only for the

Table 6.2 - Coordinates of the LISN GNSS ionospheric monitoring network stations.

Station	**City**	**Geographic**		**Magnetic**
		Latitude	**Longitude**	**Dip Latitude**
LBO_	Bogota	4.6378	−74.0823	15.5882
LBOA	Boa Vista	2.8338	−60.6946	10.0516
LSTM	Santarem	−2.4283	−54.7314	2.6909
LSLZ	Sao Luiz	−2.5934	−44.2123	−4.6808
LIQ_	Iquitos	−3.7860	−73.3040	7.2002
LLE_	Leticia	−4.1937	−69.9407	6.6783
LPIU	Piura	−5.1699	−80.6393	6.5588
LIMP	Imperatriz	−5.5280	−47.4880	−5.5614
LNTA	Natal	−5.8362	−35.2077	−13.0839
LPUC	Pucallpa	−8.3839	−74.5737	3.7054
LPVH	Porto Velho	−8.8371	−63.9399	0.4650
LPLN	Petrolina	−9.3622	−40.5395	−12.0842
LAFL	Alta Floresta	−9.8705	−56.1040	−3.9232
LRBR	Rio Branco	−9.9577	−67.8690	0.7651
LRIB	Riberalta	−10.9997	−66.0807	−0.6801
LCOB	Cobija	−11.0266	−68.7677	0.0900
LANC	Ancon	−11.7766	−77.1501	0.0400
LHYO	Huancayo	−12.0424	−75.3214	−0.0150
LPMO	Puerto Maldonado	−12.5859	−69.1868	−1.7216
LAYA	Ayacucho	−13.1537	−74.2061	−1.0103
LCUZ	Cuzco	−13.5204	−71.9593	−2.1279
LIOS	Ilheus	−14.7966	−39.1724	−18.5847
LBSB	Brasilia	−15.7644	−47.8692	−13.6291
LTAC	Tacna	−18.0507	−70.2773	−6.0252
LBHT	Belo Horizonte	−19.8686	−43.9619	−19.3086
LDOU	Dourados	−22.1960	−54.9317	−14.5240
LSJK	Sao Jose	−23.2076	−45.8597	−20.2967
LPBR	Pato Branco	−26.1977	−52.6894	−18.5325
LTCA	Tucuman	−26.8140	−65.2557	−14.6371
LCOR	Corrientes	−27.4671	−58.8310	−16.5537
LSTA	Santa Maria	−29.7126	−53.7173	−20.7897
LLEO	Casleo (El leoncito)	−31.8001	−69.2927	−17.7132
LSTF	Rosario	−32.9593	−60.6284	−20.0728
LVLG	Villegas	−35.0326	−63.0136	−20.8310

Figure 6.6 - Distribution of the IPP samples for each of the 125 consecutive nights according to the three-class scintillation severity classification.

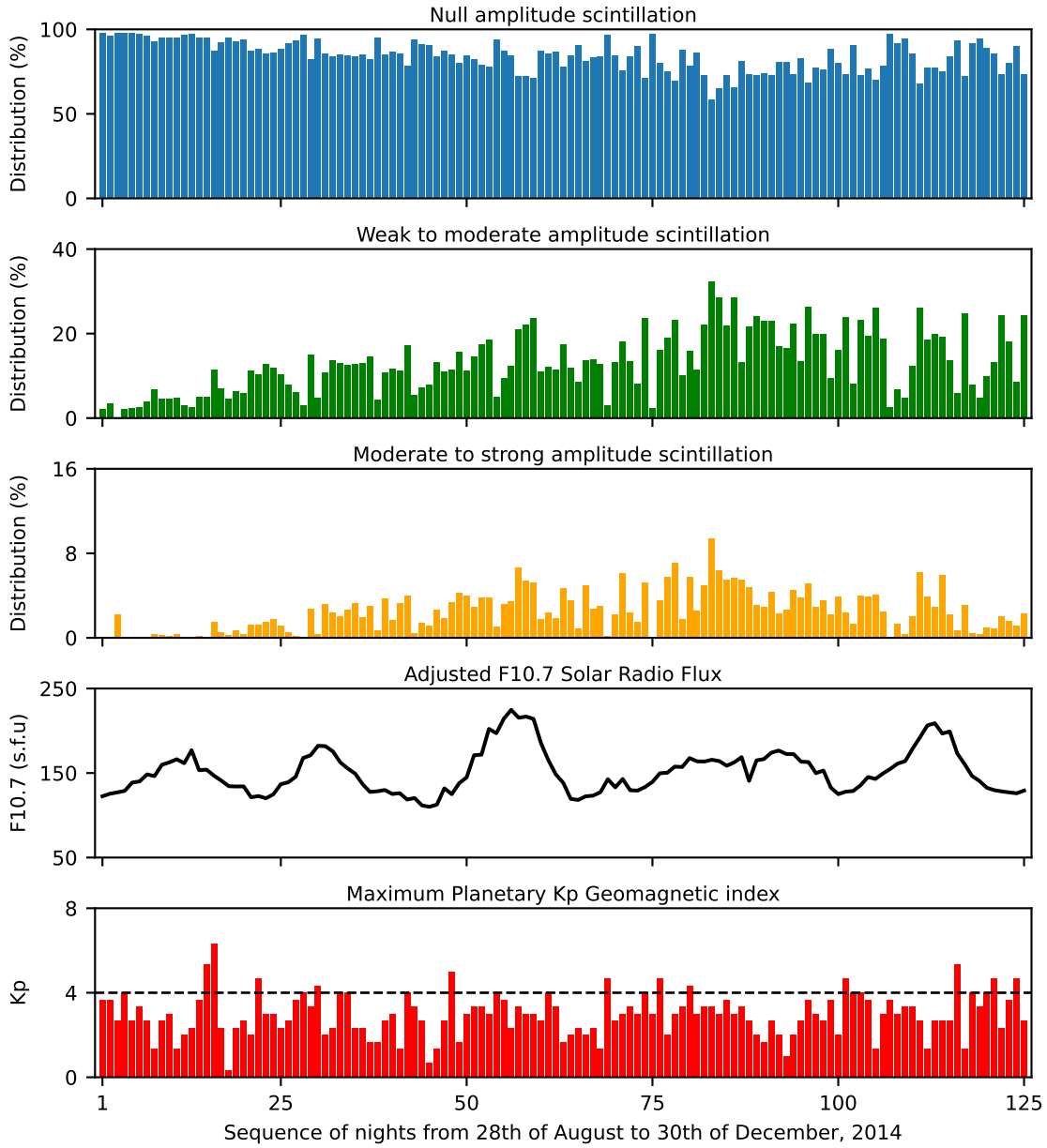

training of the set of 32 models, while the following night intervals were used for both training and the test of the set of models, starting with the 11/01/2014 night interval until 12/30/2014. In the case of the subsequent nights after 10/31/2014, the training of the models also employs data from the preceding nights. In this initial implementation, the training process does not use autoregression, i.e. does not include the previous predictions in the training data, but instead the real data

of preceding night for each time step.

As mentioned before in this chapter, there is a model per 15-minute time step of the area time series. The data employed for each model includes the previous 3 time steps, and thus, for a given night interval, the first time step to be predicted is for 21:15 UT, the next time step 21:30 UT, which uses the real/observed data of the previous 21:15 time step, 21:15 UT, and so on.

A walk-forward validation scheme was used to evaluate the prediction of the set of 32 models, which allows the update of the set of models each time step new data is available from real data acquisition from different nights, but always for the same considered time step. This is a time-series cross-validation scheme used to assess the performance of predictive models, and suitable for data that is ordered in time. Data is usually split into training, validation, and test sets, but here a different data division is employed due to the scarce amount of data related to moderate-strong scintillation occurrences. Therefore, as new data becomes available for further night intervals, such data is included in the training set, with no validation set (despite the XGBoost implementation including a validation phase). Prediction is then performed using all the data from the preceding nights for a given time step.

A baseline model was chosen in order to compare the proposed predictions using XGBoost, a simple persistence model, which uses the area at the current time step (t) to predict the next area at the next time step ($t+1$). The choice of the persistence model is reasonable, since the prediction time is only 15 minutes.

Prediction results are shown in Table 6.3 for predictions using the total area time series or the time series for the 4 quadrants, both derived from the amplitude scintillation maps. The RMSE results show that the set of XGBoost models presented a considerable reduction in comparison to the Persistence model. The correlations of the real area time series and the predicted area time series were much better for the set of XGBoost models, particularly considering the total area or the 2nd quadrant, which covers the Brazilian Southeast and the related Atlantic coast.

Prediction results are shown in Table 6.4 for predictions using the total area time series or the time series for the 4 quadrants, both derived from the probability maps. Similarly as the results shown in the former table, the RMSE results show that the set of XGBoost models also presented a considerable reduction in comparison to the Persistence model. The correlations of the real area time series and the predicted area time series were much better for the set of XGBoost models (above 0.90 in

Table 6.3 - Prediction performance (RMSE and correlation) of the proposed set of XGBoost models using the area time series derived from the amplitude scintillation maps, compared to the corresponding performance of the persistence model.

Time series	Persistence Model		Set of XGBoost Models	
	RMSE	**CORR**	**RMSE**	**CORR**
Total area	0.0143	0.5103	0.0076	0.8592
Quadrant-1 area	0.0203	0.3460	0.0121	0.7374
Quadrant-2 area	0.0307	0.4905	0.0150	0.8749
Quadrant-3 area	0.0195	0.4870	0.0127	0.7551
Quadrant-4 area	0.0122	0.2692	0.0080	0.6120

all cases), mainly considering the total area or the 2nd quadrant, which covers the Brazilian Southeast and the related Atlantic coast.

Table 6.4 - Prediction performance (RMSE and correlation) of the proposed set of XGBoost models using the area time series derived from the probability scintillation maps, compared to the corresponding performance of the persistence model.

Time series	Persistence Model		Set of XGBoost Models	
	RMSE	**CORR**	**RMSE**	**CORR**
Total area	0.1204	0.6456	0.0468	0.9471
Quadrant-1 area	0.1626	0.6130	0.0743	0.9198
Quadrant-2 area	0.1420	0.6425	0.0525	0.9509
Quadrant-3 area	0.1415	0.6070	0.0692	0.9022
Quadrant-4 area	0.1741	0.5373	0.0863	0.8834

6.4 Discussions and conclusions

The proposed approach for scintillation prediction presented higher correlations to observed/real values and lower errors in comparison to the persistence mode. Time series of amplitude scintillation maps and the corresponding probability maps were employed to derive the related time series of the areas with moderate-strong scintilla-

tion or the times series of the areas with probability of moderate-strong scintillation above zero, respectively. Prediction performance using the time series of the areas of the latter maps was better, with correlations to observed/real values above 0.90. Therefore, the proposed prediction approach seems to have potential to be further improved in order to be used operationally.

In future work related to scintillation prediction, time series of eventual different parameters of maps of different ionospheric indexes, or of the corresponding probability maps, may be chosen instead of the time series of the area parameter derived from amplitude scintillation maps, shown here. Similarly to the prediction approach presented here, prediction may be tried for smaller quadrants, antecedence of more hours of the same night, and using other additional/exogenous data, like for instance digisonde data.

Furthermore, different machine learning algorithms can be tested, including the related hyperparameter optimization, in order to choose the one with better prediction performance.

7 REAL-TIME SYSTEM FOR SCINTILLATION MONITORING

A real-time system for the generation and online dissemination of scintillation index maps covering the Brazilian territory was entirely developed in the scope of this thesis. A prototype of such a system, only for amplitude scintillation maps, was already proposed in Martinon et al. (2024), but was extended and tested for the phase scintillation maps here. The system included all the processing steps to generate the maps using the approach described in Chapter 4, which uses innovative preprocessing and interpolation methods. In addition, the approach has low computational cost and is compatible with real-time demands.

Scintillation data is acquired from two networks of multi-constellation GNSS monitoring stations, which are the LISN network and the INCT network. Only the INCT network provides the σ_ϕ scintillation index. Section 2.2 provides more detailed information about the Brazilian GNSS networks for ionospheric monitoring.

A single real-time server, a standard personal computer (PC), centralizes the data reception from the GNSS stations, performs all the required data processing and provides a web service for the online dissemination of the maps. Data processing at the real-time server can be divided into three steps: remote data acquisition, interpolation, and image rendering, while local data acquisition is performed locally at the GNSS stations.

The key concept of the system is to establish a pipeline for performing these tasks asynchronously and without any loss of data in the real-time server. The challenges that must be overcome to have real-time capability are related to the tasks described above: (i) to configure two types of GNSS monitoring stations to send scintillation index data asynchronously without loss of data, and to configure a real-time server able to (ii) receive scintillation index data from GNSS stations also asynchronously without loss of data, (iii) process scintillation index data in order to generate sequences of amplitude or phase scintillation maps with 1-minute resolution, and (iv) make these maps available in a web server. As a result, the implemented system was able to acquire data from all available stations of the two monitoring networks, being robust concerning interruption of connections or different processing times of the tasks. Therefore, the implemented system was able to provide real-time scintillation maps.

An overview of the implemented system hosted in the real-time server for the generation of amplitude or phase scintillation index maps appears in Figure 7.1. The

adopted Database Management System (DBMS), described in Section 7.1, is the central module of the system, working as a data hub for the required data processing tasks/steps, which are performed by the remaining modules as consecutive stages of a pipeline. Acquisition/reception from the GNSS stations of the specific monitoring networks is implemented by the modules "INCT Data Acquisition" and "LISN Data Acquisition", detailed in Section 7.2. A validation was performed for the INCT real-time acquired scintillation amplitude or phase data using the default post-processed data, as shown in Section 7.2.1. The scintillation index preprocessing and interpolation task/step is performed by the module "Scintillation Map Generation", discussed in Section 7.3. The image rendering task/step is carried out by the module "Scintillation Map Rendering", while resulting maps and data are made available online by the "Web Server" module, also presented in Section 7.3. The proposed real-time system proved to be feasible, allowing to process incoming scintillation index data and produce scintillation maps for the Brazilian territory in less than 1-minute, thus complying to the real-time specification.

Figure 7.1 - Modules of the system implemented in the PC-based server for the real-time generation of scintillation index maps from amplitude or phase scintillation index data.

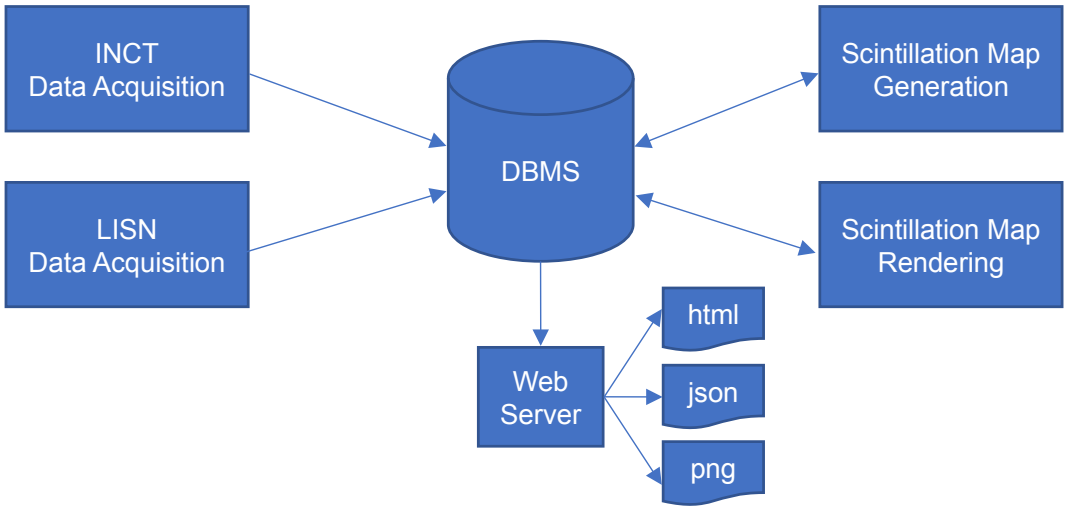

SOURCE: Martinon et al. (2024).

7.1 Data storage and processing pipeline

As already mentioned, the DBMS database is the central module of the system, acting as a hub that provides the interchange of data between the remaining modules. It allows the execution of a pipeline of processing steps in order to generate a map for each minute of received scintillation index data, similarly to an assembly line employed for automobile production.

Normally, in a traditional SQL/relational database, which employs a Structured Query Language, the retrieval of stored data is performed through periodic requests (by data pulls) made by some modules to get updated data. However, these periodic requests cannot be performed frequently nor by many client modules, since they easily degrade the performance of the DBMS. Therefore, a DBMS that sends new data in real-time whenever it is updated (by data pushes) was implemented in the real-time server, the NoSQL RethinkDB DBMS[1], providing timely exportation of data without overcharging the DBMS. Data is stored as documents, in contrast to the tuples of standard SQL/relational databases. These documents can store JSON (JavaScript Object Notation) data or binary data, and are grouped into tables.

The implemented DBMS is a database with three tables: acquired_data, scint_map and rendered_scint_map. The documents of these tables are identified by the corresponding datetime in the format "yyyy-mm-ddThh:mm:ss" composing a sequence of consecutive 1-minute intervals. There is a direct correspondence between documents of the three tables that share the same identifier. The acquired_data table stores real-time acquired data from the GNSS stations in JSON-format documents that contain data for a particular minute. Data is stored as an array of objects, with each object having a pair key-value, as depicted in Table 7.1.

The scint_map table stores the resulting matrix from the "Scintillation Map Generation" module, with each document containing the scintillation map for a particular minute, typically as a matrix of 193×193 real-valued scintillation index grid points, stored in binary format. Similarly, each document in the rendered_scint_map table contains the rendered scintillation map in raster format PNG (Portable Network Graphic) for a particular minute, also stored in binary format.

The pipeline executes some processing steps using the DBMS as a central hub, as shown in Figure 7.1. At every minute, modules "INCT Data Acquisition" and "LISN Data Acquisition" provide scintillation index data to be stored as a docu-

[1] https://rethinkdb.com/

Table 7.1 - Object pair key-value entries of a DBMS document of this work.

Key	**Value Description**
station	Monitoring station acronym.
network	LISN or INCT.
cx	Constellation acronym.
svid	Satellite identifier.
az	Azimuth (degrees).
el	Elevation (degrees).
r_lat	GNSS station latitude (degrees).
r_lon	GNSS station longitude (degrees).
s4_1	S4 index from the C/A code in the L1 band.
s4_1_sig	GPS_L1CA, GLO_L1CA, GAL_L1BC, BDS_B1I, BDS_B1C or GEO_L1.
phi60_1	phase scintillation index from the C/A code in the L1 band.
phi60_1_sig	GPS_L1CA, GLO_L1CA, GAL_L1BC, BDS_B1I, BDS_B1C or GEO_L1.

ment of the DBMS acquired_data table, which is instantly pushed to the module "Scintillation Map Generation" that performs scintillation index data preprocessing and interpolation, generating the corresponding grid point matrix, and store it back as a document of DBMS scint_map table, which in turn is instantly pushed to the module "Scintillation Map Rendering" that finally performs the image rendering step for the considered minute. Therefore, consecutive sets of 1-minute scintillation index data feed the pipeline, each one being processed in less than 1 minute. The consecutive sets are acquired and processed concurrently and asynchronously by the different modules that form the pipeline, automatically exchanging data via the DBMS central hub. Thus, different modules can process data related to different 1-minute sets of data at about the same time, but the pipeline finishes the processing of one set of data at a time following the temporal order of the sets.

7.2 GNSS data acquisition

The scintillation amplitude or phase index is calculated for each GNSS satellite-receiver link of the several constellations (GPS, GLONASS, GALILEO, BEIDOU, SBAS etc) currently available at the GNSS station location. As a consequence, the number of GNSS satellites detectable by a station can exceed 40 in the same minute. These two networks can provide data from up to 44 GNSS stations simultaneously

over the Brazilian territory, or up to 70 considering South America. In addition, for a given constellation, the scintillation amplitude and phase index values are compatible between GNSS stations equipped with different GNSS receivers (PAULA et al., 2021).

Data acquisition provides the starting point for the pipeline of the implemented system, performed by modules "INCT Data Acquisition" and "LISN Data Acquisition". The related challenge was to deal with different GNSS receivers of different manufacturers of the LISN and INCT networks, respectively Novatel and Septentrio. In addition, the data acquisition process was also designed differently for these networks, affecting the way that the data acquired from each station is received at the remote real-time server, being preprocessed and stored in the DBMS of the same server. These tasks must be carried out concurrently and asynchronously in the shortest time possible to be compliant to the real-time demand, and without being subjected to network blockings that may force waiting times when several stations are trying to send data to the remote real-time server concurrently. The original FTP data transfer default schemes of both LISN and INCT networks do not meet real-time requirements, and thus required the implementation of the alternative schemes described below. Data includes not only scintillation index values for 1-minute intervals for all GNSS stations, but also ancillary data like datetime, identifier, azimuthal and elevation angles for each satellite that was locked by the stations.

As for June 2023, when the data acquisition was tested, there were 15 LISN and 29 INCT GNSS monitoring stations currently active in Brazil, and up to 26 LISN stations distributed in other countries of South America, as seen in Figure 7.2. The GNSS stations of these monitoring networks employ different electronic devices and data acquisition software. Each LISN station has a Novatel 4004B receiver connected to a local computer via USB cable, performing data acquisition by the SCINDA software (CARRANO, 2008), being such data transferred via FTP to a central server every 1-minute. Conversely, the INCT stations can employ two different solutions: (i) a stand-alone Septentrio PolaRx5S receiver that compresses and stores the acquired data in its internal persistent flash memory, (ii) a Septentrio PolarRxS PRO receiver connected to a local computer via USB cable running a proprietary software from Septentrio that compresses and stores the acquired data in the local computer hard disk. In both cases, the compressed data of INCT stations is transferred via FTP to a central server every 15-minute or every hour. The Novatel 4004B receiver only acquires data from the GPS and SBAS constellations measuring the S4 index

only for the L1 C/A signal, while the Septentrio PolaRxS PRO and the PolarRx5S receivers acquires data from all available GNSS constellations, with each receiver computing the scintillation amplitude or phase index using the available signals of all constellations, as also explained in Paula et al. (2021).

Figure 7.2 - Geographic location of the GNSS monitoring stations of the LISN and INCT networks, as for June 2023.

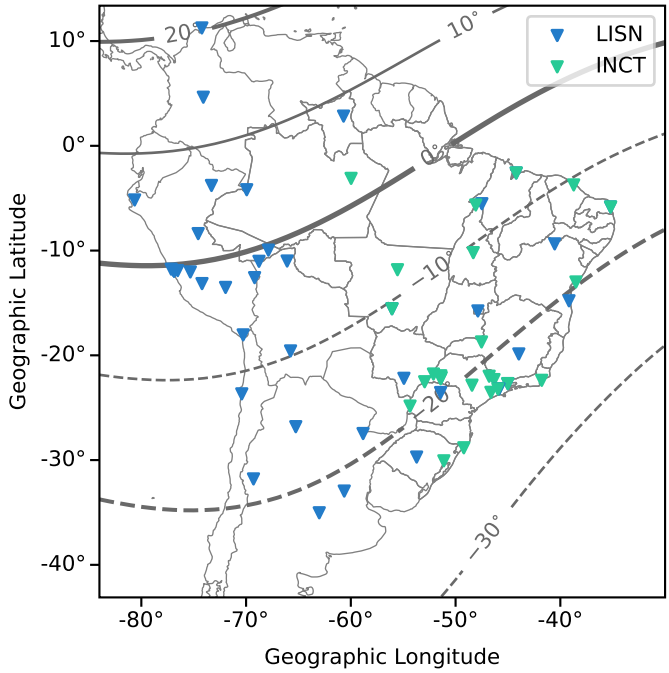

In the case of LISN stations, the solution was straightforward, as the data is already available for each 1-minute interval. A new TCP/IP client software was developed to be executed in the station computer sending data using the HTTP protocol to the remote real-time server, which executes a TCP/IP server software in the "LISN Data Acquisition" module.

In the case of the INCT data acquisition, the default mode precludes even more the real-time operation, since it is configured to acquire consecutive sets of 15 minutes of data, compress it, send via FTP to the real-time server, and then decompress the data and post-process it to calculate the S4 index values. After exploring, implementing and testing some alternative schemes, a particular feature of the INCT Septentrio PolaRx5S receivers was employed. These receivers have an integrated TCP/IP server, which can be configured to transmit incoming data blocks received

from the GNSS satellites. Thus, these data blocks are automatically transmitted via a specific TCP/IP port to the remote real-time server, which executes a new TCP/IP client software. It is worth noting that this alternative is not applicable to the remaining stations with Septentrio PolarRxS PRO receivers, since there are just a few, and are going to be replaced by the former receivers. The Septentrio PolaRx5S receivers provide local real-time calculation of the amplitude or phase index values and ancillary data in the receiver memory, contained in the corresponding ISRM and SatVisibility data blocks. The TCP/IP client software is executed at the remote real-time server, in the "INCT Data Acquisition" module that receives data in the specific TCP/IP port. The TCP/IP client software is multithreaded, and receives each incoming 1-minute dataset creating a new thread. This multithreaded software is resilient to network errors, since in case of connection errors or corrupted datasets, it keeps trying to establish a new connection. Even if the Internet connection is inaccessible to the real-time server itself, once it turns accessible the multithreaded software tries to reestablish the TCP/IP connection with all INCT stations.

Another important difference between the two monitoring networks is the time when the scintillation index is calculated. INCT stations calculate the amplitude or phase index at GPS time, which occurs some seconds before the UTC time, according to the current leap seconds adjustment, which is 18 seconds, while LISN stations calculate the S4 index at UTC time. Therefore, the combined processing of INCT and LISN incoming datasets is synchronized by the reception of the LISN datasets at UTC time, and assuming that the INCT datasets correspond to the same UTC time. Despite this issue, the LISN and INCT datasets refer to the same acquired 1-minute data. In addition, in this work, scintillation maps are generated using 15-minute intervals of data, but a sliding-window advances to the next minute whenever new data is received, thus keeping compliance to the real-time requirement.

7.2.1 Validation of the GNSS data acquisition

An extensive validation was performed to assess the accuracy of the INCT real-time acquired scintillation amplitude or phase index data using the post-processed data that corresponds to real/observed scintillation amplitude or phase index values. The scintillation indexes measured in the INCT stations are calculated by default using 15 min or 1-hour raw data files that are post-processed by a proprietary command line tool (`sbf2ismr`) provided by the receiver microprocessor. Nevertheless, the implemented solution shown here uses the amplitude scintillation index measured in

real-time by the receiver itself, being another source of differences taken into account in the validation.

The validation procedure was performed using 4 classes of amplitude and phase scintillation classes defined by the thresholds seen in Table 7.2, which is similar to Table 4.2, except for not including the ROTI thresholds. Values above the upper limit for the strong class (1.4) were considered outliers, being rounded to 1.4. Values below the lower limit for the null class are considered noise.

Table 7.2 - Four-class scintillation severity thresholds for the amplitude and phase scintillation indexes.

Scintillation Index	**null**	**weak**	**moderate**	**strong**
S4	[0.00-0.15]	(0.15-0.30]	(0.30-0.70]	(0.70-1.40)
σ_ϕ	[0.00-0.15]	(0.15-0.30]	(0.30-0.70]	(0.70-1.40)

The amplitude scintillation index validation employed data from 15 INCT stations, as detailed in Table 7.3, but for the phase scintillation index validation only data from the 11 INCT stations shown in Table 7.5 was employed. Out of these 15 stations, the DMC1, MOR2, PRU2 and PRU4 stations presented higher values for the post-processed phase scintillation index, since all days presented cycle slips, even in time intervals without scintillation.

This validation encompassed observations from 1st of January to 31 of March of 2023, a period that presented high ionospheric scintillation activity. The validation was not necessary for the LISN stations, once the SCINDA software executed in the station computer already post-processes the real-time acquired data. The validation was restricted to the time interval between 21 UT and 9 UT, i.e., after sunset, which is the time interval with occurrences of ionospheric scintillation in Brazil (DE PAULA et al., 2007). In order to filter out data of L-band signals affected by ground interference and the related multipath reflections, only satellite links with elevations higher than 30° were considered. The resulting dataset comprised 64,080 min of observations for each of the 15 INCT stations. If considering that for each 1-minute of observation the number of visible satellites to a station can reach up to 40, and the total number of 1-minute samples would amount to 64,080 × 40 × 15 or 38,448,000

samples.

Table 7.3 - Coordinates of the considered 15 GNSS ionospheric monitoring stations.

Station	**City**	**Geographic**		**Magnetic**
		Latitude	**Longitude**	**Dip Latitude**
STNT	Natal	−5.8406	−35.1962	−15.2186
STCB	Cuiabá	−15.5552	−56.0699	−11.0643
STMC	Monte Carmelo	−18.7240	−47.5238	−18.3375
STPE	Presidente Epitácio	−21.7852	−52.1116	−18.1563
STSJ	São João da Boa Vista	−21.9971	−46.7922	−21.2401
PRU4	Presidente Prudente	−22.1201	−51.4085	−18.7546
PRU2	Presidente Prudente	−22.1220	−51.4071	−18.7546
DMC1	Presidente Prudente	−22.1231	−51.4080	−18.7546
MOR3	Presidente Prudente	−22.1277	−51.4133	−18.7546
STCP	Cachoeira Paulista	−22.7023	−45.0138	−23.2196
SPBO	Botucatu	−22.8525	−48.4323	−21.3238
SJCE	São José dos Campos	−23.2075	−45.8597	−22.5870
SJCU	São José dos Campos	−23.2106	−45.9566	−22.5870
STSH	Santa Helena	−24.8470	−54.3444	−19.2025
STBR	Balneário Rincão	−28.8267	−49.2139	−24.6613

The adopted metrics for the validation were CORR, MAE and STDA, which were evaluated for every satellite, of every constellation of every station, as shown in the summary presented in Table 7.4 and 7.5. Considering averages for all 4 classes of the amplitude scintillation severity, and all the 15 stations, the overall CORR was 0.99950, the overall MAE was 0.00054, and the overall STDA was 0.00402. If considering values per class for all the 15 stations, these values were, respectively for classes null, weak, moderate, and strong, as follows: overall CORR of 0.99980, 0.99992, 0.99935, and 0.99453; overall MAE of 0.00050, 0.00050, 0.00061 and 0.00165; overall STDA of 0.00051, 0.00054, 0.00398, and 0.01533. It can be seen that the validation procedure demonstrated a good accuracy for any class of amplitude scintillation severity. Considering averages for all 4 classes of the phase scintillation severity for all the 11 stations, the overall CORR was 0.99680, the overall MAE was 0.00069, and the overall STDA was 0.00998. If considering values per class for all the 11 sta-

tions, these values were, respectively for classes null, weak, moderate, and strong, as follows: overall CORR of 0.99547, 0.99460, 0.99484, and 0.97609; overall MAE of 0.00049, 0.00072, 0.00186 and 0.01033; overall STDA of 0.00293, 0.00425, 0.01100, and 0.08530. It can be seen that the validation procedure demonstrated a good accuracy for any class of phase scintillation severity.

These results show a good agreement between the scintillation indexes given by the maps and the post-processed real/observed values, during occurrences of ionospheric scintillation.

Table 7.4 - Summary of the amplitude scintillation validation metrics by INCT station.

Station	**CORR**	**MAE**	**STDA**
DMC1	0.99961	0.00054	0.00401
MOR3	0.99958	0.00054	0.00416
PRU2	0.99944	0.00055	0.00480
PRU4	0.99944	0.00056	0.00476
SBPO	0.99940	0.00054	0.00401
SJCE	0.99934	0.00052	0.00330
SJCU	0.99952	0.00052	0.00286
STBR	0.99912	0.00052	0.00281
STCB	0.99985	0.00052	0.00235
STCP	0.99958	0.00052	0.00269
STMC	0.99960	0.00056	0.00447
STNT	0.99939	0.00059	0.00504
STPE	0.99930	0.00059	0.00561
STSH	0.99945	0.00055	0.00405
STSJ	0.99956	0.00053	0.00342

7.3 Scintillation map generation and image rendering

The second stage of the implemented system pipeline is the generation of an interpolated grid from the acquired samples, performed by module “Scintillation Map Generation”, while the third stage of the pipeline is performed by module “Scintillation Map Rendering” that uses the interpolated grids for every minute to render the corresponding scintillation index maps.

Table 7.5 - Summary of the phase scintillation validation metrics by INCT station.

Station	**CORR**	**MAE**	**STDA**
SBPO	0.99573	0.00067	0.01123
SJCE	0.99590	0.00057	0.00873
SJCU	0.99615	0.00058	0.00837
STBR	0.98891	0.00109	0.01003
STCB	0.99812	0.00072	0.00830
STCP	0.99582	0.00058	0.00885
STMC	0.99723	0.00074	0.01202
STNT	0.99821	0.00071	0.00839
STPE	0.99726	0.00078	0.01165
STSH	0.99749	0.00065	0.00916
STSJ	0.99552	0.00062	0.01149

The approach for map generation with GPR(VQI) preprocessing and Gaussian Process Regression interpolation, which was described in Chapter 4, was employed in the implemented real-time system for generation of real-time scintillation maps. The making of scintillation maps requires the interpolation of the values of the considered scintillation index for each IPP of each satellite-receiver link considered as located in the corresponding IPP for the considered area and time interval. IPP locations are derived from the available elevation and azimuthal angles of each satellite-receiver link.

The module "Scintillation Map Generation" was designed to receive real-time scintillation index data pushed by the DBMS. During its initialization, 1 hour of data is retrieved from the DBMS and buffered in memory in order to ensure data continuity. This module generates each interpolated grid from 15 minutes of scintillation index samples received from all GNSS stations. Every minute, a new 1-minute set of samples is received by the module, and a sliding-window that traverses the data samples advances 1 minute, thus disregarding the older 1-minute set of samples. This module has a multithreaded architecture allowing the concurrent tasks of data retrieval and scintillation map generation. The interpolated 193×193 grid points that are generated every minute are stored in a sequence of files compacted in binary format in the scint_map DBMS table.

As mentioned, in the third stage of the pipeline, module "Scintillation Map Rendering" receives real-time interpolated grids pushed by the DBMS for every minute, and employs them to render the resulting scintillation index maps, which are images in the raster format PNG. These images are stored in documents of the DBMS rendered_scint_map table. Finally, in the fourth stage of the pipeline, the DBMS automatically pushes the rendered maps for every minute to the "Web Server" module, which makes them available online with the corresponding interpolated grids.

The "Web Server" module is an API (Application Programming Interface) that implements two HTTP (Hypertext Transfer Protocol) endpoints in order to publish every minute the maps and the corresponding interpolated grids. To optimize the speed of the TCP/IP connections of the connected clients, i.e., the users demanding maps, these endpoints use the WebSocket protocol. This protocol provides full-duplex communication channels over a single TCP/IP connection, and employs the HTTP protocol only during the initial request/response handshake that establishes the connection between the "Web Server" module and a given client. After the connection is established, the TCP/IP connection is kept active until the "Web Server" module, or the client closes the connection. Therefore, whenever new maps are updated every minute, there is no need to open new connections to the clients. Each "Web Server" endpoint waits for the DBMS to push every new document from the scint_map and the rendered_scint_map tables. When a new document arrives, the content is instantly sent to all opened connections, i.e., to all the connected clients to the "Web Server" module.

As an example of the scintillation maps generated by the proposed/implemented approach, Figure 7.3 and 7.4 show, respectively, an hourly sequence of 9 amplitude scintillation maps and phase scintillation maps. These maps allow us to see the evolution of ionospheric irregularities on the night from March 11th to 12th in 2023.

7.4 Discussion and conclusions

It was demonstrated that the real-time generation and online dissemination of scintillation maps covering Brazil is feasible, with all acquisition and preprocessing steps demanding less than 1 second, except for the generation of the interpolated grid that took up to 12 seconds. The real-time capability involves acquiring data from all the 20 available stations of the two GNSS monitoring networks, LISN and INCT, and was achieved using a standard PC as the real-time server. It has a single Intel processor 2.4 GHz with 4 cores, main memory of 64 GBytes. Even assuming the predicted number of near 50 stations for South America in the near future, the current system

Figure 7.3 - Hourly sequence of amplitude scintillation maps generated by the proposed approach showing the evolution of ionospheric irregularities on the night from March 11th to 12th in 2023.

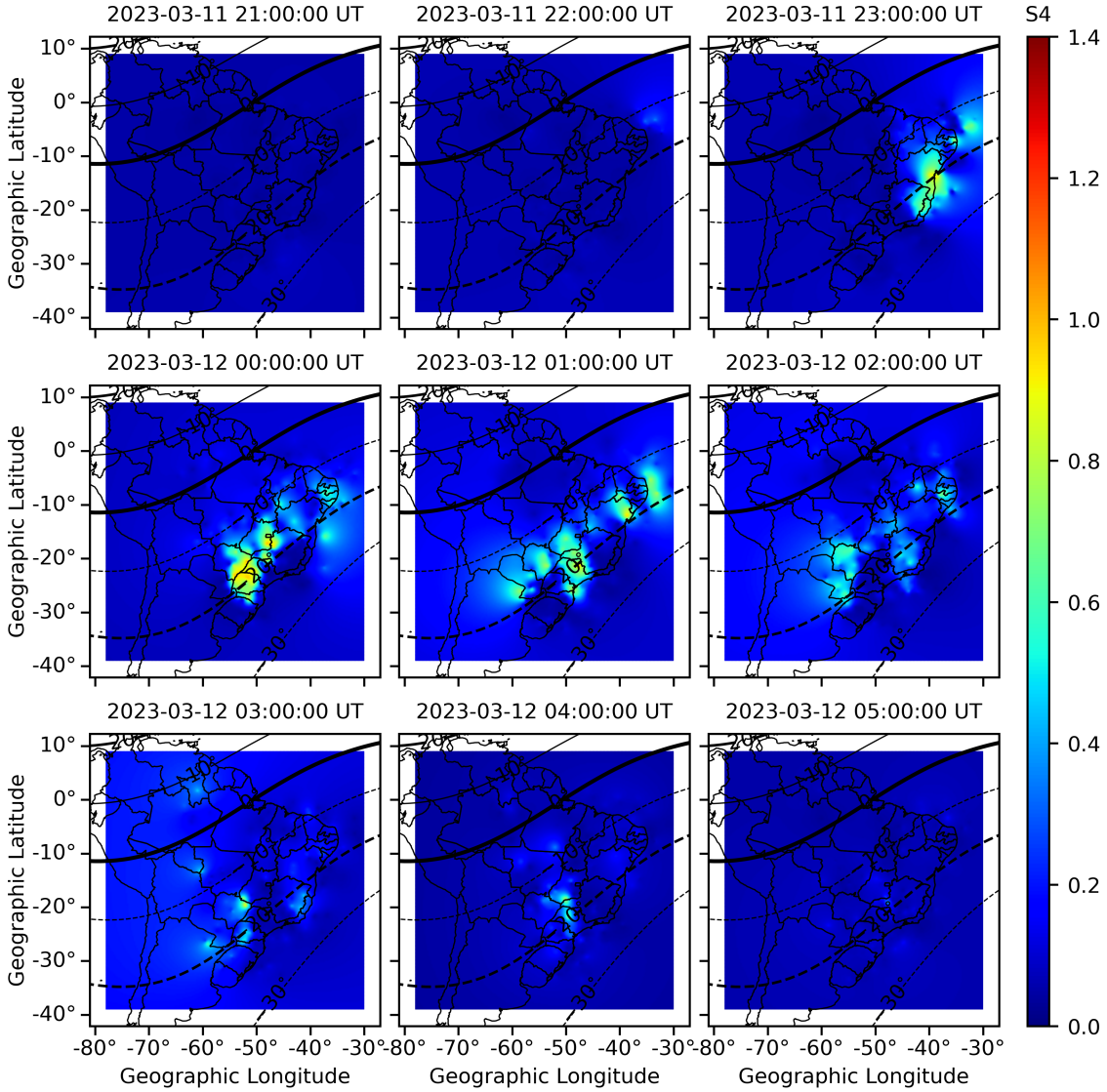

still will be able to provide the proposed real-time capability. The only performance bottleneck would be a heavy demand of users downloading maps, but the web serving module could be easily executed in a separate PC. Any state-of-the-art current server would have at least two processors, with at least 8 cores each one, and a memory of hundreds of GBytes, thus exceeding many times the required processing capability required for all these stations.

Figure 7.4 - Hourly sequence of phase scintillation maps generated by the proposed approach showing the evolution of ionospheric irregularities on the night from March 11th to 12th in 2023.

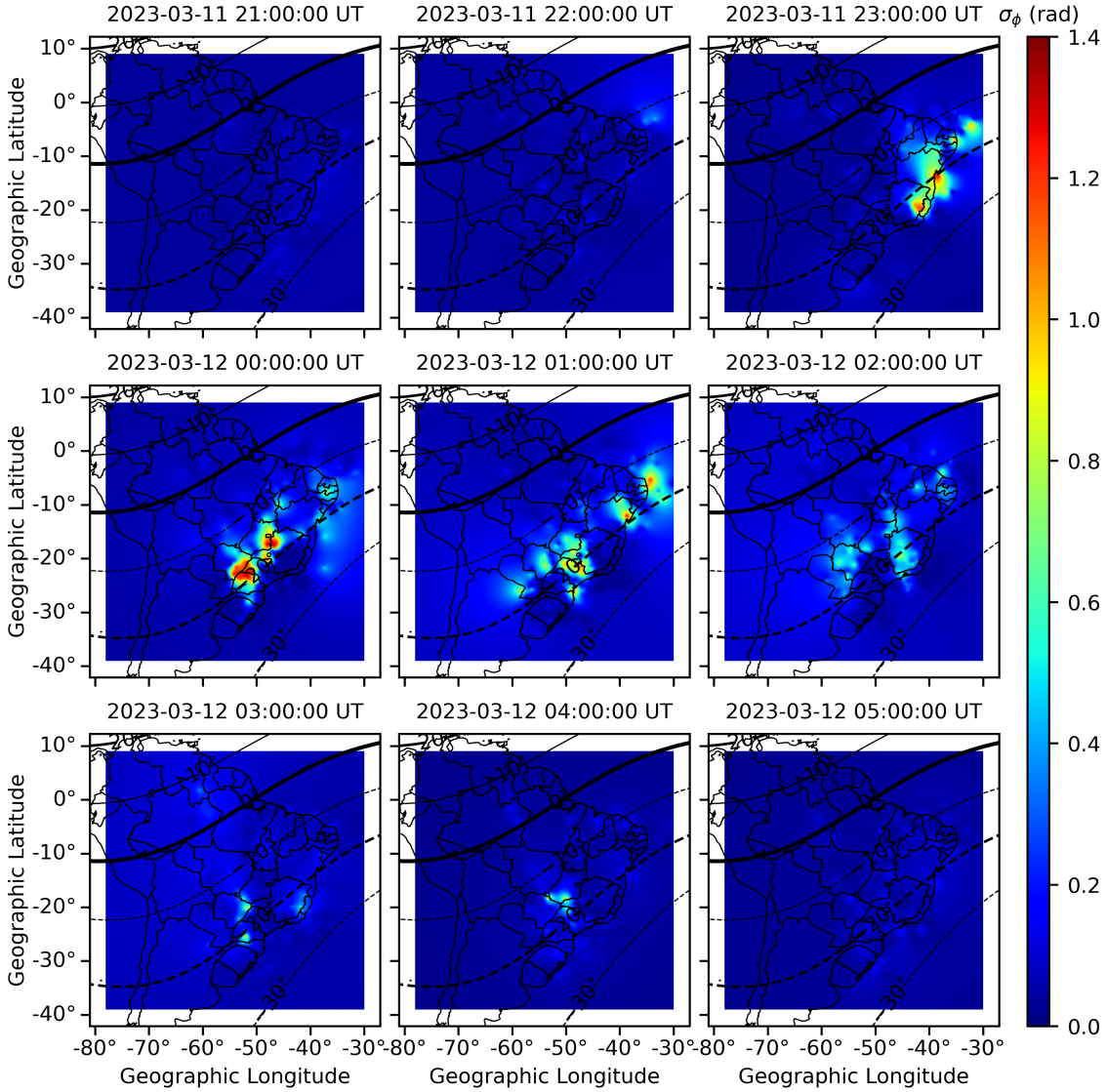

It is expected that the presented real-time generation of ionospheric scintillation index maps will provide warnings for several GNSS-based applications, including aerial navigation, aircraft takeoff and landing procedures, precision agriculture and positioning of offshore oil prospecting platforms. Furthermore, these real-time maps may benefit the research on ionospheric scintillation and/or be assimilated by ionospheric models. As the proposed system proved to be an excellent real-time framework, it is currently being enhanced to support the real-time generation of scintillation prob-

ability maps shown in Chapter 5, and also ROTI maps shown in Chapter 4. Both the scintillation probability and the ROTI maps may support the prediction of occurrence of ionospheric scintillation. Furthermore, the end user deployment of this system is in progress, being expected to make real-time scintillation maps available on the Internet soon. Another further work would be the generation of real-time scintillation maps covering all South America, using all the LISN stations.

8 CONCLUSIONS

This thesis encompasses several contributions, including a new approach for maps of ionospheric indexes that allow to generate better maps, the proposal of using the innovative probability maps corresponding to each of these maps, the implementation of a real-time prototype system for the online dissemination of amplitude and phase scintillation maps that can be easily extended to ROTI maps, and a new approach for the prediction of occurrence of scintillation. All these contributions sum up for a better monitoring and prediction of scintillation with a potential use for operational purposes.

Considering scintillation monitoring, a comparison of maps of different ionospheric indexes for scintillation monitoring and the corresponding probabilities maps was performed. These maps cover the Brazilian territory and part of the neighboring countries. Three indexes were considered: the amplitude scintillation index (S4), the phase scintillation index (σ_ϕ), or the ROTI. Correlation analysis was performed between the maps of these indexes and/or their corresponding probability of occurrence maps. In addition, an error analysis of these maps for a set of locations defined by a set of GNSS stations was also performed. Besides the generation of maps for scintillation monitoring, scintillation prediction was performed with antecedence of 15 minutes using time series of a parameter derived from amplitude scintillation maps or the corresponding probability maps. The future refinement of such prediction may allow the eventual issue of warnings of scintillation occurrences.

All maps were generated using the approach GPR(VQI) developed in the scope of this thesis, which employs interpolation by Gaussian Process Regression and a particular set of preprocessing options (VQI). The corresponding probability maps were also proposed in the scope of this thesis in order to take into account azimuthal and elevation angles for each satellite-station line-of-sight.

Another contribution of the thesis was the development of a prototype with real-time capability, able to receive GNSS data from the set of monitoring stations, pre-process the GNSS data, generate the maps, render the corresponding images and disseminate them using a web server. The real-time capability was already demonstrated for amplitude and phase scintillation maps, using a standard PC as a server. However, the high processing cost of generating ROTI maps would preclude the use of this index for real-time maps using a standard PC as the real-time server, but some kind of parallel processing could be easily employed. For instance, it would be straightforward to use OpenMP in a multi-processed multi-core computer or in

a computer with one or more GPUs.

Yet another contribution is a new algorithm for detection and correction of cycle slips, discontinuities in the receiver carrier phase lock caused by receiver-satellite loss of the lock, and/or by scintillation affecting their RF link. This algorithm detected more cycle slips than the standard ones, thus allowing for better relative STEC measurements. Predictions of scintillation occurrence were performed considering the Brazilian and part of the neighboring countries with antecedence of 15 minutes. Prediction was performed using an ensemble machine learning algorithm (XGBoost). Tests using higher prediction antecedence are envisaged. The validation performed with actual data will soon be started in order to evaluate the maps made available to the users, as well the corresponding predicted maps, concerning scintillation awareness and usefulness to provide warnings of scintillation occurrence.

Future work is expected to continue the proposed research and the corresponding operational implementations in the scope of the INCT NavAer project. ROTI probability maps in real-time and ROTI probability map predictions would be available to the users in some months.

REFERENCES

ABDU, M.; SOBRAL, J.; BATISTA, I.; RIOS, V.; MEDINA, C. Equatorial spread-F occurrence statistics in the american longitudes: diurnal, seasonal and solar cycle variations. **Advances in Space Research**, v. 22, n. 6, p. 851–854, 1998. ISSN 0273-1177. IRI 1997 Symposium: New Developments in Ionospheric Modelling and Prediction. Available from: <<https://www.sciencedirect.com/science/article/pii/S0273117798001112>>. 11

ABDU, M. A. Day-to-day and short-term variabilities in the equatorial plasma bubble/spread F irregularity seeding and development. **Progress in Earth and Planetary Science**, v. 6, n. 1, p. 11, Feb 2019. ISSN 2197-4284. Available from: <<https://doi.org/10.1186/s40645-019-0258-1>>. 9

ABDU, M. A.; SOUZA, J. R. D.; SOBRAL, J. H. A.; BATISTA, I. S. Magnetic storm associated disturbance dynamo effects in the low and equatorial latitude ionosphere. In: TSURUTANI, B.; MCPHERRON, R.; LU, G.; SOBRAL, J. H. A.; GOPALSWAMY, N. (Ed.). **Recurrent magnetic storms: corotating solar wind streams**. American Geophysical Union (AGU), 2006. p. 283–304. ISBN 9781118666456. Available from: <<https://agupubs.onlinelibrary.wiley.com/doi/abs/10.1029/167GM22>>. 13

ALKEN, P.; THÉBAULT, E.; BEGGAN, C. D.; AMIT, H.; AUBERT, J.; BAERENZUNG, J.; BONDAR, T. N.; BROWN, W. J.; CALIFF, S.; CHAMBODUT, A.; CHULLIAT, A.; COX, G. A.; FINLAY, C. C.; FOURNIER, A.; GILLET, N.; GRAYVER, A.; HAMMER, M. D.; HOLSCHNEIDER, M.; HUDER, L.; HULOT, G.; JAGER, T.; KLOSS, C.; KORTE, M.; KUANG, W.; KUVSHINOV, A.; LANGLAIS, B.; LÉGER, J.-M.; LESUR, V.; LIVERMORE, P. W.; LOWES, F. J.; MACMILLAN, S.; MAGNES, W.; MANDEA, M.; MARSAL, S.; MATZKA, J.; METMAN, M. C.; MINAMI, T.; MORSCHHAUSER, A.; MOUND, J. E.; NAIR, M.; NAKANO, S.; OLSEN, N.; PAVÓN-CARRASCO, F. J.; PETROV, V. G.; ROPP, G.; ROTHER, M.; SABAKA, T. J.; SANCHEZ, S.; SATURNINO, D.; SCHNEPF, N. R.; SHEN, X.; STOLLE, C.; TANGBORN, A.; TØFFNER-CLAUSEN, L.; TOH, H.; TORTA, J. M.; VARNER, J.; VERVELIDOU, F.; VIGNERON, P.; WARDINSKI, I.; WICHT, J.; WOODS, A.; YANG, Y.; ZEREN, Z.; ZHOU, B. International geomagnetic reference field: the thirteenth generation. **Earth, Planets and Space**, v. 73, n. 1, p. 49, Feb 2021. ISSN 1880-5981. Available from: <<https://doi.org/10.1186/s40623-020-01288-x>>. 39, 86

AMABAYO, E. B.; ANDIMA, G.; SSENYUNZI, R. C. Instantaneous ionospheric scintillation mapping over the east african region by use of GPS derived amplitude scintillation proxy. **Asian Journal of Research and Reviews in Physics**, v. 4, n. 2, p. 6–20, Apr. 2021. Available from: <<https://journalajr2p.com/index.php/AJR2P/article/view/62>>. 3

BANDYOPADHAYAY, T.; GUHA, A.; DASGUPTA, A.; BANERJEE, P.; BOSE, A. Degradation of navigational accuracy with global positioning system during

periods of scintillation at equatorial latitudes. **Electronics Letters**, v. 33, p. 1010–1011(1), June 1997. ISSN 0013-5194. Available from: <<https://digital-library.theiet.org/content/journals/10.1049/el_19970692>>. 1

BEECK, S. S.; JENSEN, A. B. O. ROTI maps of Greenland using kriging. **Journal of Geodetic Science**, v. 11, n. 1, p. 83–94, 2021. Available from: <<https://doi.org/10.1515/jogs-2020-0123>>. 3

BÉNIGUEL, Y.; CHERNIAK, I.; GARCIA-RIGO, A.; HAMEL, P.; HERNÁNDEZ-PAJARES, M.; KAMENI, R.; KASHCHEYEV, A.; KRANKOWSKI, A.; MONNERAT, M.; NAVA, B.; NGAYA, H.; ORUS-PEREZ, R.; SECRÉTAN, H.; SÉRANT, D.; SCHLÜTER, S.; WILKEN, V. MONITOR ionospheric network: two case studies on scintillation and electron content variability. **Annales Geophysicae**, v. 35, n. 3, p. 377–391, 2017. Available from: <<https://angeo.copernicus.org/articles/35/377/2017/>>. 3

BÉNIGUEL, Y.; HAMEL, P. A global ionosphere scintillation propagation model for equatorial regions. **Journal of Space Weather and Space Climate**, v. 1, n. 1, p. A04, 2011. Available from: <<https://doi.org/10.1051/swsc/2011004>>. 4

CARRANO, C. **GPS-SCINDA: A realtime GPS data acquisition and ionospheric analysis system for SCINDA**. [S.l.]: Boston College, 2008. 97

CARRANO, C. S.; GROVES, K. M.; RINO, C. L. On the relationship between the rate of change of total electron content index (ROTI), irregularity strength (CkL), and the scintillation index (S4). **Journal of Geophysical Research: Space Physics**, v. 124, n. 3, p. 2099–2112, 2019. Available from: <<https://agupubs.onlinelibrary.wiley.com/doi/abs/10.1029/2018JA026353>>. 2, 21, 33

CHERNIAK, I.; KRANKOWSKI, A.; ZAKHARENKOVA, I. ROTI maps: a new IGS ionospheric product characterizing the ionospheric irregularities occurrence. **GPS Solutions**, v. 22, n. 3, p. 69, May 2018. ISSN 1521-1886. Available from: <<https://doi.org/10.1007/s10291-018-0730-1>>. 3

CHERNIAK, I.; ZAKHARENKOVA, I.; KRANKOWSKI, A. IGS ROTI Maps: current status and its extension towards equatorial region and southern hemisphere. **Sensors**, v. 22, n. 10, 2022. ISSN 1424-8220. Available from: <<https://www.mdpi.com/1424-8220/22/10/3748>>. 4

DE FRANCESCHI, G.; SPOGLI, L.; ALFONSI, L.; ROMANO, V.; CESARONI, C.; HUNSTAD, I. The ionospheric irregularities climatology over Svalbard from solar cycle 23. **Scientific Reports**, v. 9, n. 1, p. 9232, Jun 2019. ISSN 2045-2322. Available from: <<https://doi.org/10.1038/s41598-019-44829-5>>. 3

DE PAULA, E. R.; KHERANI, E. A.; ABDU, M. A.; BATISTA, I. S.; SOBRAL, J. H. A.; KANTOR, I. J.; TAKAHASHI, H.; REZENDE, L. F. C. d.; MUELLA, M. T. A. H.; RODRIGUES, F. S.; KINTNER, P. M.; LEDVINA, B. M.; MITCHELL, C.; GROVES, K. M. Characteristics of the ionospheric F-region

plasma irregularities over brazilian longitudinal sector. **Indian Journal of Radio & Space Physics**, v. 36, n. 4, p. 268–277, 2007. ISSN 0975-105X. Available from: <<http://nopr.niscpr.res.in/handle/123456789/4706>>. 2, 100

DOS SANTOS, P. A. **Predição local da cintilação ionosférica em baixa latitude magnética utilizando aprendizado de máquina**. 172 p. Tese (Doutorado em Computação Aplicada) — Instituto Nacional de Pesquisas Espaciais (INPE), São José dos Campos, 2022. Available from: <<http://urlib.net/ibi/8JMKD3MGP3W34T/477R4DL>>. 5, 79

DOS SANTOS, P. A.; STEPHANY, S.; PAULA, E. R. de. A new approach for low-latitude ionospheric scintillation prediction. **Brazilian Journal of Geophysics**, v. 40, n. 4, 2022. ISSN 2764-8044. Available from: <<https://www.sbgf.org.br/revista/index.php/rbgf/article/view/2187>>. 5, 79

HAMEL, P.; SAMBOU, D. C.; DARCES, M.; BENIGUEL, Y.; HÉLIER, M. Kriging method to perform scintillation maps based on measurement and GISM model. **Radio Science**, v. 49, n. 9, p. 746–752, 2014. Available from: <<https://agupubs.onlinelibrary.wiley.com/doi/abs/10.1002/2014RS005470>>. 3

HUMPHREYS, T. E.; LEDVINA, B. M.; PSIAKI, M. L.; KINTNER, P. M. Analysis of ionospheric scintillations using wideband GPS L1 C/A signal data. In: INTERNATIONAL TECHNICAL MEETING OF THE SATELLITE DIVISION OF THE INSTITUTE OF NAVIGATION, 17., Sept. 2004, Long Beach Convention Center. **Proceedings...** Long Beach, CA: ION GNSS, 2004. p. 399–407. 1

INSTITUTO BRASILEIRO DE GEOGRAFIA E ESTATÍSTICA. **Rede brasileira de monitoramento contínuo dos sistemas GNSS**. 2024. Available from: <<http://geoftp.ibge.gov.br/informacoes_sobre_posicionamento_geodesico/rbmc/cartogramas/RBMC_2024.pdf>>. 18

JACOBSEN, K. S. The impact of different sampling rates and calculation time intervals on ROTI values. **Journal of Space Weather and Space Climate**, v. 4, p. A33, 2014. Available from: <<https://doi.org/10.1051/swsc/2014031>>. 21

JONAH, O. F. **Analysis of Total Electron Content (TEC) variations obtained from GPS data over South America**. 145 p. Dissertação (Mestrado em Geofísica Espacial) — Instituto Nacional de Pesquisas Espaciais (INPE), São José dos Campos, 2013. Available from: <<http://urlib.net/ibi/8JMKD3MGP7W/3DHJF42>>. 20

KIEFT, P.; AQUINO, M.; DODSON, A. Using ordinary kriging for the creation of scintillation maps. In: NOTARPIETRO, R.; DOVIS, F.; FRANCESCHI, G. D.; AQUINO, M. (Ed.). **Mitigation of ionospheric threats to GNSS**. Rijeka: IntechOpen, 2014. chapter 6. Available from: <<https://doi.org/10.5772/58781>>. 3, 4

KINTNER, P. M.; KIL, H.; BEACH, T. L.; PAULA, E. R. de. Fading timescales associated with GPS signals and potential consequences. **Radio Science**, v. 36, n. 4, p. 731–743, 2001. Available from: <<https://agupubs.onlinelibrary.wiley.com/doi/abs/10.1029/1999RS002310>>. 1

KINTNER, P. M.; LEDVINA, B. M.; DE PAULA, E. R. An amplitude scintillation test pattern standard for evaluating GPS receiver performance. **Space Weather**, v. 3, n. 3, 2005. Available from: <<https://agupubs.onlinelibrary.wiley.com/doi/abs/10.1029/2003SW000025>>. 1

KOULOURI, A. Real-time ionospheric imaging of S4 scintillation from limited data with parallel kalman filters and smoothness. **IEEE Transactions on Geoscience and Remote Sensing**, v. 60, p. 1–12, 2022. 3

LEICK, A. **GPS satellite surveying**. 2. ed. [S.l.]: Wiley, 1995. ISBN 9780471306269. 1

LI, J.; MA, G.; MARUYAMA, T.; WAN, Q.; FAN, J.; ZHANG, J.; WANG, X. ROTI keograms based on CMONOC to characterize the ionospheric irregularities in 2014. **Earth, Planets and Space**, v. 74, n. 1, p. 149, Oct 2022. ISSN 1880-5981. Available from: <<https://doi.org/10.1186/s40623-022-01708-0>>. 24, 35

LIMA, G. R. T. de; STEPHANY, S.; PAULA, E. R. de; BATISTA, I. S.; ABDU, M. A.; REZENDE, L. F. C.; AQUINO, M. G. S.; DUTRA, A. P. S. Correlation analysis between the occurrence of ionospheric scintillation at the magnetic equator and at the southern peak of the equatorial ionization anomaly. **Space Weather**, v. 12, n. 6, p. 406–416, 2014. Available from: <<https://agupubs.onlinelibrary.wiley.com/doi/abs/10.1002/2014SW001041>>. 4, 5, 79

LIMA, G. R. T. de; STEPHANY, S.; PAULA, E. R. de; BATISTA, I. S.; ABDU, M. A. Prediction of the level of ionospheric scintillation at equatorial latitudes in Brazil using a neural network. **Space Weather**, v. 13, n. 8, p. 446–457, 2015. Available from: <<https://agupubs.onlinelibrary.wiley.com/doi/abs/10.1002/2015SW001182>>. 4, 5, 79

MARTINON, A. R. F.; STEPHANY, S.; PAULA, E. R. Ionospheric scintillation awareness for GPS and other constellations by probability maps. In: SIMPÓSIO BRASILEIRO DE GEOINFORMÁTICA, 23., 2022, INPE. **Proceedings...** São José dos Campos: GEOINFO, 2022. ISSN 2179-4847. Available from: <<http://urlib.net/ibi/8JMKD3MGPDW34P/487MADB>>. 2, 6, 59, 65

MARTINON, A. R. F.; STEPHANY, S.; PAULA, E. R. d. Challenges in real-time generation of scintillation index maps. **Boletim de Ciências Geodésicas**, v. 30, p. e2024004, 2024. ISSN 1982-2170. Available from: <<https://doi.org/10.1590/s1982-21702024000100004>>. 7, 93, 94

MARTINON, A. R. F.; STEPHANY, S.; PAULA, E. R. de. A new approach for the generation of real-time GNSS low-latitude ionospheric scintillation maps. **Journal of Space Weather and Space Climate**, v. 13, p. 18, 2023. Available from: <<https://doi.org/10.1051/swsc/2023015>>. 3, 6, 24, 37, 47

MCGRANAGHAN, R. M.; MANNUCCI, A. J.; WILSON, B.; MATTMANN, C. A.; CHADWICK, R. New capabilities for prediction of high-latitude ionospheric scintillation: a novel approach with machine learning. **Space Weather**, v. 16, n. 11, p. 1817–1846, 2018. Available from: <<https://agupubs.onlinelibrary.wiley.com/doi/abs/10.1029/2018SW002018>>. 5

MONICO, J. F. G.; PAULA, E. R. d.; MORAES, A. d. O.; COSTA, E.; SHIMABUKURO, M. H.; ALVES, D. B. M.; SOUZA, J. R. d.; CAMARGO, P. d. O.; PROL, F. d. S.; VANI, B. C.; PEREIRA, V. S. A.; JUNIOR, P. S. d. O.; TSUCHIYA, I.; AGUIAR, C. R. The GNSS NavAer INCT project overview and main results. **Journal of Aerospace Technology and Management**, v. 14, p. e0722, 2022. ISSN 2175-9146. Available from: <<https://doi.org/10.1590/jatm.v14.1249>>. 2

MORAES, A. d. O.; VANI, B. C.; COSTA, E.; ABDU, M. A.; PAULA, E. R. de; SOUSASANTOS, J.; MONICO, J. a. F. G.; FORTE, B.; NEGRETI, P. M. de S.; SHIMABUKURO, M. H. GPS availability and positioning issues when the signal paths are aligned with ionospheric plasma bubbles. **GPS Solutions**, v. 22, n. 4, p. 95, Jul 2018. ISSN 1521-1886. Available from: <<https://doi.org/10.1007/s10291-018-0760-8>>. 15

MORAES, A. de O.; COSTA, E.; ABDU, M. A.; RODRIGUES, F. S.; PAULA, E. R. de; OLIVEIRA, K.; PERRELLA, W. J. The variability of low-latitude ionospheric amplitude and phase scintillation detected by a triple-frequency GPS receiver. **Radio Science**, v. 52, n. 4, p. 439–460, 2017. Available from: <<https://agupubs.onlinelibrary.wiley.com/doi/abs/10.1002/2016RS006165>>. 20

MORTON, Y. J.; YANG, Z.; BREITSCH, B.; BOURNE, H.; RINO, C. Ionospheric effects, monitoring, and mitigation techniques. In: MORTON, Y. J.; DIGGELEN, F.; SPILKER JUNIOR, J. J.; PARKINSON, B. W.; LO, S.; GAO, G. (Ed.). **Position, navigation, and timing technologies in the 21st century**. John Wiley & Sons, 2020. chapter 31, p. 879–937. ISBN 9781119458449. Available from: <<https://onlinelibrary.wiley.com/doi/abs/10.1002/9781119458449.ch31>>. 3

MUELLA, M. T. A. H.; KHERANI, E. A.; PAULA, E. R. de; CERRUTI, A. P.; KINTNER, P. M.; KANTOR, I. J.; MITCHELL, C. N.; BATISTA, I. S.; ABDU, M. A. Scintillation-producing fresnel-scale irregularities associated with the regions of steepest TEC gradients adjacent to the equatorial ionization anomaly. **Journal of Geophysical Research: Space Physics**, v. 115, n. A3, 2010. Available from: <<https://agupubs.onlinelibrary.wiley.com/doi/abs/10.1029/2009JA014788>>. 4

NGUYEN, C. T.; OLUWADARE, S. T.; LE, N. T.; ALIZADEH, M.; WICKERT, J.; SCHUH, H. Spatial and temporal distributions of ionospheric irregularities derived from regional and global ROTI maps. **Remote Sensing**, v. 14, n. 1, 2022. ISSN 2072-4292. Available from: <<https://www.mdpi.com/2072-4292/14/1/10>>. 3

PAULA, E. de; RODRIGUES, F.; IYER, K.; KANTOR, I.; ABDU, M.; KINTNER, P.; LEDVINA, B.; KIL, H. Equatorial anomaly effects on GPS scintillations in Brazil. **Advances in Space Research**, v. 31, n. 3, p. 749–754, 2003. ISSN 0273-1177. Description of the Low Latitude and Equatorial Ionosphere in the International Reference Ionosphere. Available from: <<https://www.sciencedirect.com/science/article/pii/S0273117703000486>>. 10

PAULA, E. R. de; MARTINON, A. R. F.; CARRANO, C.; MORAES, A. O.; NERI, J. A. C. F.; CECATTO, J. R.; ABDU, M. A.; CUNHA NETO, A.; MONICO, J. a. F. G.; SILVA, W. da C.; VANI, B. C.; BATISTA, I. S.; MENDES, O.; SOUZA, J. R. de; SILVA, A. L. A. Solar flare and radio burst effects on GNSS signals and the ionosphere during september 2017. **Radio Science**, v. 57, n. 10, p. e2021RS007418, 2022. E2021RS007418 2021RS007418. Available from: <<https://agupubs.onlinelibrary.wiley.com/doi/abs/10.1029/2021RS007418>>. 14, 15

PAULA, E. R. de; MARTINON, A. R. F.; MORAES, A. O.; CARRANO, C.; NETO, A. C.; DOHERTY, P.; GROVES, K.; VALLADARES, C. E.; CROWLEY, G.; AZEEM, I.; REYNOLDS, A.; AKOS, D. M.; WALTER, T.; BEACH, T. L.; SLEWAEGEN, J.-M. Performance of 6 different global navigation satellite system receivers at low latitude under moderate and strong scintillation. **Earth and Space Science**, v. 8, n. 2, p. e2020EA001314, 2021. E2020EA001314 2020EA001314. Available from: <<https://agupubs.onlinelibrary.wiley.com/doi/abs/10.1029/2020EA001314>>. 19, 33, 97, 98

PAULA, E. R. de; MONICO, J. F. G.; TSUCHIYA, I. H.; VALLADARES, C. E.; COSTA, S. M. A.; MARINI-PEREIRA, L.; VANI, B. C.; MORAES, A. d. O. A retrospective of global navigation satellite system ionospheric irregularities monitoring networks in Brazil. **Journal of Aerospace Technology and Management**, v. 15, p. e0123, 2023. ISSN 2175-9146. Available from: <<https://doi.org/10.1590/jatm.v15.1288>>. 2, 17

PAULA, E. R. de; MORAES, A. de O.; MONICO, J. F. G. Ionospheric scintillation characteristics and their effects over GNSS signal and position and navigation systems in the brazilian region. **Brazilian Journal of Geophysics**, v. 40, n. 5, 2022. ISSN 2764-8044. Available from: <<https://www.sbgf.org.br/revista/index.php/rbgf/article/view/2151>>. 13, 14, 16

PAULA, E. R. de; MORAES, A. O.; ABDU, M. A.; SOBRAL, J. H. A.; BATISTA, I. S.; KHERANI, E. A.; TAKAHASHI, H.; COSTA, E. Long term

studies on ionospheric scintillation and plasma bubbles. In: WILKINSON, P.; CANNON, P. S.; STONE, W. R. (Ed.). **100 years of the International Union of Radio Science**. URSI, International Union of Radio Science, 2021. chapter 29, p. 557–562. ISBN 9789463968034. Available from: <<https://ursi.org/Publications/URSI100/URSI100_book.pdf>>. 10

PAULA, E. R. de; OLIVEIRA, C. B. A. de; CATON, R. G.; NEGRETI, P. M.; BATISTA, I. S.; MARTINON, A. R. F.; CUNHA NETO, A.; ABDU, M. A.; MONICO, J. F. G.; SOUSASANTOS, J.; MORAES, A. O. Ionospheric irregularity behavior during the september 6–10, 2017 magnetic storm over brazilian equatorial–low latitudes. **Earth, Planets and Space**, v. 71, n. 1, p. 42, Apr 2019. ISSN 1880-5981. Available from: <<https://doi.org/10.1186/s40623-019-1020-z>>. 12

PI, X.; MANNUCCI, A. J.; LINDQWISTER, U. J.; HO, C. M. Monitoring of global ionospheric irregularities using the worldwide GPS network. **Geophysical Research Letters**, v. 24, n. 18, p. 2283–2286, 1997. Available from: <<https://agupubs.onlinelibrary.wiley.com/doi/abs/10.1029/97GL02273>>. 21

PI, X.; MANNUCCI, A. J.; VALANT-SPAIGHT, B.; BAR-SEVER, Y.; ROMANS, L. J.; SKONE, S.; SPARKS, L.; HALL, G. M. **Observations of global and regional ionospheric irregularities and scintillation using GNSS tracking networks**. Pasadena, CA: Jet Propulsion Laboratory, National Aeronautics and Space Administration, 2013, 2013. Available from: <<https://hdl.handle.net/2014/45695>>. 3

PROL, F. d. S.; CAMARGO, P. d. O.; MUELLA, M. T. d. A. H. Comparative study of methods for calculating ionospheric points and describing the GNSS signal path. **Boletim de Ciências Geodésicas**, v. 23, n. 4, p. 669–683, Oct 2017. ISSN 1982-2170. Available from: <<https://doi.org/10.1590/S1982-21702017000400044>>. 24

RETTERER, J. M. Forecasting low-latitude radio scintillation with 3-d ionospheric plume models: 2. scintillation calculation. **Journal of Geophysical Research: Space Physics**, v. 115, n. A3, 2010. Available from: <<https://agupubs.onlinelibrary.wiley.com/doi/abs/10.1029/2008JA013840>>. 4

REZENDE, L. F. C.; PAULA, E. R. de; STEPHANY, S.; KANTOR, I. J.; MUELLA, M. T. A. H.; SIQUEIRA, P. M. de; CORREA, K. S. Survey and prediction of the ionospheric scintillation using data mining techniques. **Space Weather**, v. 8, n. 6, 2010. Available from: <<https://agupubs.onlinelibrary.wiley.com/doi/abs/10.1029/2009SW000532>>. 4, 5, 79

REZENDE, L. F. C. de. **Mineração de dados aplicada à análise e predição de cintilação ionosférica**. Dissertação (Mestrado em Computação Aplicada) — Instituto Nacional de Pesquisas Espaciais (INPE), São José dos Campos, 2009. Available from: <<http://urlib.net/sid.inpe.br/mtc-m18@80/2009/06.22.15.52>>. 4, 5, 79

REZENDE, L. F. C. de; PAULA, E. R. de; KANTOR, I. J.; KINTNER, P. M. Mapping and survey of plasma bubbles over brazilian territory. **Journal of Navigation**, v. 60, n. 1, p. 69–81, 2007. Available from: <<https://doi.org/10.1017/S0373463307004006>>. 3, 11, 37

RINO, C. L. A power law phase screen model for ionospheric scintillation: 1. weak scatter. **Radio Science**, v. 14, n. 6, p. 1135–1145, 1979. Available from: <<https://agupubs.onlinelibrary.wiley.com/doi/abs/10.1029/RS014i006p01135>>. 23, 28

RODRIGUES, F. S. **Estudo das irregularidades ionosféricas equatoriais utilizando GPS**. 175 p. Dissertação (Mestrado em Geofísica Espacial) — Instituto Nacional de Pesquisas Espaciais (INPE), São José dos Campos, 2003. Available from: <<http://urlib.net/ibi/6qtX3pFwXQZGivnK2Y/TcHKB>>. 12

SAITO, S.; HOSOKAWA, K.; SAKAI, J.; TOMIZAWA, I. Study of structures of the sporadic E layer by using dense GNSS network observations. **NAVIGATION: Journal of the Institute of Navigation**, v. 68, n. 4, p. 751–758, 2021. ISSN 0028-1522. Available from: <<https://navi.ion.org/content/68/4/751>>. 4

SATO, H.; KIM, J. S.; OTSUKA, Y.; WRASSE, C. M.; PAULA, E. R. d.; SOUZA, J. R. d. L-band synthetic aperture radar observation of ionospheric density irregularities at equatorial plasma depletion region. **Geophysical Research Letters**, v. 48, n. 16, p. e2021GL093541, 2021. E2021GL093541 2021GL093541. Available from: <<https://agupubs.onlinelibrary.wiley.com/doi/abs/10.1029/2021GL093541>>. 2, 60

SKONE, S.; KNUDSEN, K.; DE JONG, M. Limitations in GPS receiver tracking performance under ionospheric scintillation conditions. **Physics and Chemistry of the Earth, Part A: Solid Earth and Geodesy**, v. 26, n. 6, p. 613–621, 2001. ISSN 1464-1895. Available from: <<https://www.sciencedirect.com/science/article/pii/S1464189501001107>>. 1

SPOGLI, L.; ALFONSI, L.; FRANCESCHI, G. D.; ROMANO, V.; AQUINO, M. H. O.; DODSON, A. Climatology of GPS ionospheric scintillations over high and mid-latitude european regions. **Annales Geophysicae**, v. 27, n. 9, p. 3429–3437, 2009. Available from: <<https://angeo.copernicus.org/articles/27/3429/2009/>>. 23

SPOGLI, L.; ALFONSI, L.; ROMANO, V.; FRANCESCHI, G. D.; MONICO, J. F. G.; SHIMABUKURO, M. H.; BOUGARD, B.; AQUINO, M. Assessing the GNSS scintillation climate over Brazil under increasing solar activity. **Journal of Atmospheric and Solar-Terrestrial Physics**, v. 105-106, p. 199–206, 2013. ISSN 1364-6826. Available from: <<https://www.sciencedirect.com/science/article/pii/S1364682613002605>>. 23, 28, 29

STAFFORD, J. V. Implementing precision agriculture in the 21st century. **Journal of Agricultural Engineering Research**, v. 76, n. 3, p. 267–275, 2000.

ISSN 0021-8634. Available from: <<https://www.sciencedirect.com/science/article/pii/S0021863400905778>>. 4

VALLADARES, C. TEC depletions and scintillation measurements in south america. In: AGU FALL MEETING, Dec. 11-15, 2023. **Proceedings...** San Francisco, CA, USA: AGU, 2023. On the session G54A-03. 11

VALLADARES, C. E.; CHAU, J. L. The low-latitude ionosphere sensor network: initial results. **Radio Science**, v. 47, n. 4, 2012. Available from: <<https://agupubs.onlinelibrary.wiley.com/doi/abs/10.1029/2011RS004978>>. 16

VAN DIERENDONCK, A.; ARBESSER-RASTBURG, B. Measuring ionospheric scintillation in the equatorial region over africa, including measurements from SBAS geostationary satellite signals. In: INTERNATIONAL TECHNICAL MEETING OF THE SATELLITE DIVISION OF THE INSTITUTE OF NAVIGATION, 17., Sept. 21 - 24, 2004. **Proceedings...** Long Beach, CA, USA: ION GPS, 2004. p. 316–324. 20

VAN DIERENDONCK, A.; KLOBUCHAR, J.; HUA, Q. Ionospheric scintillation monitoring using commercial single frequency C/A code receivers. In: INTERNATIONAL TECHNICAL MEETING OF THE SATELLITE DIVISION OF THE INSTITUTE OF NAVIGATION, 6., Sept. 22 - 24, 1993. **Proceedings...** Salt Lake City, UT, USA: ION GPS, 1993. p. 1333–1342. 19, 20

VANI, B. C. **Investigações sobre modelagem, mitigação e predição de cintilação ionosférica na região brasileira**. Tese (Doutorado em Ciências Cartográficas) — Universidade Estadual Paulista (Unesp), Faculdade de Ciências e Tecnologia, Presidente Prudente, 2018. Available from: <<http://hdl.handle.net/11449/153701>>. 3, 5, 37, 79

VANI, B. C.; SHIMABUKURO, M. H.; MONICO, J. F. G. Visual exploration and analysis of ionospheric scintillation monitoring data: the ISMR Query Tool. **Computers & Geosciences**, v. 104, p. 125–134, 2017. ISSN 0098-3004. Available from: <<https://www.sciencedirect.com/science/article/pii/S0098300416303065>>. 17

WERNIK, A. W.; ALFONSI, L.; MATERASSI, M. Scintillation modeling using in situ data. **Radio Science**, v. 42, n. 1, 2007. Available from: <<https://agupubs.onlinelibrary.wiley.com/doi/abs/10.1029/2006RS003512>>. 4

YOKOYAMA, T. A review on the numerical simulation of equatorial plasma bubbles toward scintillation evaluation and forecasting. **Progress in Earth and Planetary Science**, v. 4, n. 1, p. 37, Dec 2017. ISSN 2197-4284. Available from: <<https://doi.org/10.1186/s40645-017-0153-6>>. 4

ZHAO, D.; LI, W.; LI, C.; HANCOCK, C. M.; ROBERTS, G. W.; WANG, Q. Analysis on the ionospheric scintillation monitoring performance of ROTI extracted from GNSS observations in high-latitude regions. **Advances in Space**

Research, v. 69, n. 1, p. 142–158, 2022. ISSN 0273-1177. Available from: <<https://www.sciencedirect.com/science/article/pii/S027311772100733X>>. 3

ZHAO, X.; LI, G.; XIE, H.; HU, L.; SUN, W.; YANG, S.; LI, Y.; NING, B.; TAKAHASHI, H. The prediction of day-to-day occurrence of low latitude ionospheric strong scintillation using gradient boosting algorithm. **Space Weather**, v. 19, n. 12, p. e2021SW002884, 2021. E2021SW002884 2021SW002884. Available from: <<https://agupubs.onlinelibrary.wiley.com/doi/abs/10.1029/2021SW002884>>. 5, 79

APPENDIX A - LISN S4 DATA FORMAT

The S4 data files obtained from the LISN website follow the format presented in Table A.1. The data blocks for PRN, S4, az and el repeats n times according to the field 04 value.

Table A.1 - LISN S4 file format.

Field	Description	Units
01	Two digit year.	
02	Day of year (1-366).	
03	Seconds since midnight (0-86400).	
04	Number of data records (containing PRN, S4, az, el) for this epoch.	
05	PRN of first satellite.	
06	S4 of first satellite.	dimensionless
07	Azimuth of first satellite, az.	degrees
08	Elevation of first satellite, el.	degrees
09	PRN of second satellite.	
10	S4 of second satellite.	dimensionless
11	Azimuth of second satellite, az.	degrees
12	Elevation of second satellite, el.	degrees
13	...	

APPENDIX B - SEPTENTRIO ISMR DATA FORMAT

The following description of the ISMR file was obtained executing the Septentrio command line tool `sbf2ismr`, distributed by Septentrio in the RXtools package at <https://www.septentrio.com/en/products/gps-gnss-receiver-software/rxtools>.

```
Format of the ISMR output file
------------------------------
Note: "Sig1" means L1CA for GPS/GLONASS/SBAS/QZSS, E1 for GALILEO,
       B1I for BeiDou and L5 for IRNSS.
      "Sig2" means L2C for GPS/GLONASS/QZSS, E5a for GALILEO, L5
       for SBAS, B2b for BeiDou.
      "Sig3" means L5 for GPS/QZSS, E5b for GALILEO, B3 for
       BeiDou.

Col  1: WN, GPS Week Number
Col  2: TOW, GPS Time of Week (seconds)
Col  3: SVID (see numbering convention below in
        Satellite ID)
Col  4: Value of the RxState field of the ReceiverStatus
        SBF block
Col  5: Azimuth (degrees)
Col  6: Elevation (degrees)
Col  7: Average Sig1 C/N0 over the last minute (dB-Hz)
Col  8: Total S4 on Sig1 (dimensionless)
Col  9: Correction to total S4 on Sig1 (thermal noise
        component only) (dimensionless)
Col 10: Phi01 on Sig1,  1-second phase sigma (radians)
Col 11: Phi03 on Sig1,  3-second phase sigma (radians)
Col 12: Phi10 on Sig1, 10-second phase sigma (radians)
Col 13: Phi30 on Sig1, 30-second phase sigma (radians)
Col 14: Phi60 on Sig1, 60-second phase sigma (radians)
Col 15: AvgCCD on Sig1, average of code/carrier divergence
        (meters)
Col 16: SigmaCCD on Sig1, standard deviation of code/carrier
        divergence (meters)
Col 17: TEC at TOW-45s (TECU), taking calibration into account
        (see -C option)
Col 18: dTEC from TOW-60s to TOW-45s (TECU)
```

```
Col 19: TEC at TOW-30s (TECU), taking calibration into account
        (see -C option)
Col 20: dTEC from TOW-45s to TOW-30s (TECU)
Col 21: TEC at TOW-15s (TECU), taking calibration into account
        (see -C option)
Col 22: dTEC from TOW-30s to TOW-15s (TECU)
Col 23: TEC at TOW (TECU), taking calibration into account
        (see -C option)
Col 24: dTEC from TOW-15s to TOW (TECU)
Col 25: Sig1 lock time (seconds)
Col 26: sbf2ismr version number
Col 27: Lock time on the second frequency used for the TEC
        computation (seconds)
Col 28: Averaged C/N0 of second frequency used for the TEC
        computation (dB-Hz)
Col 29: SI Index on Sig1:
        (10*log10(Pmax)-10*log10(Pmin))/
        (10*log10(Pmax)+10*log10(Pmin)) (dimensionless)
Col 30: SI Index on Sig1, numerator only:
        10*log10(Pmax)-10*log10(Pmin) (dB)
Col 31: p on Sig1, spectral slope of detrended phase in the 0.1 to
        25Hz range (dimensionless)
Col 32: Average Sig2 C/N0 over the last minute (dB-Hz)
Col 33: Total S4 on Sig2 (dimensionless)
Col 34: Correction to total S4 on Sig2 (thermal noise component
        only) (dimensionless)
Col 35: Phi01 on Sig2,  1-second phase sigma (radians)
Col 36: Phi03 on Sig2,  3-second phase sigma (radians)
Col 37: Phi10 on Sig2, 10-second phase sigma (radians)
Col 38: Phi30 on Sig2, 30-second phase sigma (radians)
Col 39: Phi60 on Sig2, 60-second phase sigma (radians)
Col 40: AvgCCD on Sig2, average of code/carrier divergence
        (meters)
Col 41: SigmaCCD on Sig2, standard deviation of code/carrier
        divergence (meters)
Col 42: Sig2 lock time (seconds)
Col 43: SI Index on Sig2 (dimensionless)
Col 44: SI Index on Sig2, numerator only (dB)
Col 45: p on Sig2, phase spectral slope in the 0.1 to 25Hz range
        (dimensionless)
```

Col 46: Average Sig3 C/N0 over the last minute (dB-Hz)
Col 47: Total S4 on Sig3 (dimensionless)
Col 48: Correction to total S4 on Sig3 (thermal noise component only) (dimensionless)
Col 49: Phi01 on Sig3, 1-second phase sigma (radians)
Col 50: Phi03 on Sig3, 3-second phase sigma (radians)
Col 51: Phi10 on Sig3, 10-second phase sigma (radians)
Col 52: Phi30 on Sig3, 30-second phase sigma (radians)
Col 53: Phi60 on Sig3, 60-second phase sigma (radians)
Col 54: AvgCCD on Sig3, average of code/carrier divergence (meters)
Col 55: SigmaCCD on Sig3, standard deviation of code/carrier divergence (meters)
Col 56: Sig3 lock time (seconds)
Col 57: SI Index on Sig3 (dimensionless)
Col 58: SI Index on Sig3, numerator only (dB)
Col 59: p on Sig3, phase spectral slope in the 0.1 to 25Hz range (dimensionless)
Col 60: T on Sig1, phase power spectral density at 1 Hz (rad^2/Hz)
Col 61: T on Sig2, phase power spectral density at 1 Hz (rad^2/Hz)
Col 62: T on Sig3, phase power spectral density at 1 Hz (rad^2/Hz)

Satellite ID (Col 3 - SVID)

The following ranges are defined:
1-37: PRN number of a GPS satellite
38-61: Slot number of a GLONASS satellite with an offset of 37 (R01 to R24)
62: GLONASS satellite of which the slot number is not known
63-68: Slot number of a GLONASS satellite with an offset of 38 (R25 to R30)
71-106: PRN number of a GALILEO satellite with an offset of 70
107-119: L-Band (MSS) satellite. Corresponding satellite name can be found in the LBandBeams block.
120-140: PRN number of an SBAS satellite (S120 to S140)
141-177: PRN number of a BeiDou satellite with an offset of 140
181-187: PRN number of a QZSS satellite with an offset of 180
191-197: PRN number of an IRNSS satellite with an offset of 190
198-215: PRN number of an SBAS satellite with an offset of 157 (S141 to S158)

APPENDIX C - STEC DATA FILE FORMAT

The RINEX files obtained from the INCT and RBMC networks are converted to a simpler data format, in this case a CSV file. The description of each column is detailed in Table C.1. This conversion was implemented using an existing Python library called "gnss-tec", available at Github (<https://github.com/gnss-lab/gnss-tec>) and also at the official Python package repository PyPi (<https://pypi.org/project/gnss-tec/>). However, there was an error in this code, which was corrected and committed to the personal github account of the author: <https://github.com/andremartinon/gnss-tec/>.

Table C.1 - STEC data file format.

Field	**Description**
datetime	Observation day and time in format "yyyy-mm-dd hh:mm:ss".
system_time	Time system of the observations, e.g. GPS.
satellite	Current satellite, e.g. G01.
glo_freq_num	GLONASS frequency number for the satellite.
phase_sig1	Phase observation values for first frequency.
phase_sig2	Phase observation values for second frequency.
phase_code_sig1	Phase observation type for first frequency, e.g. L1.
phase_code_sig2	Phase observation type for second frequency, e.g. L2.
signal_strength	Signal strength on the main (e.g. L1CA) frequency.
p_range_sig1	Pseudorange observation for first frequency.
p_range_sig2	Pseudorange observation for second frequency.
p_range_code_sig1	Pseudorange observation type for first frequency, e.g. P1.
p_range_code_sig2	Pseudorange observation type for second frequency, e.g. P2.
lli_sig1	Value of the bit 0 of loss of lock indicator (LLI) for the phase observation on the first frequency.
lli_sig2	Value of the bit 0 of loss of lock indicator (LLI) for the phase observation on the second frequency.

continue

Table C.1 - Conclusion.

Field	**Description**
validity	Validity index, where: Bit 0: reserved Bit 1: reserved Bit 2 set: lli[2] != 0 Bit 3 set: lli[1] != 0 Bit 4 set: p_range[2] != 0 Bit 5 set: p_range[1] != 0 Bit 6 set: phase[2] != 0 Bit 7 set: phase[1] != 0
phase_tec	Phase total electron content. Value will be NaN if some observations are missing.
p_range_tec	Pseudorange total electron content. Value will be NaN if some observations are missing.
prn	Observed satellite identifier, e.g. 01.
station	Acronym of the monitoring station.
constellation	GNSS constellation to which the satellite belongs: GPS, SBAS, GLONASS, GALILEO and BEIDOU.
network	Monitoring network name: INCT or RBMC.

APPENDIX D - COMPLETE ERROR EVALUATION AND CORRELATION TABLES

Table D.1 - Complete amplitude scintillation maps error evaluation and correlation.

Night	Option	MAE	RMSE	MXAE	MMAX	MMIN	STDA	CORR
2023-03-08	SMR	0.0715	0.1361	0.6410	0.6381	-0.2240	0.1158	0.8403
	SMI	0.0641	0.1205	0.5936	0.5902	-0.2398	0.1021	0.8589
	VMR	0.0572	0.1041	0.4849	0.4832	-0.1600	0.0870	0.8406
	VMI	0.0522	0.0927	0.4461	0.4438	-0.1694	0.0766	0.8597
	SQR	0.0495	0.1030	0.5452	0.5328	-0.2855	0.0904	0.8653
	SQI	0.0458	0.0953	0.5178	0.5033	-0.2936	0.0836	0.8781
	VQR	0.0401	0.0787	0.4103	0.4046	-0.2036	0.0678	0.8660
	VQI	0.0375	0.0731	0.3857	0.3787	-0.2077	0.0628	0.8782
	SAR	0.0324	0.0742	0.4627	0.3200	-0.4471	0.0667	0.8837
	SAI	0.0312	0.0722	0.4569	0.3141	-0.4447	0.0651	0.8904
	VAR	0.0248	0.0556	0.3386	0.2433	-0.3270	0.0498	0.8828
	VAI	0.0241	0.0543	0.3391	0.2389	-0.3286	0.0487	0.8888
2023-03-09	SMR	0.0490	0.0824	0.4510	0.4396	-0.2116	0.0663	0.7836
	SMI	0.0443	0.0738	0.4152	0.4077	-0.1845	0.0590	0.8201
	VMR	0.0404	0.0640	0.3372	0.3288	-0.1534	0.0496	0.7821
	VMI	0.0371	0.0583	0.3210	0.3163	-0.1307	0.0450	0.8155
	SQR	0.0346	0.0639	0.3825	0.3570	-0.2491	0.0537	0.8135
	SQI	0.0314	0.0585	0.3675	0.3505	-0.2232	0.0494	0.8432
	VQR	0.0290	0.0498	0.2882	0.2686	-0.1826	0.0405	0.8093
	VQI	0.0267	0.0463	0.2858	0.2767	-0.1575	0.0378	0.8375
	SAR	0.0229	0.0481	0.3730	0.1970	-0.3679	0.0423	0.8369
	SAI	0.0212	0.0455	0.3653	0.1999	-0.3553	0.0402	0.8556
	VAR	0.0179	0.0359	0.2771	0.1520	-0.2717	0.0311	0.8295
	VAI	0.0168	0.0341	0.2704	0.1578	-0.2616	0.0296	0.8479
2023-03-10	SMR	0.0870	0.1536	0.6643	0.6629	-0.2412	0.1266	0.8429
	SMI	0.0778	0.1372	0.6046	0.6027	-0.2522	0.1131	0.8593
	VMR	0.0696	0.1193	0.5091	0.5085	-0.1715	0.0969	0.8419
	VMI	0.0630	0.1071	0.4725	0.4717	-0.1782	0.0866	0.8577

continue

Table D.1 - Continuation.

Night	Option	MAE	RMSE	MXAE	MMAX	MMIN	STDA	CORR
	SQR	0.0609	0.1139	0.5507	0.5366	-0.3071	0.0963	0.8717
	SQI	0.0555	0.1048	0.5206	0.5053	-0.3052	0.0889	0.8847
	VQR	0.0492	0.0892	0.4240	0.4170	-0.2212	0.0743	0.8698
	VQI	0.0454	0.0827	0.4053	0.3984	-0.2189	0.0690	0.8821
	SAR	0.0397	0.0818	0.4852	0.3135	-0.4698	0.0715	0.8894
	SAI	0.0376	0.0788	0.4721	0.3123	-0.4596	0.0692	0.8978
	VAR	0.0306	0.0623	0.3606	0.2476	-0.3454	0.0543	0.8871
	VAI	0.0292	0.0604	0.3533	0.2514	-0.3374	0.0528	0.8947
2023-03-11	SMR	0.0940	0.1688	0.7216	0.7182	-0.2512	0.1402	0.8328
	SMI	0.0831	0.1498	0.6382	0.6372	-0.2454	0.1246	0.8529
	VMR	0.0750	0.1312	0.5560	0.5536	-0.1834	0.1076	0.8329
	VMI	0.0672	0.1174	0.5008	0.5001	-0.1795	0.0963	0.8512
	SQR	0.0647	0.1220	0.5839	0.5704	-0.3288	0.1034	0.8638
	SQI	0.0585	0.1116	0.5447	0.5365	-0.3064	0.0951	0.8789
	VQR	0.0522	0.0957	0.4541	0.4456	-0.2423	0.0802	0.8625
	VQI	0.0477	0.0879	0.4263	0.4207	-0.2279	0.0739	0.8770
	SAR	0.0415	0.0857	0.5171	0.3218	-0.5107	0.0750	0.8838
	SAI	0.0395	0.0830	0.5052	0.3311	-0.4963	0.0731	0.8914
	VAR	0.0319	0.0655	0.3959	0.2491	-0.3899	0.0572	0.8825
	VAI	0.0305	0.0635	0.3892	0.2556	-0.3820	0.0557	0.8897
2023-03-12	SMR	0.1389	0.2361	0.8074	0.8034	-0.3155	0.1909	0.8332
	SMI	0.1246	0.2142	0.7658	0.7629	-0.3167	0.1742	0.8471
	VMR	0.1089	0.1824	0.6433	0.6408	-0.2338	0.1463	0.8324
	VMI	0.0985	0.1664	0.6029	0.6017	-0.2232	0.1341	0.8465
	SQR	0.0950	0.1696	0.6777	0.6538	-0.4139	0.1405	0.8629
	SQI	0.0871	0.1591	0.6582	0.6417	-0.4080	0.1332	0.8732
	VQR	0.0753	0.1320	0.5350	0.5190	-0.3074	0.1084	0.8613
	VQI	0.0696	0.1241	0.5126	0.5048	-0.2972	0.1027	0.8718
	SAR	0.0614	0.1174	0.6059	0.3904	-0.5982	0.1001	0.8827
	SAI	0.0587	0.1146	0.6013	0.3908	-0.5938	0.0984	0.8886
	VAR	0.0472	0.0901	0.4663	0.3064	-0.4606	0.0768	0.8807
	VAI	0.0455	0.0882	0.4612	0.3029	-0.4565	0.0756	0.8860

continue

Table D.1 - Conclusion.

Night	Option	MAE	RMSE	MXAE	MMAX	MMIN	STDA	CORR
2023-03-13	SMR	0.0971	0.1775	0.7987	0.7924	-0.2782	0.1485	0.8210
	SMI	0.0863	0.1579	0.7291	0.7244	-0.2737	0.1323	0.8429
	VMR	0.0769	0.1362	0.6026	0.5978	-0.2020	0.1124	0.8188
	VMI	0.0690	0.1225	0.5670	0.5638	-0.1986	0.1012	0.8408
	SQR	0.0668	0.1294	0.6550	0.6352	-0.3580	0.1108	0.8572
	SQI	0.0612	0.1202	0.6381	0.6239	-0.3474	0.1035	0.8704
	VQR	0.0534	0.0995	0.4997	0.4866	-0.2661	0.0840	0.8553
	VQI	0.0492	0.0930	0.4925	0.4840	-0.2590	0.0789	0.8681
	SAR	0.0436	0.0927	0.5612	0.3689	-0.5508	0.0818	0.8802
	SAI	0.0416	0.0899	0.5496	0.3813	-0.5325	0.0797	0.8878
	VAR	0.0335	0.0701	0.4306	0.2844	-0.4211	0.0615	0.8785
	VAI	0.0321	0.0681	0.4241	0.2956	-0.4070	0.0601	0.8857

Table D.2 - Complete phase scintillation maps error evaluation and correlation.

Night	Option	MAE	RMSE	MXAE	MMAX	MMIN	STDA	CORR
2023-03-08	SMR	0.0767	0.1562	0.6926	0.6917	-0.2642	0.1360	0.7922
	SMI	0.0686	0.1382	0.6290	0.6261	-0.2740	0.1200	0.8173
	VMR	0.0668	0.1360	0.6076	0.6069	-0.2274	0.1185	0.7927
	VMI	0.0600	0.1207	0.5478	0.5459	-0.2314	0.1047	0.8168
	SQR	0.0552	0.1174	0.5829	0.5756	-0.3294	0.1036	0.8240
	SQI	0.0498	0.1084	0.5475	0.5371	-0.3357	0.0962	0.8426
	VQR	0.0482	0.1020	0.5097	0.5035	-0.2855	0.0899	0.8235
	VQI	0.0436	0.0945	0.4801	0.4711	-0.2905	0.0838	0.8416
	SAR	0.0368	0.0852	0.5161	0.3240	-0.5094	0.0768	0.8434
	SAI	0.0342	0.0825	0.5140	0.3222	-0.5062	0.0751	0.8539
	VAR	0.0321	0.0742	0.4493	0.2810	-0.4433	0.0669	0.8426
	VAI	0.0299	0.0718	0.4486	0.2786	-0.4413	0.0653	0.8533
2023-03-09	SMR	0.0460	0.0814	0.4387	0.4230	-0.2240	0.0672	0.7365
	SMI	0.0413	0.0737	0.4007	0.3912	-0.1928	0.0611	0.7821
	VMR	0.0400	0.0702	0.3742	0.3643	-0.1893	0.0577	0.7390

continue

Table D.2 - Continuation.

Night	Option	MAE	RMSE	MXAE	MMAX	MMIN	STDA	CORR
	VMI	0.0360	0.0640	0.3507	0.3447	-0.1607	0.0529	0.7831
	SQR	0.0334	0.0620	0.3723	0.3311	-0.2703	0.0523	0.7691
	SQI	0.0293	0.0575	0.3549	0.3318	-0.2293	0.0495	0.8085
	VQR	0.0293	0.0538	0.3163	0.2874	-0.2286	0.0451	0.7694
	VQI	0.0257	0.0500	0.3080	0.2912	-0.1940	0.0429	0.8084
	SAR	0.0233	0.0484	0.3921	0.1720	-0.3890	0.0424	0.7866
	SAI	0.0208	0.0456	0.3729	0.1857	-0.3607	0.0406	0.8131
	VAR	0.0205	0.0420	0.3339	0.1486	-0.3312	0.0366	0.7857
	VAI	0.0182	0.0395	0.3187	0.1623	-0.3081	0.0351	0.8129
2023-03-10	SMR	0.0870	0.1591	0.6798	0.6731	-0.3006	0.1332	0.7882
	SMI	0.0765	0.1421	0.6039	0.5982	-0.2839	0.1197	0.8151
	VMR	0.0759	0.1399	0.6042	0.5991	-0.2623	0.1175	0.7879
	VMI	0.0669	0.1257	0.5370	0.5326	-0.2454	0.1064	0.8152
	SQR	0.0625	0.1187	0.5666	0.5354	-0.3802	0.1010	0.8229
	SQI	0.0544	0.1084	0.5327	0.5107	-0.3533	0.0938	0.8474
	VQR	0.0547	0.1047	0.5042	0.4791	-0.3320	0.0893	0.8218
	VQI	0.0477	0.0957	0.4694	0.4505	-0.3054	0.0830	0.8468
	SAR	0.0423	0.0892	0.5526	0.2942	-0.5484	0.0785	0.8414
	SAI	0.0376	0.0847	0.5365	0.3062	-0.5314	0.0759	0.8582
	VAR	0.0371	0.0789	0.4843	0.2627	-0.4799	0.0696	0.8403
	VAI	0.0329	0.0749	0.4707	0.2744	-0.4657	0.0673	0.8572
2023-03-11	SMR	0.0989	0.1859	0.8065	0.7993	-0.3286	0.1574	0.7642
	SMI	0.0866	0.1652	0.7243	0.7216	-0.2987	0.1406	0.7942
	VMR	0.0869	0.1650	0.7210	0.7155	-0.2888	0.1403	0.7633
	VMI	0.0761	0.1468	0.6567	0.6558	-0.2556	0.1255	0.7942
	SQR	0.0696	0.1350	0.6629	0.6316	-0.4251	0.1156	0.8019
	SQI	0.0610	0.1236	0.6249	0.6077	-0.3828	0.1075	0.8280
	VQR	0.0614	0.1197	0.5904	0.5626	-0.3754	0.1027	0.8000
	VQI	0.0537	0.1095	0.5603	0.5438	-0.3362	0.0954	0.8271
	SAR	0.0454	0.0971	0.6403	0.3254	-0.6376	0.0859	0.8240
	SAI	0.0420	0.0939	0.6265	0.3477	-0.6174	0.0840	0.8366
	VAR	0.0400	0.0863	0.5735	0.2861	-0.5707	0.0765	0.8219

continue

Table D.2 - Conclusion.

Night	Option	MAE	RMSE	MXAE	MMAX	MMIN	STDA	CORR
	VAI	0.0368	0.0833	0.5592	0.3064	-0.5515	0.0747	0.8352
2023-03-12	SMR	0.1719	0.2929	1.1238	1.1082	-0.5245	0.2371	0.7402
	SMI	0.1507	0.2644	1.0518	1.0488	-0.4686	0.2172	0.7750
	VMR	0.1499	0.2573	1.0148	1.0022	-0.4619	0.2092	0.7414
	VMI	0.1316	0.2329	0.9527	0.9510	-0.4163	0.1922	0.7746
	SQR	0.1208	0.2146	0.9818	0.8960	-0.6692	0.1774	0.7796
	SQI	0.1077	0.1991	0.9280	0.8820	-0.6258	0.1675	0.8082
	VQR	0.1056	0.1889	0.8764	0.8027	-0.5860	0.1567	0.7789
	VQI	0.0942	0.1751	0.8225	0.7881	-0.5436	0.1476	0.8079
	SAR	0.0784	0.1574	0.9207	0.4675	-0.9173	0.1365	0.7972
	SAI	0.0736	0.1515	0.9036	0.4834	-0.8999	0.1325	0.8138
	VAR	0.0685	0.1386	0.8258	0.4163	-0.8222	0.1205	0.7965
	VAI	0.0643	0.1335	0.8094	0.4245	-0.8056	0.1170	0.8128
2023-03-13	SMR	0.1102	0.2049	0.8620	0.8360	-0.3719	0.1727	0.7745
	SMI	0.0969	0.1824	0.8041	0.7962	-0.3467	0.1546	0.8022
	VMR	0.0960	0.1798	0.7689	0.7461	-0.3254	0.1520	0.7729
	VMI	0.0844	0.1606	0.7208	0.7147	-0.3009	0.1367	0.7999
	SQR	0.0789	0.1523	0.7580	0.6980	-0.4667	0.1302	0.8167
	SQI	0.0695	0.1407	0.7227	0.6931	-0.4334	0.1223	0.8366
	VQR	0.0688	0.1328	0.6629	0.6114	-0.4124	0.1136	0.8153
	VQI	0.0605	0.1229	0.6362	0.6109	-0.3813	0.1070	0.8352
	SAR	0.0523	0.1094	0.6896	0.3923	-0.6826	0.0960	0.8428
	SAI	0.0478	0.1053	0.6691	0.4151	-0.6562	0.0938	0.8555
	VAR	0.0458	0.0956	0.6112	0.3416	-0.6040	0.0840	0.8414
	VAI	0.0416	0.0919	0.5941	0.3622	-0.5797	0.0819	0.8548

Table D.3 - Complete ROTI scintillation maps error evaluation and correlation.

Night	Option	MAE	RMSE	MXAE	MMAX	MMIN	STDA	CORR
2023-03-08	SMR	0.0176	0.0426	0.2128	0.2121	-0.0851	0.0388	0.7997
	SMI	0.0158	0.0377	0.1930	0.1913	-0.0882	0.0343	0.8230

continue

Table D.3 - Continuation.

Night	Option	MAE	RMSE	MXAE	MMAX	MMIN	STDA	CORR
	VMR	0.0130	0.0318	0.1637	0.1630	-0.0650	0.0291	0.8033
	VMI	0.0117	0.0283	0.1534	0.1517	-0.0648	0.0258	0.8243
	SQR	0.0134	0.0341	0.1890	0.1858	-0.1055	0.0313	0.8300
	SQI	0.0121	0.0313	0.1782	0.1731	-0.1029	0.0288	0.8501
	VQR	0.0099	0.0253	0.1447	0.1419	-0.0801	0.0233	0.8319
	VQI	0.0090	0.0233	0.1371	0.1328	-0.0766	0.0215	0.8504
	SAR	0.0093	0.0261	0.1655	0.1064	-0.1631	0.0243	0.8523
	SAI	0.0087	0.0250	0.1653	0.1058	-0.1609	0.0235	0.8644
	VAR	0.0069	0.0194	0.1276	0.0799	-0.1256	0.0181	0.8533
	VAI	0.0064	0.0187	0.1251	0.0786	-0.1224	0.0175	0.8647
2023-03-09	SMR	0.0106	0.0237	0.1374	0.1347	-0.0634	0.0212	0.7402
	SMI	0.0094	0.0207	0.1275	0.1256	-0.0527	0.0185	0.7974
	VMR	0.0079	0.0176	0.1064	0.1039	-0.0468	0.0158	0.7402
	VMI	0.0070	0.0156	0.1012	0.1001	-0.0383	0.0139	0.7943
	SQR	0.0081	0.0186	0.1176	0.1096	-0.0751	0.0168	0.7840
	SQI	0.0072	0.0169	0.1109	0.1067	-0.0623	0.0153	0.8253
	VQR	0.0060	0.0139	0.0901	0.0839	-0.0561	0.0125	0.7813
	VQI	0.0053	0.0127	0.0857	0.0828	-0.0460	0.0115	0.8227
	SAR	0.0057	0.0144	0.1174	0.0547	-0.1159	0.0132	0.8183
	SAI	0.0051	0.0132	0.1103	0.0589	-0.1064	0.0122	0.8489
	VAR	0.0043	0.0107	0.0878	0.0416	-0.0868	0.0098	0.8135
	VAI	0.0038	0.0098	0.0823	0.0450	-0.0791	0.0090	0.8461
2023-03-10	SMR	0.0275	0.0582	0.2206	0.2188	-0.1018	0.0513	0.7653
	SMI	0.0242	0.0507	0.2007	0.1979	-0.1058	0.0446	0.7978
	VMR	0.0203	0.0440	0.1708	0.1696	-0.0777	0.0390	0.7660
	VMI	0.0181	0.0384	0.1560	0.1537	-0.0794	0.0339	0.7965
	SQR	0.0203	0.0448	0.1913	0.1833	-0.1248	0.0399	0.8117
	SQI	0.0180	0.0406	0.1832	0.1751	-0.1236	0.0365	0.8384
	VQR	0.0150	0.0340	0.1467	0.1407	-0.0962	0.0304	0.8102
	VQI	0.0134	0.0310	0.1431	0.1372	-0.0940	0.0280	0.8361
	SAR	0.0136	0.0337	0.1831	0.1020	-0.1818	0.0308	0.8421
	SAI	0.0126	0.0323	0.1813	0.1057	-0.1796	0.0298	0.8552

continue

Table D.3 - Continuation.

Night	Option	MAE	RMSE	MXAE	MMAX	MMIN	STDA	CORR
	VAR	0.0101	0.0258	0.1423	0.0786	-0.1414	0.0237	0.8393
	VAI	0.0094	0.0248	0.1409	0.0825	-0.1391	0.0230	0.8521
2023-03-11	SMR	0.0279	0.0605	0.2563	0.2545	-0.1058	0.0537	0.7709
	SMI	0.0245	0.0533	0.2263	0.2239	-0.1039	0.0473	0.8006
	VMR	0.0213	0.0472	0.2079	0.2069	-0.0795	0.0421	0.7739
	VMI	0.0187	0.0414	0.1827	0.1809	-0.0769	0.0369	0.8002
	SQR	0.0203	0.0458	0.2181	0.2116	-0.1371	0.0410	0.8154
	SQI	0.0181	0.0417	0.2042	0.1968	-0.1320	0.0376	0.8382
	VQR	0.0154	0.0353	0.1727	0.1671	-0.1057	0.0317	0.8146
	VQI	0.0137	0.0321	0.1631	0.1569	-0.1016	0.0291	0.8361
	SAR	0.0133	0.0332	0.2043	0.1163	-0.2026	0.0304	0.8461
	SAI	0.0126	0.0321	0.2031	0.1202	-0.2000	0.0295	0.8567
	VAR	0.0101	0.0255	0.1629	0.0887	-0.1609	0.0234	0.8423
	VAI	0.0095	0.0246	0.1601	0.0918	-0.1573	0.0227	0.8533
2023-03-12	SMR	0.0507	0.0928	0.3364	0.3291	-0.1743	0.0778	0.7427
	SMI	0.0446	0.0844	0.3155	0.3140	-0.1563	0.0716	0.7771
	VMR	0.0390	0.0724	0.2820	0.2757	-0.1375	0.0610	0.7453
	VMI	0.0342	0.0657	0.2609	0.2598	-0.1201	0.0560	0.7773
	SQR	0.0376	0.0723	0.3056	0.2798	-0.2133	0.0618	0.7873
	SQI	0.0336	0.0670	0.2846	0.2741	-0.1970	0.0580	0.8167
	VQR	0.0287	0.0559	0.2531	0.2315	-0.1715	0.0480	0.7867
	VQI	0.0257	0.0519	0.2343	0.2254	-0.1530	0.0451	0.8158
	SAR	0.0251	0.0539	0.2864	0.1564	-0.2854	0.0477	0.8142
	SAI	0.0235	0.0518	0.2836	0.1610	-0.2817	0.0461	0.8297
	VAR	0.0190	0.0418	0.2381	0.1246	-0.2373	0.0373	0.8106
	VAI	0.0178	0.0403	0.2335	0.1274	-0.2319	0.0361	0.8261
2023-03-13	SMR	0.0290	0.0630	0.2734	0.2706	-0.1169	0.0560	0.7690
	SMI	0.0256	0.0565	0.2567	0.2550	-0.1134	0.0503	0.7981
	VMR	0.0217	0.0474	0.2206	0.2175	-0.0878	0.0421	0.7723
	VMI	0.0191	0.0424	0.2072	0.2061	-0.0850	0.0379	0.7977
	SQR	0.0212	0.0482	0.2389	0.2292	-0.1472	0.0433	0.8183
	SQI	0.0190	0.0449	0.2345	0.2285	-0.1420	0.0407	0.8381

continue

Table D.3 - Conclusion.

Night	Option	MAE	RMSE	MXAE	MMAX	MMIN	STDA	CORR
	VQR	0.0157	0.0357	0.1848	0.1753	-0.1128	0.0320	0.8211
	VQI	0.0140	0.0332	0.1839	0.1777	-0.1088	0.0301	0.8388
	SAR	0.0144	0.0360	0.2192	0.1355	-0.2160	0.0330	0.8484
	SAI	0.0135	0.0347	0.2153	0.1404	-0.2109	0.0320	0.8594
	VAR	0.0106	0.0265	0.1720	0.1012	-0.1692	0.0243	0.8484
	VAI	0.0099	0.0257	0.1688	0.1055	-0.1651	0.0237	0.8588

APPENDIX E - PROBABILITY MAPS COMPLETE ERROR EVALUATION AND CORRELATION TABLES

Table E.1 - Complete amplitude scintillation derived probability maps error metrics and correlation results.

Night	Option	MAE	RMSE	MXAE	MMAX	MMIN	STDA	CORR
2023-03-08	SMR	4.2514	9.0431	16.5886	16.5439	-0.3235	7.9814	0.9365
	SMI	3.7043	8.3649	16.2082	15.7316	-0.7619	7.5000	0.9370
	VMR	4.3789	9.2988	17.9235	17.8852	-0.1404	8.2032	0.9252
	VMI	3.9287	8.7400	17.5662	17.0927	-0.6096	7.8072	0.9259
	SQR	2.7072	5.9883	10.4253	10.2579	-1.0253	5.3414	0.9598
	SQI	2.3833	5.5090	10.2815	9.6953	-1.4191	4.9668	0.9576
	VQR	2.8324	6.2467	11.1319	11.0461	-0.5525	5.5676	0.9536
	VQI	2.5056	5.7187	10.9247	10.3962	-0.8591	5.1406	0.9529
	SAR	1.1581	2.7240	6.3486	2.4409	-6.1522	2.4656	0.9248
	SAI	1.1644	2.6626	6.1894	2.1353	-6.1374	2.3945	0.9283
	VAR	1.0474	2.3976	5.6771	2.8334	-5.1871	2.1567	0.9411
	VAI	1.0397	2.3785	5.7838	2.5778	-5.4967	2.1392	0.9415
2023-03-09	SMR	1.1482	4.0651	6.7253	6.4533	-0.7908	3.8996	0.9034
	SMI	0.9499	3.5180	6.2189	5.8841	-0.9381	3.3874	0.9017
	VMR	1.2381	4.1493	6.7791	6.6038	-0.5321	3.9603	0.8972
	VMI	1.0346	3.6244	6.6561	6.4461	-0.6206	3.4736	0.9047
	SQR	0.6582	2.5146	4.2163	3.7125	-1.2583	2.4269	0.9043
	SQI	0.5897	2.2870	4.0647	3.3848	-1.3810	2.2097	0.9047
	VQR	0.7085	2.5796	4.3846	3.9682	-0.9371	2.4804	0.9131
	VQI	0.6224	2.3051	4.3004	3.9319	-0.9306	2.2195	0.9166
	SAR	0.5134	1.7307	3.7037	0.1471	-3.7037	1.6527	0.8011
	SAI	0.5808	1.9086	3.8868	0.1500	-3.8868	1.8181	0.7572
	VAR	0.4834	1.7157	3.7219	0.2797	-3.7184	1.6462	0.7975
	VAI	0.5314	1.7997	3.8296	0.1689	-3.8296	1.7195	0.7841
2023-03-10	SMR	5.8138	11.2792	20.2125	20.1964	-0.3694	9.6654	0.9270
	SMI	5.0271	10.0610	18.6839	18.5219	-0.9702	8.7150	0.9340
	VMR	6.0615	11.4407	20.7010	20.7000	-0.2016	9.7030	0.9217
	VMI	5.2472	10.1742	18.8649	18.4854	-0.9934	8.7167	0.9297

continue

Table E.1 - Continuation.

Night	Option	MAE	RMSE	MXAE	MMAX	MMIN	STDA	CORR
	SQR	3.5969	7.7018	13.9481	13.8331	-0.9961	6.8103	0.9513
	SQI	3.0186	6.6657	12.3497	12.0209	-1.4242	5.9430	0.9551
	VQR	3.7858	7.7945	14.6829	14.6751	-0.6120	6.8134	0.9508
	VQI	3.2327	6.8387	12.9655	12.5047	-1.2686	6.0264	0.9554
	SAR	1.5355	2.9035	5.7852	2.5648	-5.4663	2.4643	0.9553
	SAI	1.4729	2.8451	5.8702	2.1779	-5.8027	2.4342	0.9575
	VAR	1.3810	2.6497	5.5545	2.7662	-4.9889	2.2614	0.9612
	VAI	1.3253	2.6183	5.6030	2.1519	-5.1859	2.2581	0.9629
2023-03-11	SMR	6.3430	11.9369	21.2289	21.1641	-0.4048	10.1122	0.9326
	SMI	5.3641	10.6031	19.1360	19.0809	-0.5504	9.1462	0.9425
	VMR	6.6096	12.2052	22.2405	22.1925	-0.2597	10.2606	0.9291
	VMI	5.6286	10.8218	19.3328	19.2649	-0.5632	9.2428	0.9386
	SQR	3.7017	7.7428	14.0575	13.9947	-0.8276	6.8006	0.9605
	SQI	3.1810	6.8412	12.0781	12.0116	-1.1487	6.0567	0.9668
	VQR	3.9914	8.0005	14.7252	14.6174	-0.7820	6.9337	0.9564
	VQI	3.3734	6.9519	12.6518	12.5839	-0.9946	6.0786	0.9633
	SAR	1.3997	2.9772	7.1257	2.4668	-6.0342	2.6276	0.9680
	SAI	1.4577	3.1800	7.4559	2.4389	-6.4764	2.8262	0.9634
	VAR	1.3299	2.8064	6.6178	2.8537	-5.4389	2.4713	0.9715
	VAI	1.3316	2.8996	6.6926	2.4258	-5.9246	2.5758	0.9693
2023-03-12	SMR	10.7814	18.2236	26.6995	26.6371	-0.2632	14.6922	0.9495
	SMI	9.8145	17.1199	25.6153	25.4967	-0.4242	14.0273	0.9531
	VMR	11.0121	18.4107	27.2527	27.1920	-0.1667	14.7543	0.9475
	VMI	9.8921	17.0153	26.1364	26.0194	-0.2804	13.8444	0.9526
	SQR	7.2299	13.1574	19.5891	19.4705	-0.8543	10.9929	0.9690
	SQI	6.5226	12.1497	18.2152	17.9937	-1.1221	10.2504	0.9716
	VQR	7.3534	13.0654	19.3561	19.2375	-0.5620	10.7997	0.9686
	VQI	6.7197	12.2782	18.4029	18.2842	-0.8346	10.2762	0.9707
	SAR	2.3076	4.5491	8.5417	5.7119	-6.2936	3.9204	0.9799
	SAI	2.2779	4.4912	8.7371	5.6058	-6.8515	3.8707	0.9792
	VAR	2.1409	4.2444	8.3424	5.9253	-6.0980	3.6649	0.9811
	VAI	2.1311	4.1786	8.3658	5.5866	-6.4002	3.5943	0.9807

continue

Table E.1 - Conclusion.

Night	Option	MAE	RMSE	MXAE	MMAX	MMIN	STDA	CORR
2023-03-13	SMR	6.4866	12.4150	25.6141	25.6039	-0.4203	10.5856	0.9510
	SMI	5.6790	11.2703	23.7317	23.6484	-0.5208	9.7350	0.9559
	VMR	6.7341	12.6320	26.0241	26.0116	-0.3474	10.6874	0.9493
	VMI	5.8838	11.3921	24.5277	24.4444	-0.4133	9.7550	0.9554
	SQR	3.9931	8.3102	18.5971	18.3774	-0.9738	7.2880	0.9681
	SQI	3.5319	7.5925	16.7950	16.6772	-1.2207	6.7209	0.9695
	VQR	4.2380	8.6465	19.5919	19.4475	-0.7326	7.5367	0.9648
	VQI	3.6554	7.6215	17.3673	17.2222	-0.8344	6.6877	0.9674
	SAR	1.4141	2.8100	6.3122	2.8616	-5.9321	2.4283	0.9726
	SAI	1.3469	2.7554	6.3714	2.9010	-6.0051	2.4038	0.9735
	VAR	1.2787	2.5650	5.9646	2.7572	-5.6955	2.2236	0.9766
	VAI	1.2639	2.5867	6.0397	2.7470	-5.8574	2.2569	0.9762

Table E.2 - Complete phase scintillation derived probability maps error metrics and correlation results.

Night	Option	MAE	RMSE	MXAE	MMAX	MMIN	STDA	CORR
2023-03-08	SMR	4.0186	8.4603	14.3309	14.0931	-0.3247	7.4450	0.9441
	SMI	3.6390	7.9096	13.7107	13.2594	-0.5204	7.0227	0.9466
	VMR	4.0658	8.5060	14.4330	14.2431	-0.2651	7.4714	0.9425
	VMI	3.6544	7.8999	13.7543	13.3157	-0.5045	7.0038	0.9467
	SQR	2.4900	5.7083	9.9695	9.6249	-0.7788	5.1366	0.9651
	SQI	2.1844	5.1130	9.7148	9.2103	-0.9582	4.6228	0.9655
	VQR	2.4955	5.6482	9.8688	9.5260	-0.6791	5.0670	0.9647
	VQI	2.2352	5.2259	9.8234	9.3237	-0.9538	4.7238	0.9630
	SAR	1.0421	2.4705	5.3937	2.5513	-4.8570	2.2399	0.9142
	SAI	1.0258	2.4198	5.4525	2.3729	-5.0686	2.1916	0.9164
	VAR	1.0229	2.4617	5.4096	2.6903	-4.9894	2.2392	0.9131
	VAI	0.9917	2.3957	5.5540	2.3479	-5.1384	2.1808	0.9176
2023-03-09	SMR	0.8930	3.4021	5.6680	5.4662	-0.6102	3.2828	0.8783
	SMI	0.7467	2.8889	4.9559	4.4160	-0.7182	2.7907	0.8859

continue

Table E.2 - Continuation.

Night	Option	MAE	RMSE	MXAE	MMAX	MMIN	STDA	CORR
	VMR	0.9126	3.3656	5.8204	5.6232	-0.5663	3.2395	0.8840
	VMI	0.7547	2.9370	5.1897	4.7793	-0.5496	2.8384	0.8805
	SQR	0.4045	1.5849	2.9322	2.2844	-1.0825	1.5324	0.9140
	SQI	0.3972	1.6626	3.1638	2.1866	-1.2671	1.6145	0.8816
	VQR	0.4183	1.6074	2.8649	2.2940	-1.0620	1.5520	0.9048
	VQI	0.3946	1.6521	3.0799	2.2764	-1.1691	1.6043	0.8813
	SAR	0.3750	1.4386	3.0636	0.1692	-3.0636	1.3889	0.7175
	SAI	0.3898	1.4916	3.1969	0.0852	-3.1969	1.4398	0.6999
	VAR	0.3855	1.4813	3.1146	0.1642	-3.1146	1.4303	0.7021
	VAI	0.3980	1.5216	3.1782	0.0609	-3.1782	1.4686	0.6879
2023-03-10	SMR	4.5614	9.7542	16.6842	16.6176	-0.9793	8.6220	0.9101
	SMI	3.9960	8.6919	15.4120	15.0124	-1.2109	7.7189	0.9159
	VMR	4.6152	9.8271	16.7911	16.7245	-0.8985	8.6759	0.9072
	VMI	4.0707	8.7936	15.4963	15.1713	-1.1866	7.7947	0.9117
	SQR	2.7648	6.2886	10.5435	10.0183	-1.5044	5.6482	0.9304
	SQI	2.3003	5.4047	9.6510	8.9915	-1.6127	4.8907	0.9366
	VQR	2.7735	6.2311	10.3557	9.9020	-1.4412	5.5799	0.9321
	VQI	2.3754	5.5089	9.6802	8.9667	-1.6396	4.9705	0.9340
	SAR	1.2600	2.7682	5.7296	1.7911	-5.3578	2.4648	0.9175
	SAI	1.2936	2.8424	5.9637	1.6616	-5.8105	2.5310	0.9142
	VAR	1.2731	2.7855	5.8831	1.8741	-5.4549	2.4776	0.9165
	VAI	1.2744	2.7887	5.8893	1.7026	-5.6692	2.4805	0.9167
2023-03-11	SMR	5.8897	12.0336	19.9558	19.8881	-0.3332	10.4937	0.9263
	SMI	5.0802	10.7696	17.1742	17.0003	-0.7562	9.4961	0.9328
	VMR	5.9929	12.1396	20.2014	20.1466	-0.3954	10.5573	0.9233
	VMI	5.1826	10.9454	17.2931	17.1395	-0.8545	9.6407	0.9285
	SQR	3.4976	7.9239	12.8690	12.5833	-1.2576	7.1103	0.9516
	SQI	3.0299	6.9887	11.6237	11.2487	-1.4519	6.2978	0.9586
	VQR	3.5288	7.9454	12.9666	12.7160	-1.3293	7.1188	0.9498
	VQI	3.0814	7.1001	11.7366	11.4512	-1.3778	6.3966	0.9552
	SAR	1.3428	2.9421	6.3687	1.9425	-6.0615	2.6178	0.9337
	SAI	1.4511	3.2070	7.1591	1.9187	-6.7359	2.8599	0.9223

continue

Table E.2 - Conclusion.

Night	Option	MAE	RMSE	MXAE	MMAX	MMIN	STDA	CORR
	VAR	1.3319	2.8887	6.1798	1.9370	-5.9854	2.5634	0.9353
	VAI	1.4200	3.1058	6.9199	1.9142	-6.5602	2.7621	0.9267
2023-03-12	SMR	13.3951	21.7845	39.6509	39.6509	-0.3561	17.1795	0.9256
	SMI	12.1239	20.0818	37.7096	37.7096	-0.4197	16.0091	0.9342
	VMR	13.1941	21.4257	39.2054	39.2054	-0.3596	16.8813	0.9280
	VMI	12.0723	19.9813	37.4630	37.4630	-0.3839	15.9221	0.9375
	SQR	8.6645	15.3162	27.3602	27.3602	-0.8733	12.6298	0.9560
	SQI	8.1637	14.4300	27.1052	27.1052	-1.0444	11.8987	0.9558
	VQR	8.7162	15.3013	27.9582	27.9582	-0.7885	12.5761	0.9564
	VQI	8.1412	14.3527	26.9965	26.9965	-1.1557	11.8204	0.9560
	SAR	2.2500	4.5718	9.5770	7.4233	-6.2650	3.9798	0.9574
	SAI	2.1848	4.3856	9.3053	6.7490	-6.2530	3.8027	0.9586
	VAR	2.2247	4.5167	9.3846	7.3239	-6.0503	3.9308	0.9571
	VAI	2.1920	4.3711	9.2457	6.6452	-6.6174	3.7818	0.9578
2023-03-13	SMR	6.4867	12.8221	24.8543	24.5733	-0.4569	11.0603	0.9477
	SMI	5.7937	11.8746	24.0427	23.7204	-0.7280	10.3653	0.9497
	VMR	6.5877	12.9492	24.7273	24.4468	-0.4574	11.1482	0.9485
	VMI	5.8328	11.9112	24.3175	24.0033	-0.6346	10.3853	0.9507
	SQR	3.9712	8.5351	18.0032	17.5011	-1.0852	7.5550	0.9674
	SQI	3.5549	7.8112	17.3961	16.9668	-1.1710	6.9554	0.9697
	VQR	3.9550	8.4947	17.8817	17.4938	-0.9196	7.5179	0.9687
	VQI	3.5785	7.8362	17.3262	16.9106	-1.0972	6.9714	0.9688
	SAR	1.3931	3.2140	7.4627	4.1862	-6.0775	2.8964	0.9513
	SAI	1.3126	2.9960	6.6054	3.4233	-5.8991	2.6931	0.9554
	VAR	1.3676	3.1544	7.5123	4.0115	-5.8841	2.8425	0.9524
	VAI	1.3144	2.9794	6.8405	3.6754	-5.7801	2.6738	0.9563

Table E.3 - Complete ROTI scintillation derived probability maps error metrics and correlation results.

Night	Option	MAE	RMSE	MXAE	MMAX	MMIN	STDA	CORR
2023-03-08	SMR	4.0575	8.8175	16.0433	16.0433	-0.1513	7.8285	0.9422
	SMI	3.5992	8.0036	14.5763	14.4700	-0.3727	7.1487	0.9509
	VMR	4.0648	8.6552	15.4830	15.4830	-0.0914	7.6414	0.9419
	VMI	3.5890	7.8250	14.0029	13.9070	-0.2907	6.9534	0.9459
	SQR	2.9200	6.4561	11.5827	11.5149	-0.3519	5.7580	0.9619
	SQI	2.5932	5.9118	11.0349	10.8995	-0.6270	5.3127	0.9619
	VQR	2.9067	6.3024	11.2183	11.1506	-0.2332	5.5920	0.9607
	VQI	2.5898	5.7198	10.2504	10.1345	-0.4611	5.0999	0.9613
	SAR	1.1080	2.5918	5.1414	4.1216	-3.9575	2.3430	0.9228
	SAI	1.1237	2.5728	4.9631	3.4507	-4.2620	2.3144	0.9168
	VAR	1.1003	2.5738	4.9006	3.7417	-3.9733	2.3267	0.9209
	VAI	1.1042	2.5605	5.0213	3.3385	-4.3962	2.3102	0.9137
2023-03-09	SMR	0.9225	3.3477	5.9622	5.8570	-0.2756	3.2181	0.9186
	SMI	0.7352	2.8187	5.7231	5.4887	-0.6121	2.7211	0.9042
	VMR	0.9646	3.3622	6.0517	5.9820	-0.2152	3.2209	0.9216
	VMI	0.7742	2.7628	5.4234	5.2037	-0.5154	2.6521	0.8986
	SQR	0.5599	2.1931	4.0040	3.5527	-0.8531	2.1204	0.9042
	SQI	0.4640	1.8514	3.6614	3.1281	-1.0288	1.7924	0.8993
	VQR	0.5658	2.1367	4.2283	3.7858	-0.8073	2.0604	0.9026
	VQI	0.4567	1.7592	3.4922	2.9139	-0.9453	1.6989	0.8981
	SAR	0.3770	1.4305	3.1558	0.3938	-3.1066	1.3799	0.7450
	SAI	0.3652	1.3433	3.1199	0.2487	-3.1199	1.2927	0.7847
	VAR	0.3925	1.4823	3.3048	0.6298	-3.2696	1.4294	0.7216
	VAI	0.3866	1.4076	3.2405	0.4700	-3.2405	1.3535	0.7577
2023-03-10	SMR	6.2743	12.4959	20.3023	20.1769	-0.3796	10.8065	0.9089
	SMI	5.5612	11.4757	18.5428	18.2523	-0.6775	10.0381	0.9191
	VMR	6.2125	12.1651	19.3563	19.2985	-0.3362	10.4591	0.9088
	VMI	5.5798	11.2863	18.1607	17.9255	-0.5234	9.8105	0.9202
	SQR	4.2035	8.9758	14.2445	13.9889	-0.8266	7.9307	0.9311
	SQI	3.7928	8.2060	13.1146	12.8806	-0.8708	7.2769	0.9378

continue

Table E.3 - Continuation.

Night	Option	MAE	RMSE	MXAE	MMAX	MMIN	STDA	CORR
	VQR	4.0851	8.5444	13.6388	13.4042	-0.6984	7.5045	0.9354
	VQI	3.6509	7.8252	12.3967	12.1353	-0.7464	6.9213	0.9403
	SAR	1.4525	3.1099	5.9987	4.7439	-3.4975	2.7498	0.9494
	SAI	1.3658	2.9665	5.7971	4.3094	-3.5512	2.6334	0.9473
	VAR	1.3790	2.9678	5.5264	4.1039	-3.4728	2.6279	0.9497
	VAI	1.3859	2.9160	5.6056	3.9270	-3.4869	2.5657	0.9463
2023-03-11	SMR	6.3572	12.2562	21.7493	21.7075	-0.2385	10.4786	0.9374
	SMI	5.7218	11.5107	19.9508	19.8551	-0.9839	9.9879	0.9394
	VMR	6.3631	12.1242	21.5676	21.5234	-0.2514	10.3202	0.9378
	VMI	5.7797	11.4199	20.0070	19.8805	-1.1088	9.8493	0.9385
	SQR	4.0085	8.4735	14.7778	14.6659	-0.7238	7.4654	0.9617
	SQI	3.6853	7.9027	13.5590	13.1308	-1.5632	6.9908	0.9613
	VQR	3.9976	8.3175	14.4426	14.3441	-0.8845	7.2939	0.9595
	VQI	3.6040	7.6273	12.9093	12.5586	-1.5137	6.7221	0.9611
	SAR	1.5479	3.5463	8.0250	4.6262	-5.4183	3.1907	0.9562
	SAI	1.5867	3.6527	8.3697	4.2987	-6.0231	3.2901	0.9528
	VAR	1.5348	3.5370	7.8147	4.6802	-5.4197	3.1866	0.9557
	VAI	1.5532	3.6123	8.2269	4.5589	-5.7693	3.2614	0.9522
2023-03-12	SMR	13.3934	21.6374	36.8653	36.8653	-0.1981	16.9939	0.9431
	SMI	12.9801	21.0506	35.8516	35.8516	-0.2315	16.5725	0.9453
	VMR	13.4208	21.4726	37.1748	37.1748	-0.2086	16.7618	0.9441
	VMI	12.8963	20.9014	36.1296	36.1296	-0.1698	16.4485	0.9447
	SQR	9.3220	16.2824	25.4884	25.3933	-0.5491	13.3498	0.9683
	SQI	8.9956	15.4787	25.7012	25.7012	-0.8956	12.5964	0.9674
	VQR	9.3101	16.0701	25.0831	25.0728	-0.6207	13.0984	0.9696
	VQI	8.8621	15.2501	24.6554	24.5340	-0.8284	12.4108	0.9689
	SAR	3.7612	7.1847	12.9680	11.0290	-5.0381	6.1215	0.9742
	SAI	3.5425	6.8138	12.6506	10.6256	-4.8712	5.8205	0.9751
	VAR	3.5157	6.7210	12.4522	10.5269	-4.6334	5.7282	0.9760
	VAI	3.3701	6.5052	12.4565	10.3905	-4.7566	5.5642	0.9755
2023-03-13	SMR	7.3845	13.8794	27.3770	27.3405	-0.3060	11.7519	0.9433
	SMI	6.5429	12.7571	25.9133	25.8599	-0.4578	10.9515	0.9462

continue

Table E.3 - Conclusion.

Night	Option	MAE	RMSE	MXAE	MMAX	MMIN	STDA	CORR
	VMR	7.3287	13.6637	27.1850	27.1822	-0.2493	11.5320	0.9455
	VMI	6.5451	12.5680	25.4493	25.3959	-0.2801	10.7293	0.9489
	SQR	4.7959	9.8841	21.0478	20.8101	-1.0002	8.6427	0.9606
	SQI	4.3547	9.0745	19.7490	19.5522	-0.9888	7.9613	0.9655
	VQR	4.7892	9.7279	21.0099	20.8645	-0.7827	8.4674	0.9634
	VQI	4.3037	8.9243	19.4150	19.2942	-0.8210	7.8180	0.9673
	SAR	1.7220	3.8653	9.4130	7.5352	-4.0320	3.4605	0.9639
	SAI	1.6732	3.7337	8.8328	7.3605	-3.9388	3.3378	0.9635
	VAR	1.6807	3.6968	8.9891	7.2303	-4.0850	3.2927	0.9644
	VAI	1.6639	3.6347	8.7424	7.2096	-4.0226	3.2315	0.9643

PUBLICAÇÕES TÉCNICO-CIENTÍFICAS EDITADAS PELO INPE

Teses e Dissertações (TDI)

Teses e Dissertações apresentadas nos Cursos de Pós-Graduação do INPE.

Notas Técnico-Científicas (NTC)

Incluem resultados preliminares de pesquisa, descrição de equipamentos, descrição e ou documentação de programas de computador, descrição de sistemas e experimentos, apresentação de testes, dados, atlas, e documentação de projetos de engenharia.

Propostas e Relatórios de Projetos (PRP)

São propostas de projetos técnico-científicos e relatórios de acompanhamento de projetos, atividades e convênios.

Publicações Seriadas

São os seriados técnico-científicos: boletins, periódicos, anuários e anais de eventos (simpósios e congressos). Constam destas publicações o Internacional Standard Serial Number (ISSN), que é um código único e definitivo para identificação de títulos de seriados.

Pré-publicações (PRE)

Todos os artigos publicados em periódicos, anais e como capítulos de livros.

Manuais Técnicos (MAN)

São publicações de caráter técnico que incluem normas, procedimentos, instruções e orientações.

Relatórios de Pesquisa (RPQ)

Reportam resultados ou progressos de pesquisas tanto de natureza técnica quanto científica, cujo nível seja compatível com o de uma publicação em periódico nacional ou internacional.

Publicações Didáticas (PUD)

Incluem apostilas, notas de aula e manuais didáticos.

Programas de Computador (PDC)

São a seqüência de instruções ou códigos, expressos em uma linguagem de programação compilada ou interpretada, a ser executada por um computador para alcançar um determinado objetivo. Aceitam-se tanto programas fonte quanto os executáveis.